

A study of the effects of organic matter on illitization in the Woodford Shale, Oklahoma and
Kansas

by

Kale W. Janssen

B.S., Kansas State University, 2015

A THESIS

submitted in partial fulfillment of the requirements for the degree

MASTER OF SCIENCE

Department of Geology
College of Arts and Sciences

KANSAS STATE UNIVERSITY
Manhattan, Kansas

2017

Approved by:

Major Professor
Matthew Totten

Copyright

© Kale Janssen 2017.

Abstract

The Woodford Shale has received significant research interest as the number of productive wells has increased. The Woodford is productive over a wide range of thermal maturity (based upon vitrinite reflectance), yet most clay mineral studies report primarily illite (Caldwell, 2011 & Whittington, 2009). A previous report contrasts this behavior to other late Paleozoic shales in Oklahoma (Kowal, 2016). The major difference between these units is the amount of organic matter, which is much higher in most Woodford samples.

In this study, Woodford shale samples were analyzed for several different characteristics, and combined with organic fraction data from previous work on the same samples (Lambert, 1993). Clay mineralogy was determined using an X-ray diffractometer (XRD) with the goal of finding the amount, and the degree of crystallinity of illite in a suite of samples. X-ray fluorescence (XRF) analysis was conducted to determine the variability of elemental concentrations within the samples. The bulk powder XRD data were combined with the major element concentrations to calculate mineral percentages. These data were compared to thermal maturity based upon vitrinite reflectance and T_{\max} values to determine the role of burial diagenesis on the clay mineralogy within Woodford Shale.

The predominant clay mineral found within the samples was illite, with no recognizable mixed-layer smectite present, suggesting illitization is occurring early in the diagenetic process. A positive correlation between K/Rb ratios and TOC was found, supporting the control of organic matter on potassium in shales. No correlation between amount illite and thermal maturity was found, providing more evidence for the theory that high amounts of organics are driving illitization rather than thermal maturity.

Table of Contents

List of Figures	vi
List of Tables	viii
Acknowledgements	ix
Dedication	x
Chapter 1 - Introduction	1
1.1 – Geologic Setting	2
1.2 – Stratigraphy	3
1.3 – Previous Investigations	6
Chapter 2 - Methodology	10
2.1 – Sample Selection	10
2.2 – XRF Analysis	13
2.3 – XRD Analysis	14
2.3.1 – X-Ray Diffraction Methods	14
2.3.2 – Bulk Powder Analysis	15
2.3.3 – Clay Analysis	16
Chapter 3 - Results	21
3.1 – XRD Bulk Powder Analysis	22
3.2 – XRD Untreated Clay Slide Analysis	23
3.3 – XRD Ethylene-Glycolated Clay Slide Analysis	24
3.4 – XRF Elemental Analysis	24
3.5 – Geochemical, thermal maturity, and crystallinity data	27
3.6 – Calculated Mineralogy	28
Chapter 4 - Discussion	30
4.1 – Sample Problems	30
4.2 – Illitization	32
4.3 – Clay Mineralogy	33
4.4 – Thermal Maturity	36
4.5 – K/Rb Ratio	37
4.6 – Mineralogical Variation with Tmax	40

4.7 – Total Organic Carbon (TOC).....	41
Chapter 5 - Conclusion	44
References.....	46
Appendix A -	49

List of Figures

Figure 1. Map showing present day Oklahoma and its geologic provinces (Northcutt and Campbell, 1996).....	3
Figure 2. Generalized stratigraphic column for the Anadarko Basin with oil and gas source rocks (red text) (Higley, 2014).	5
Figure 3. Relationship between mean vitrinite reflectance and illite crystallinity index (Guthrie et. al., 1986).	7
Figure 4. Relationship between mean vitrinite reflectance and illite sharpness ratio for data pooled from Stanley, Jackfork and Atoka shales (Guthrie et al., 1986).	8
Figure 5. Woodford shale compared to Ouachita Shales (Kowal, 2016).	9
Figure 6. Locations of all 14 samples.	11
Figure 7. Cuttings from the 14 samples.	11
Figure 8. Bruker Tracer III-SD handheld XRF.....	14
Figure 9. Panalytical Empyrean X-Ray Diffractometer.	15
Figure 10. Vacuum pump and filter apparatus used to create clay slides.	19
Figure 11. Examples of completed clay slides.....	20
Figure 12. XRD bulk powder analysis for sample KC10.	22
Figure 13. Untreated clay slide XRD analysis for sample KC10.	23
Figure 14. XRD analysis for ethylene-glycolated clay slide KC10.....	24
Figure 15. Mean vitrinite reflectance vs Weaver's sharpness ratio. Solid line represents the trendline for the Ouachita shales found in Guthrie et. al. (1986) (Figure 4).	32
Figure 16. Diffraction pattern for glycolated sample KC06.	34
Figure 17. Diffraction pattern for air-dried sample KC06.....	35
Figure 18. Diffraction pattern for glycolated sample OC02. Note the suppressed clay peaks and high dolomite and quartz peaks.	36
Figure 19. Tmax vs depth.	37
Figure 20. Tmax vs K/Rb ratios.....	39
Figure 21. Tmax vs K/Rb without samples OC02, OC03, OC04, OC05.	39
Figure 22. Calculated illite percentages vs Tmax.	41
Figure 23. K/Rb vs. TOC (wt%).	41

Figure 24. TOC vs Tmax.	42
Figure 25. Mo (ppm) vs TOC (wt%).	43

List of Tables

Table 1. Names and locations of the 14 samples used in this study.	12
Table 2. Particle size separation with centrifuge, created by Dr. LaCroix.	17
Table 3. XRF analysis of major elements reported in wt%.	24
Table 4. XRF analysis of trace elements reported in ppm.	25
Table 5. Results of XRF standards for major elements including average and standard deviation values.	26
Table 6. Results of XRF standards on trace elements including average and standard deviation values.	26
Table 7. Geochemical and calculated data for all 14 samples. * = Denotes data obtained from StratoChem Services. All other TOC, Tmax, and vitrinite reflectance values provided by Lambert (1993).	27
Table 8. Calculated mineralogy using XRF data reported in wt%.	29
Table 9. Hydrocarbon generation zones for Tmax values (Beaumont and Foster, 2000).	37
Table 10. Correlation coefficients of calculated mineral percentages vs Tmax.	40

Acknowledgements

I would like to thank Dr. Matthew Totten for all of his guidance and allowing me to work under him, along with Dr. Sambhudas Chaudhuri and Dr. Abdelmoneam Raef for their support along the way. I would like to thank Dr. Michael Lambert for allowing me to use his core samples and data. I would also like to thank Dustin Harris for his joint effort and help with this thesis.

Dedication

I would like to dedicate this thesis to my entire family. Without their continued support and motivation to succeed, I would have never completed this program.

Chapter 1 - Introduction

The study of clay minerals is commonplace in oil and gas exploration. In early exploration years, clay minerals were used as a point of analysis to estimate source rock quality as well as hydrocarbon generation zones. Later, with the advent of X-ray diffraction, clay minerals have been used extensively during petroleum system analysis which, includes pinpointing the timing of hydrocarbon generation times (Jiang, 2012).

One particular area of interest is the smectite to illite transition. The diagenetic temperatures required to drive the transformation of smectite to illite have been reported to coincide with the temperatures needed for the onset of oil generation from organic matter (Jiang, 2012; Hower et al., 1976). Thermal maturity based upon vitrinite reflectance is the most used indicator in industry, but the degree of illitization has been proposed as an alternative indicator (Weaver, 1960) because of their reported covariance.

As many authors have reported, more than just a temperature increase with increased burial depth is needed to drive this transformation from smectite to illite (e.g., Boles and Franks, 1979). Potassium and aluminum are required for this reaction to occur, which are often thought to be supplied from an outside source. One widely accepted theory calls for the dissolution of K-feldspar to provide the needed potassium and aluminum (Boles and Franks, 1979). However, in many cases it is seen that all of the K-feldspar is gone, yet there is still significant remaining smectite (Totten and Blatt, 1993). This begs the question: where is the remaining potassium coming from? Several other models have been proposed, but most are focused in areas of conventional shales and formations (Polastro, 1985). Very little information and studies exist on potassium sources and illitization in marine, organic-rich “tight” shales that are the target of

unconventional exploration. These organic-rich shales are reported to contain mostly illite, with little mixed-layer content (Caldwell, 2011 & Whittington, 2009).

In this study, 14 Woodford shale samples were analyzed for a variety of data including degree of illitization, whole-rock chemistry, total organic carbon and vitrinite reflectance. A major goal of this work is to investigate whether the clay transformations reported in “typical” shales during burial occur within an organic-rich black shale.

1.1 – Geologic Setting

Formation of the Anadarko Basin in Oklahoma began with the breakup of Pangea and the subsequent development of the Tethys Ocean, occurring in the late Precambrian to early Cambrian (Feinstein, 1981). In the Precambrian, what is now the southern region of Oklahoma, was rifted forming the Oklahoma aulacogen (Hoffman, et al., 1974). The area was faulted in the Early Cambrian, allowing for intrusion of igneous rocks, which ended by the Middle Cambrian. Subsequent cooling caused accelerated subsidence which allowed for a large accumulation of sedimentary deposits throughout the Paleozoic Era. The collision of the Laurentia and Gondwana plates in the Late Paleozoic resulted in the Wichita and Ouachita orogenies, which created the Wichita Mountains and Amarillo arch (Higley, 2014). The thrusting of the Wichita Mountains and Amarillo uplift over the Oklahoma aulocogen resulted in a large amount of continued subsidence, forming the Anadarko Basin (Webster, 1980).

Today, the Anadarko Basin contains the thickest section of Paleozoic sedimentary rocks on the North American craton, reaching thicknesses over 36,000 feet in the deepest parts (Garner and Turcotte, 1984). It covers most of western Oklahoma but also extends northward into southwestern Kansas, southward into the Texas Panhandle, and into southeastern Colorado. The Basin contains 25 oil and gas plays, with only one, the Woodford/Chattanooga shale, being the

main unconventional play. It is bounded by several uplifts. The Wichita-Amarillo Uplift to the south, the Cimarron and Las Animas Arches to the west, the Central Kansas Uplift to the north, the Pratt Anticline to the northeast, the Nemaha Uplift to the east, and the Southern Oklahoma fold belt to the southeast (Figure 1).

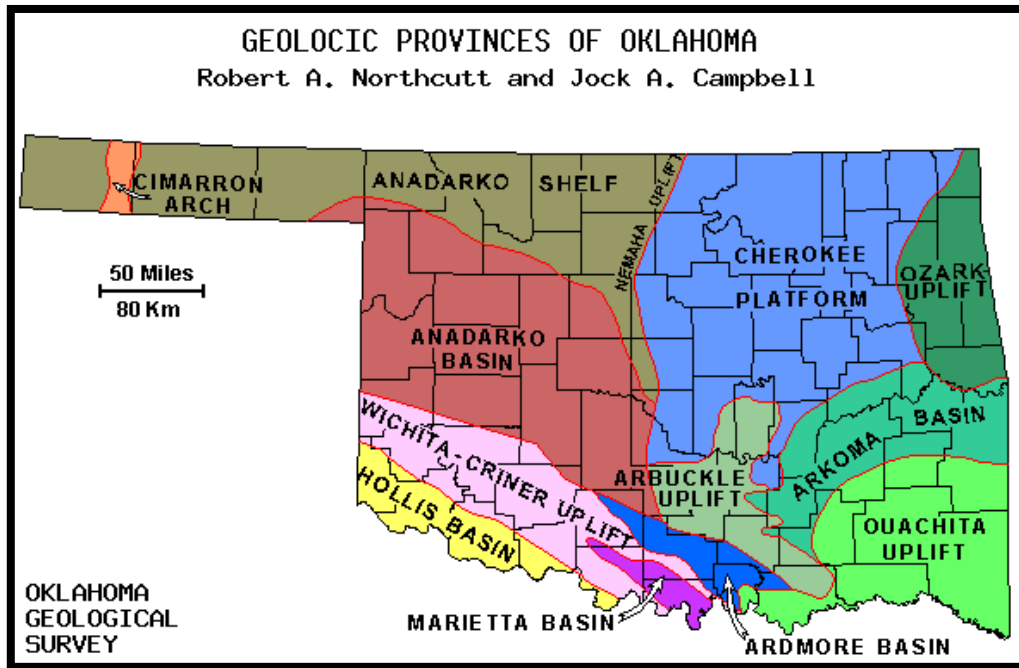


Figure 1. Map showing present day Oklahoma and its geologic provinces (Northcutt and Campbell, 1996).

1.2 – Stratigraphy

Strata within the Anadarko Basin range from Cambrian to Permian in age (Figure 2). In the Late Devonian, a major unconformity developed (Amsden, 1975). The basin then underwent a major marine transgression which allowed for the deposition of the organic-rich Woodford shales throughout the Late Devonian and into the Early Mississippian (Johnson and Cardott, 1992). Following Woodford deposition, sea levels receded leaving shallow, oxygenated waters.

Benthic organisms thrived, eventually creating the limestones of early Mississippian (Kinderhookian) age which now conformably overlie the Woodford.

The Woodford shale is organic-rich with total organic content (TOC) levels ranging from 0.4%-25% (Cardott and Lambert, 1985). It also has recorded vitrinite reflectance values (R_o) from 0.48% to over 5% in Oklahoma (Cardott and Lambert, 1985). Thicknesses range from virtually zero in the northern part of the Anadarko Basin and increase to more than 900 feet in some parts of the deep basin (Amsden, 1975).

System	Series	Lithostratigraphic Unit (HC Source Rocks in Red)	
Permian (part)	Leonardian	Sumner Gp; Enid Gp.; Hennessey Gp.	
	Wolfcampian	Chase Group Council Grove Group Admire Group	Pontotoc Group
Pennsylvanian	Virgilian	Wabaunsee Group Shawnee Group	Ada Group
		Douglas Group	
	Missourian	Lansing Group Kansas City Group	Hoxbar Group
	Desmoinesian	Marmaton Group Cherokee Group	Deese Group
	Atokan	Atoka Gp.; Thirteen Finger limestone	
	Morrowan	Morrow Gp./Fm.; lower Dornick Hills Gp.	
Mississippian	Chesterian	Springer Formation Chester Group	Mayes Group
	Meramecian	Meramec lime	
	Osagean	Osage lime	
	Kinderhookian	Kinderhook Shale	
Devonian	Chautauquan	Woodford Shale, Chattanooga Shale	
	Senecan	Misener sand	
	Erian Ulsterian		
Silurian	Cayugan Niagaran Alexandrian	Hunton Group	
Ordovician	Cincinnatian	Sylvan Shale; Maquoketa Shale	
		Viola Group/Formation	
	Champlainian	Simpson Group	
Cambrian (part)	Canadian	Arbuckle Group	
	Trempealeauan		
	Franconian	Reagan Sandstone	

Figure 2. Generalized stratigraphic column for the Anadarko Basin with oil and gas source rocks (red text) (Higley, 2014).

1.3 – Previous Investigations

There are a number of relevant previous studies pertaining to this thesis study. Kowal (2016) summarized previous work pertaining to vitrinite reflectance values and correlation with illitization. It was found that within the Woodford, illitization had progressed extensively, even with lower vitrinite reflectance values, when compared to shales with lower organic content. A suggested explanation for this was the high levels of organic matter in the Woodford supplying enough potassium to accelerate illite transformation (Kowal, 2016).

Totten et al. (2007) examined well cuttings in the Ship Shoal area, Gulf of Mexico. It was found that the increase in K_2O content needed for illite formation was only weakly related to depth. This suggests the required elements may be coming from within the rock itself, and not introduced from an external source (Totten et al., 2007).

Another study reported relationships between vitrinite reflectance, illite crystallinity, and organic geochemistry in the Ouachita Mountains, Oklahoma and Arkansas (Guthrie et al., 1986). The shales in this study are of similar age (Mississippian and Pennsylvanian) as the Woodford (Late Devonian-Mississippian) and are nearby the Woodford in Oklahoma. It was found the relationships between vitrinite reflectance and illitization in the Ouachita shales follow a more traditional pattern, unlike in the Woodford (Guthrie et al., 1986). Figure 3 and Figure 4 display

the relationships between two of the common indicators of illitization and vitrinite reflectance for the Stanley, Jackfork, and Atoka shales.

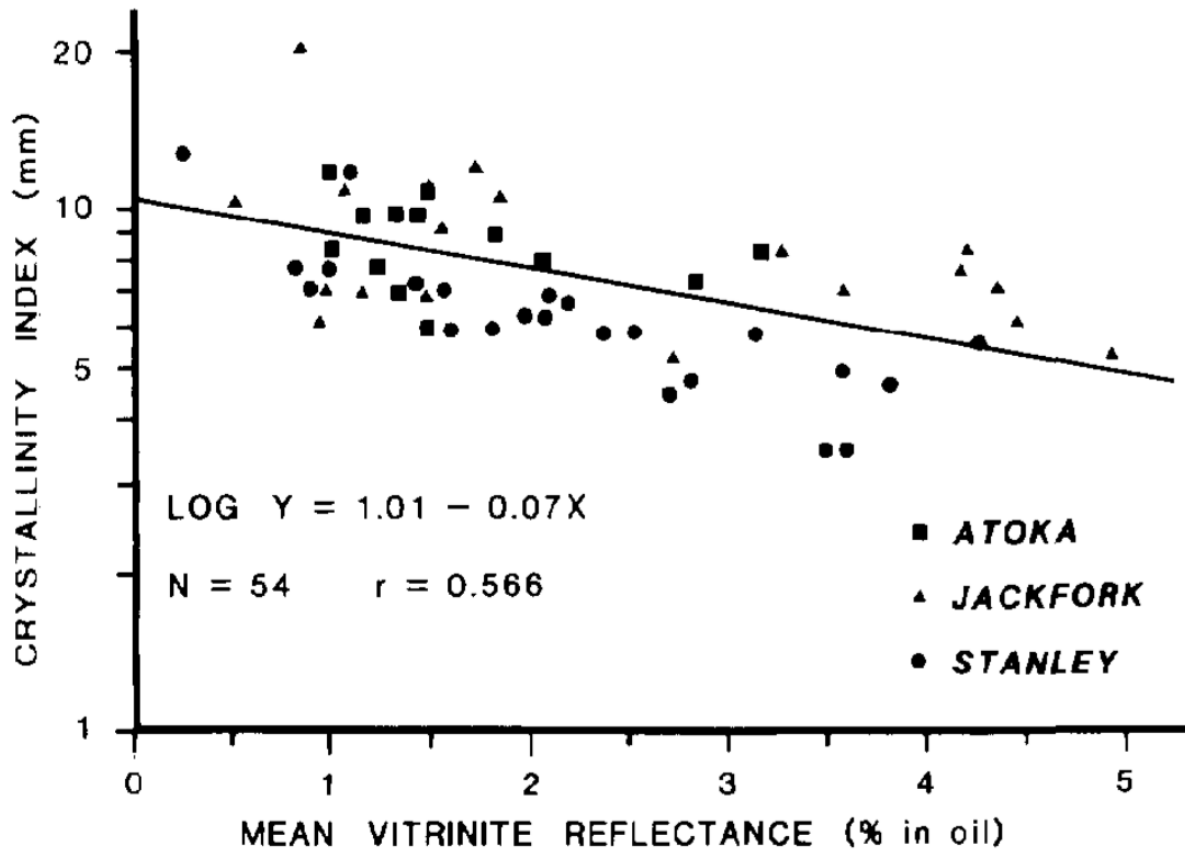


Figure 3. Relationship between mean vitrinite reflectance and illite crystallinity index (Guthrie et. al., 1986).

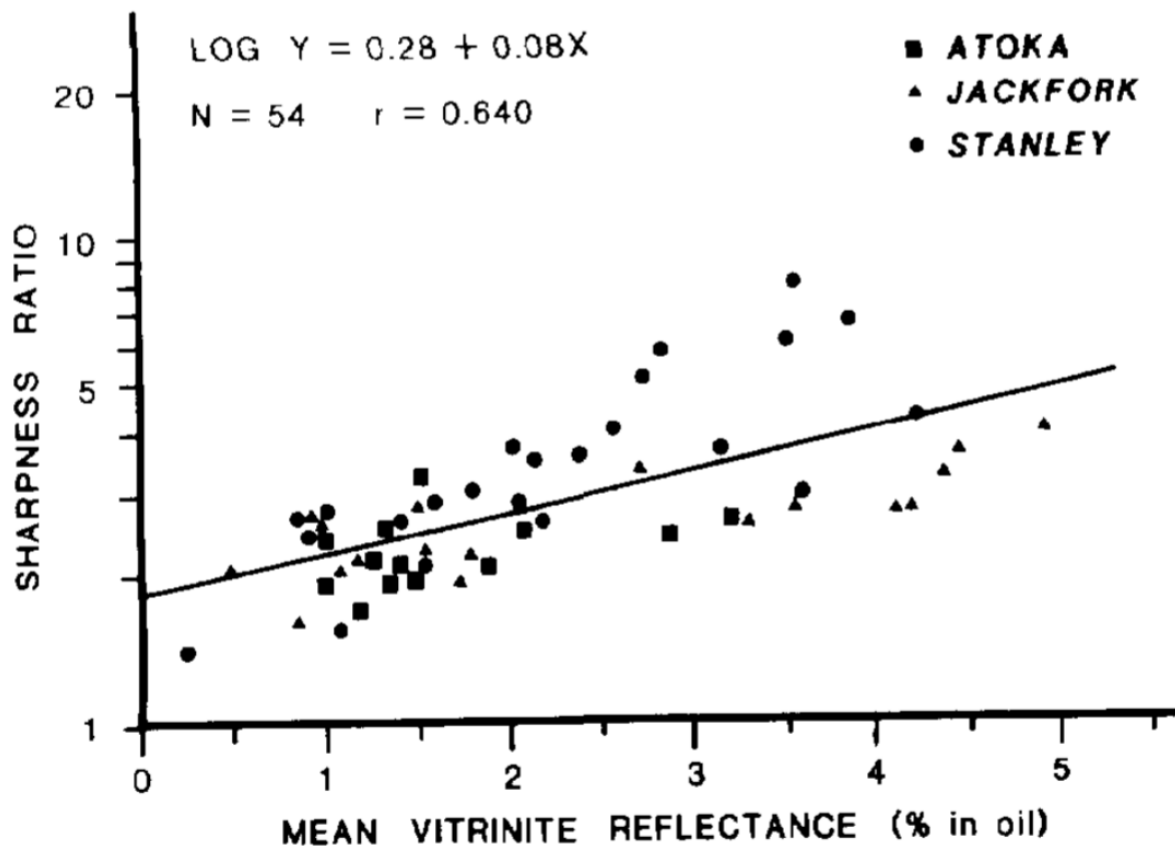


Figure 4. Relationship between mean vitrinite reflectance and illite sharpness ratio for data pooled from Stanley, Jackfork and Atoka shales (Guthrie et al., 1986).

As observed, vitrinite values appear to have a direct relationship with illitization in the Ouachita samples. However, in contrast, Woodford shale show no such correlation and exhibit high sharpness ratios, even at low vitrinite reflectance values (Figure 5). The main difference between these shales is the amount of organic matter. As previously stated, TOC values within the Woodford can be up to 25%, whereas TOC values in the Ouachita were reported as less than 1.5% (Guthrie et al., 1986). A possible explanation for the accelerated illitization may be available potassium contained within the organic matter in the Woodford. This has been previously suggested by Totten et. al. (2013).

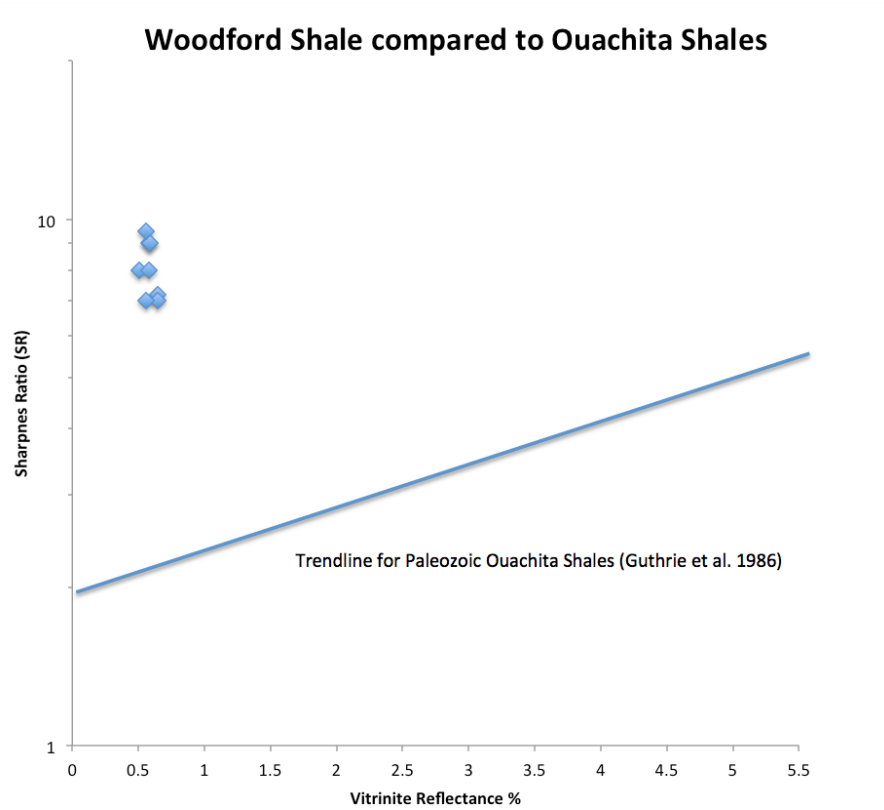


Figure 5. Woodford shale compared to Ouachita Shales (Kowal, 2016).

Chapter 2 - Methodology

2.1 – Sample Selection

The samples used in this study were selected due to their availability and relevance of previous analysis completed on them. Of the fourteen samples used, thirteen were provided by Dr. Michael Lambert. Dr. Lambert originally collected the samples in 1985 from the Oklahoma Petroleum Information Center (OPIC) core library as well as the Kansas Geologic Survey (KGS) for use in his dissertation. The samples are all from Woodford shale, and represent a wide spatial arrangement across 11 counties in Oklahoma and 3 counties in Kansas (Figure 6). A compiled list of well names and locations can be seen in Table 1. The samples were originally cores; however full cores were not necessary for use in this study. The cores were cut on both ends using a table saw to produce flat, parallel surfaces for use in Dustin Harris's study (2017). Roughly 15 grams of the excess cuttings of each sample were then collected for use in this study (Figure 7).



Figure 6. Locations of all 14 samples.

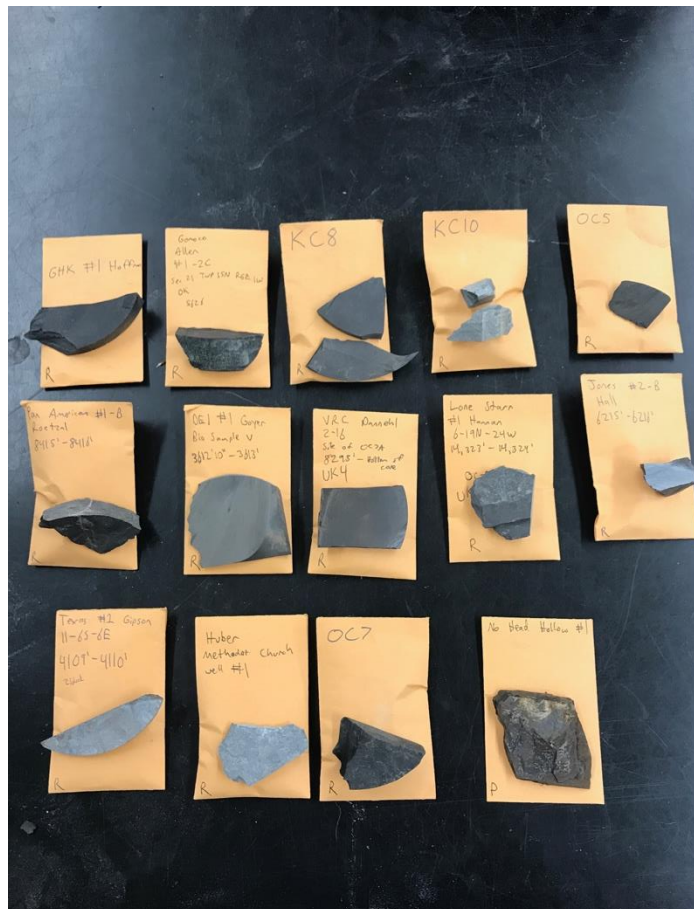


Figure 7. Cuttings from the 14 samples.

<u>Sample</u>	<u>Name</u>	<u>Section</u>	<u>Township</u>	<u>Range</u>	<u>County</u>
KC06	APC-DEI #1 Goyer	25	30S	01E	Sumner
KC08	ERDA #1 Bock	15	23S	12E	Greenwood
KC10	Dalmac #1 Allen	7	17S	03W	McPherson
OC02	Texas #1 Gipson	11	06S	06E	Marshall
OC03	Universal #2-16 Dannehl	16	13N	06W	Canadian
OC04	Gomoco Allen #1-26 Gaffe	21	15N	01W	Logan
OC05	Tenneco #1-11 Edwards	11	21N	14W	Garfield
OC06	Huber #1 Cherokee Methodist	21	26N	11W	Alfalfa
OC07	Calvert #2 Bloyd	21	27N	15W	Woods
OC08	GHK Hoffman #1	1	14N	16W	Custer
OC09	Lone Star #1 Hanan	6	19N	24W	Ellis
OC20	Jones #2-B Hall	36	07N	13W	Caddo
OC25	Pan American #1-B Roetzal	13	19N	10W	Blaine
NHH1	No Head Hollow #1	12	17N	22E	Cherokee

Table 1. Names and locations of the 14 samples used in this study.

One sample, No Head Hollow #1, was collected in person at a Woodford shale outcrop in Cherokee County, Oklahoma by Dustin Harris and the author. The original intent of the trip was to obtain a core of the outcrop using a handheld coring tool. However, a combination of the highly fissile nature of the shale at the outcrop, along with an insufficiently sharp drill bit, proved it impossible to retrieve a solid core. Nonetheless, shavings and chunks of rock were easily obtainable which were sufficient for this study.

To prepare the samples for further analyses, large cuttings of core were ground down by hand in a mortar and pestle. Care was taken to thoroughly clean the mortar and pestle between grindings so as not to cross-contaminate samples. For this particular analysis, no specific grain size was desired; however, it appeared most samples were ground to a very coarse sand size and smaller (<2mm). Samples were carefully divided into representative cuts for each analysis.

2.2 – XRF Analysis

X-Ray Fluorescence analysis was performed on the samples to determine their elemental composition. Aliquots of each sample were loaded into analysis cups. Analysis was then performed using the Bruker Tracer III-SD handheld XRF provided by Kansas State Geology (Figure 7). Major elemental analysis was performed with a vacuum and no filter with settings at 15kV, 25 μ A, and in intervals of 180 seconds. Trace elemental analysis was performed with no vacuum and a yellow filter (12 mil Al + 1 mil Ti) with settings at 40kV, 12.4 μ A, and in intervals of 120 seconds. Two different standards for both major and trace elements were analyzed before and after the suite of samples, to determine calibration and check for accuracy of the analyses. The first standard was provided by the machine's manufacturer, Bruker, and the second standard was a Woodford Shale standard created by Dr. Harry Rowe of UT Austin. Concentrations in weight percent (wt%) for the major elements, and ppm for the trace elements, were calculated for each element by comparison to the known values of the standards. Assistance in collecting and calculating the elemental data was provided by XRF technician Ian Andree.

It is important to note that due to the low penetrating power and energy of the handheld XRF, elements with a light atomic weight (Mg and below) are nearly immeasurable when analyzed in air. This can be solved by using helium as a controlled atmosphere in the chamber to eliminate the dispersing effect of air. However, at the time of this analysis, no such accommodations were available.



Figure 8. Bruker Tracer III-SD handheld XRF.

2.3 – XRD Analysis

2.3.1 – X-Ray Diffraction Methods

X-ray diffraction methods have become common practice in identifying clay minerals, but are also useful in determining bulk mineralogy. X-rays are aimed at samples which produce different diffraction patterns that show the intensity of x-rays at a specific 2 theta angle. X-ray diffraction analysis was performed using the Panalytical Empyrean provided by Kansas State

Geology (Figure 9). In this study, XRD analysis was divided into three different analyses: bulk powder, untreated clay slide, and glycolated clay slide analysis.



Figure 9. Panalytical Empyrean X-Ray Diffractometer.

2.3.2 – Bulk Powder Analysis

The goal of bulk powder analysis was to provide insight on the generalized bulk mineralogical composition of the Woodford samples. For this, powdered sample must be tightly packed in a round analysis disk and contain as little air space as possible. To achieve this, samples were placed in a steel mortar and pestle and rigorously ground by hand. The resulting powder was then dumped onto a 230 mesh sieve and sifted, the resultant being samples less than 63 microns in size. This process was continued until enough <63 micron powder of each sample to fill the disks was obtained. Powder was then tightly packed into the disks and then analyzed

with the XRD. Analysis was completed using the Panalytical Empyrean with the PIXcel 3D using a copper anode. Samples were analyzed from $2-47^{\circ}2\theta$ with a step size of $0.007^{\circ}2\theta$. Generator settings were 40mA, 45 kV and scanning was continuous, taking a total of 20 minutes per scan.

2.3.3 – Clay Analysis

Because of the poor structure factor in clays, oriented mounts were prepared to enhance basal reflections, which give d-spacing of the basal layer (which represent the thickness of the phyllosilicate layers) (Faure, 1998). Clays normally produce broad peaks which can be compared to known diffraction patterns for identification. Particularly in the context of illite crystallinity, peaks are usually measured at full width at half maximum, known as the Kübler index (Eberl and Velde, 1989). Degree of illite crystallinity can also be calculated by Weaver's sharpness ratio, which is measured by the diffractogram peak height at 10.0 \AA divided by peak height at 10.5 \AA (Weaver, 1960). Either crystallinity measure may be used, as they show strong correlation. Because the Weaver sharpness ratio may be calculated directly from the diffraction excel sheet, the Weaver index was used in this study.

The next step in the XRD analysis was to create clay slides to discover the type of clays present in the samples. Clay minerals often have similar X and Y dimensions, while the Z dimension is the best diagnostic character which represents the height of the T-O (tetrahedral-octahedral) or T-O-T layer (Moore and Reynolds, 1989). Since well-crystallized, pure samples are ideal for X-ray diffraction, and clays rarely are both, some preparation must be done in attempt to separate the clay particles and orient them to increase basal reflection. Preparation began by obtaining approximately 5 grams of finely powdered sample using the same method as above with the 230 mesh screen. To separate out the clay-size fraction ($<2 \mu\text{m}$), criteria from

Table 2 was used. The table was created from a modification of Stoke's law by Dr. Brice LaCroix of Kansas State University. Approximately 5 grams of the powdered sample was suspended in 200 milliliters of water, and spun in a centrifuge at 1000 rpm for 90 seconds. The top liquid in the centrifuge tubes was then quickly siphoned out and into a beaker. The resultant was a suspension of liquid containing particles of only 2 microns or less.

	<u>Size of Particle (μm)</u>			
	16	5	2	1
<u>Velocity (r.p.m)</u>	<u>Centrifuge time (in minutes)</u>			
500	0.09	0.96	5.98	23.94
750	0.04	0.43	2.66	10.64
1000	0.02	0.24	1.50	5.98
1250	0.01	0.15	0.96	3.83
1500	0.01	0.11	0.66	2.66
1750	0.01	0.08	0.49	1.95
2000	0.01	0.06	0.37	1.50
2250	0.00	0.05	0.30	1.18
2500	0.00	0.04	0.24	0.96
2750	0.00	0.03	0.20	0.79
3000	0.00	0.03	0.17	0.66
3250	0.00	0.02	0.14	0.57
3500	0.00	0.02	0.12	0.49
3750	0.00	0.02	0.11	0.43
5500	0.00	0.01	0.05	0.20
5000	0.00	0.01	0.06	0.24
25000	0.00	0.00	0.00	0.01

Table 2. Particle size separation with centrifuge, created by Dr. LaCroix.

To transfer particles onto a glass slide suitable for XRD analysis, a modification of the Filter Transfer Method was used (Moore and Reynolds, 1989). The liquid suspension is poured into a vacuum filtering apparatus above a $0.45\mu\text{m}$ Millipore filter. Vacuum is applied below the filter, which draws the suspension downward (Figure 10). The particles are caught by and

accumulate on the filter. Once all of the suspension was filtered, the vacuum pump was shut off, and the filter removed from the apparatus. The filter was then glued face up onto a glass slide using Elmer's glue, and the overhanging edges trimmed to fit the slide. Once allowed to dry for at least 24 hours, the clay slides were then ready for XRD analysis (Figure 11). Successful use of this method was reported by Totten and Hanan (2002).

Analyses were completed using the Panalytical Empyrean with the PIXcel 3D using a copper anode. Samples were analyzed from $2-40^{\circ}2\theta$ with a step size of $.007^{\circ}2\theta$. Generator settings were 20mA, 35 kV and scanning was continuous, taking a total of 20 minutes per scan.

After all scans were completed on the untreated slides, slides were then treated with ethylene glycol for identification of expanding clays, particularly smectite. This method of identification was first discovered by Bradley (1945). To fully saturate the samples, slides were placed in a desiccator containing an ethylene glycol atmosphere for a minimum of 24 hours at room temperature. Once fully saturated, slides were singularly removed and quickly analyzed (to minimize EG loss due to evaporation) on the XRD using the same criterion as the unsaturated slides.

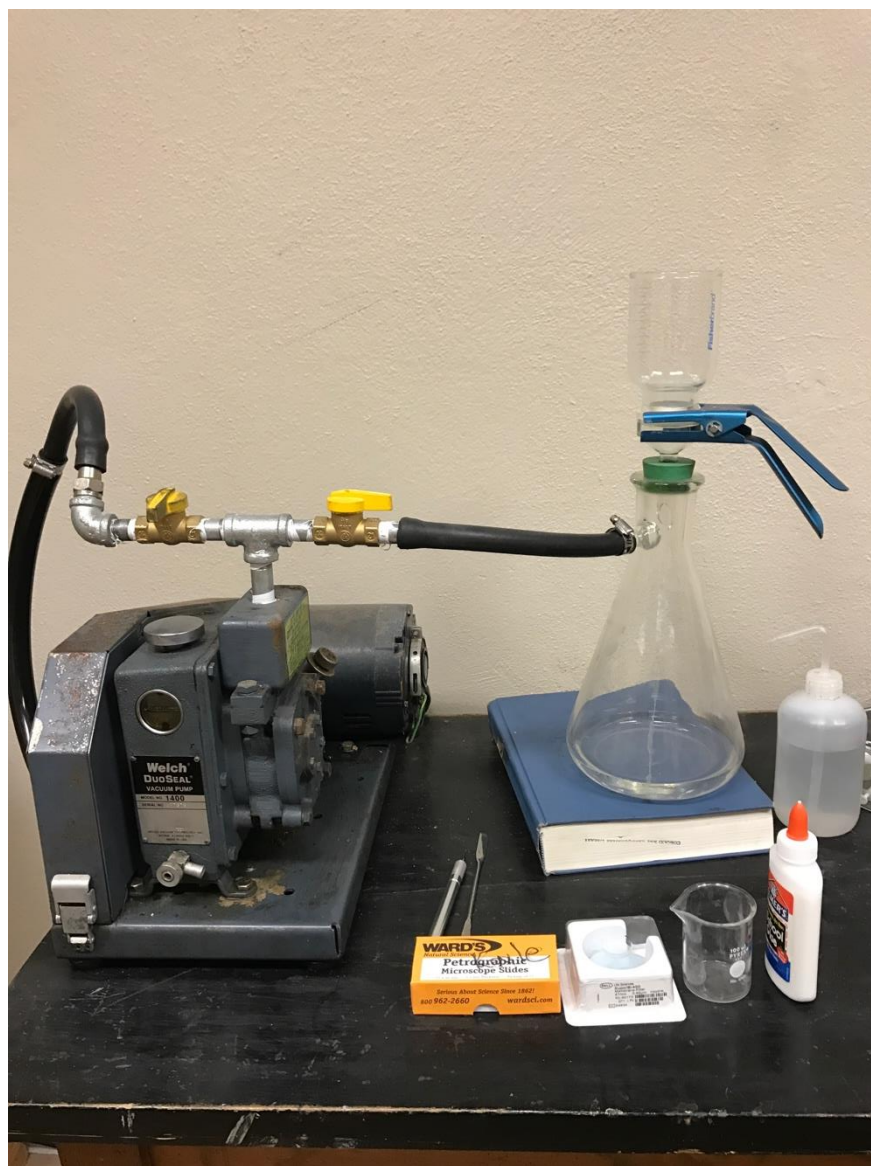


Figure 10. Vacuum pump and filter apparatus used to create clay slides.

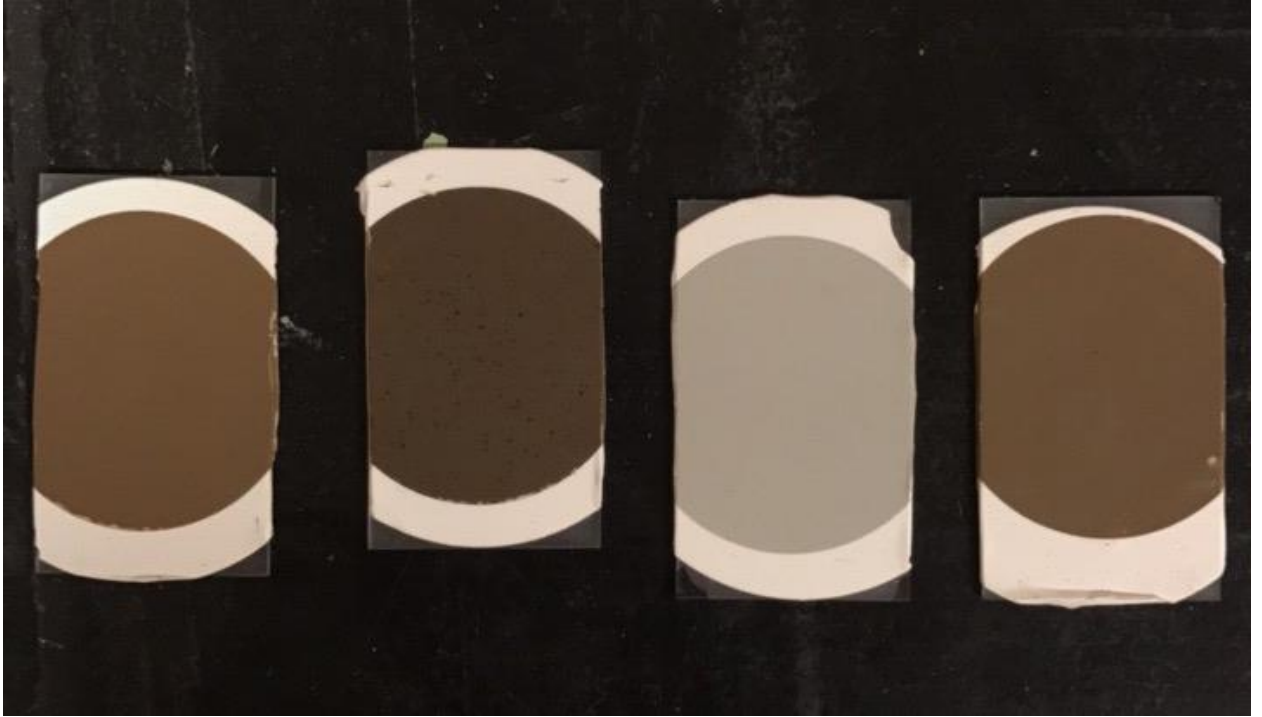


Figure 11. Examples of completed clay slides.

Chapter 3 - Results

Results from XRD bulk powder, untreated clay slides, ethylene glycolated clay slides, as well as XRF major and trace element data are displayed below. Results of the XRF standards run throughout analysis are shown in Tables 5 and 6. These include averages and standard deviation values on the standards, showing analytical accuracy throughout analysis. Appendix A.5 – 1 shows a table demonstrating the analytical uncertainty of the instrument by comparing the data collected on standard RTC-W-220 (which was analyzed at the same time as the samples) to published values for this standard. For the XRD analysis, only one example of spectra is shown for the bulk mineralogy, one for the untreated clay slides, and one for the glycolated clay slides (Figures 12, 13, 14). A complete list of spectra for all XRD analyses are listed in Appendix A, including a figure of interpreted peaks (Appendix A.5-1). Also shown is a table of geochemical and calculated data including TOC, vitrinite reflectance, T_{\max} , Weaver's ratio, depth, and K/Rb ratios (Table 7). Lastly, a calculated mineralogy was completed on all samples by Harris (2017).

3.1 – XRD Bulk Powder Analysis

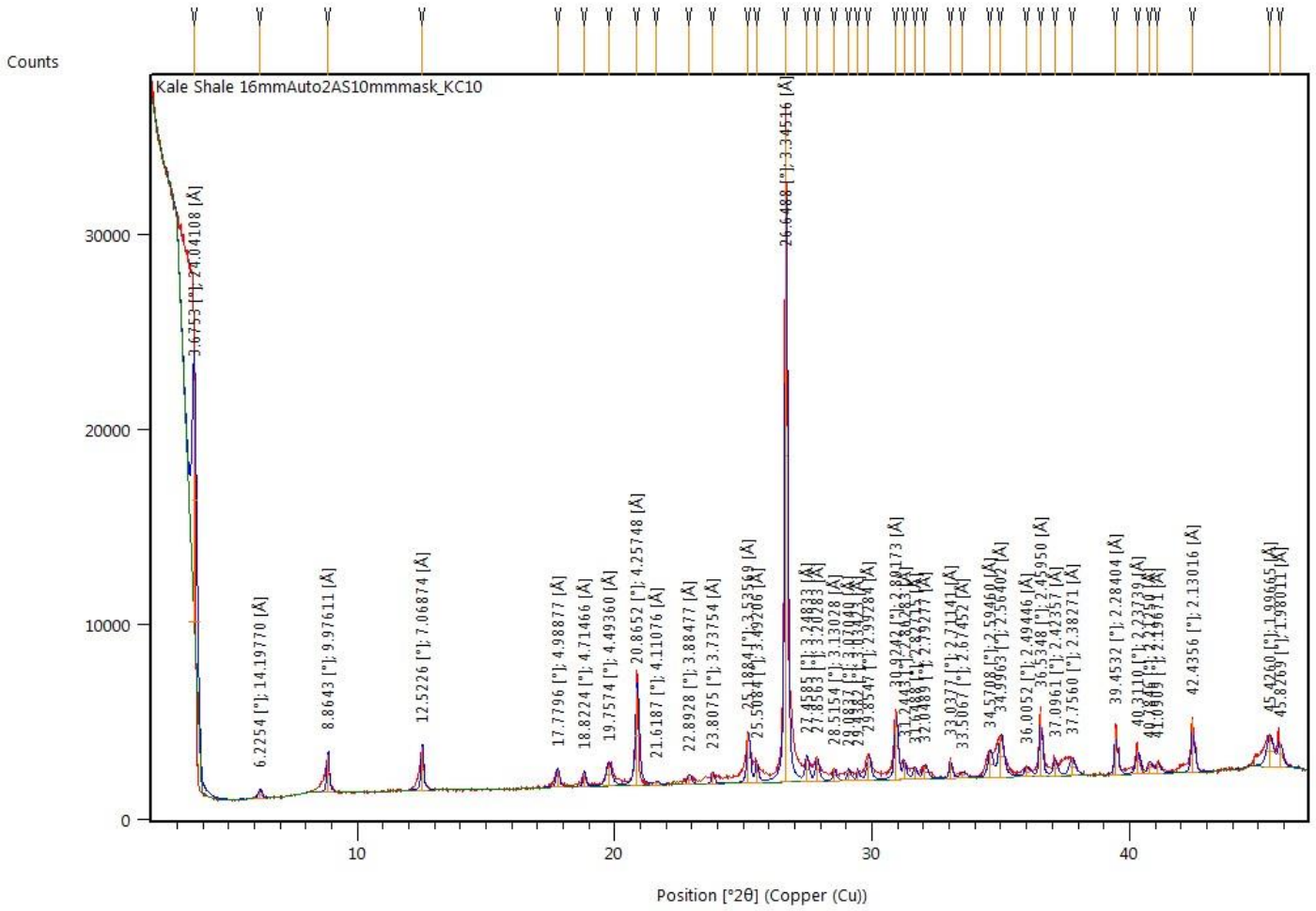


Figure 12. XRD bulk powder analysis for sample KC10.

3.2 – XRD Untreated Clay Slide Analysis

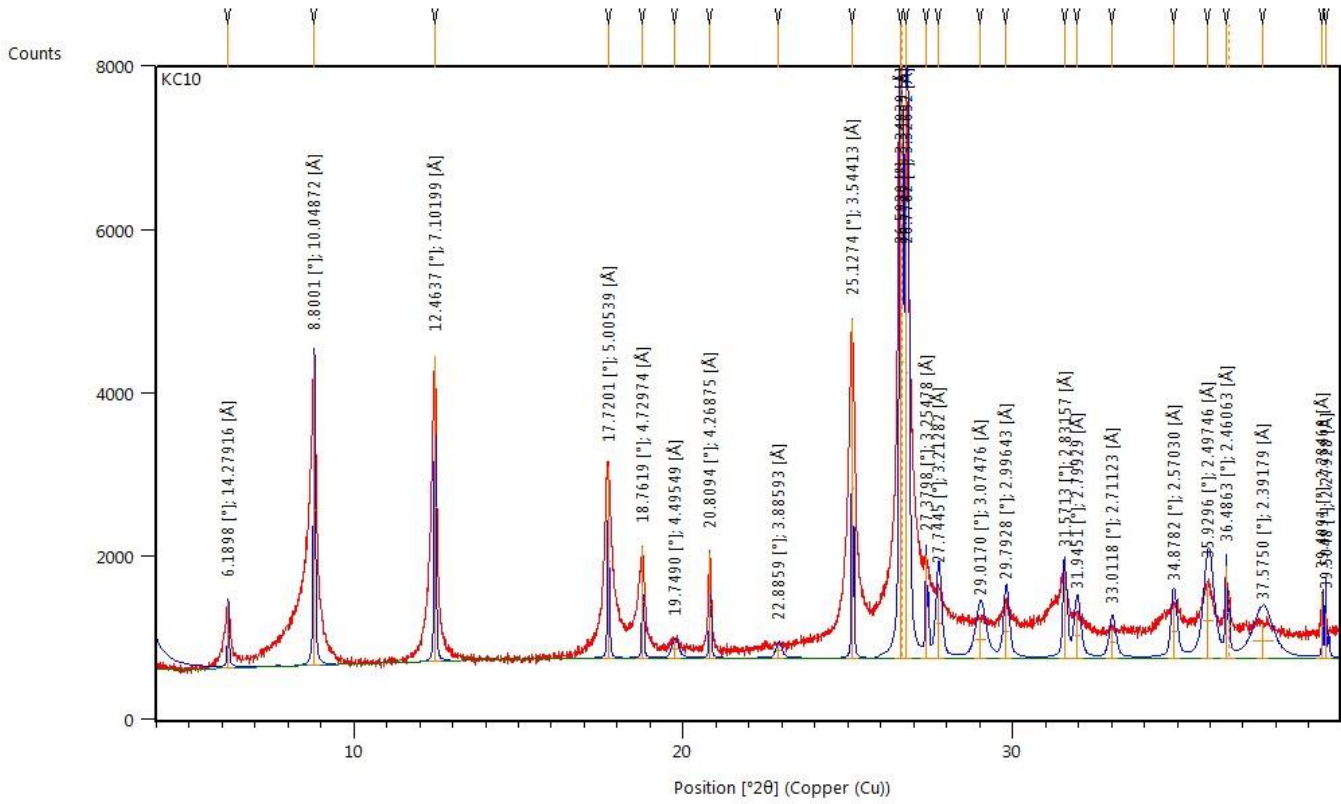


Figure 13. Untreated clay slide XRD analysis for sample KC10.

3.3 – XRD Ethylene-Glycolated Clay Slide Analysis

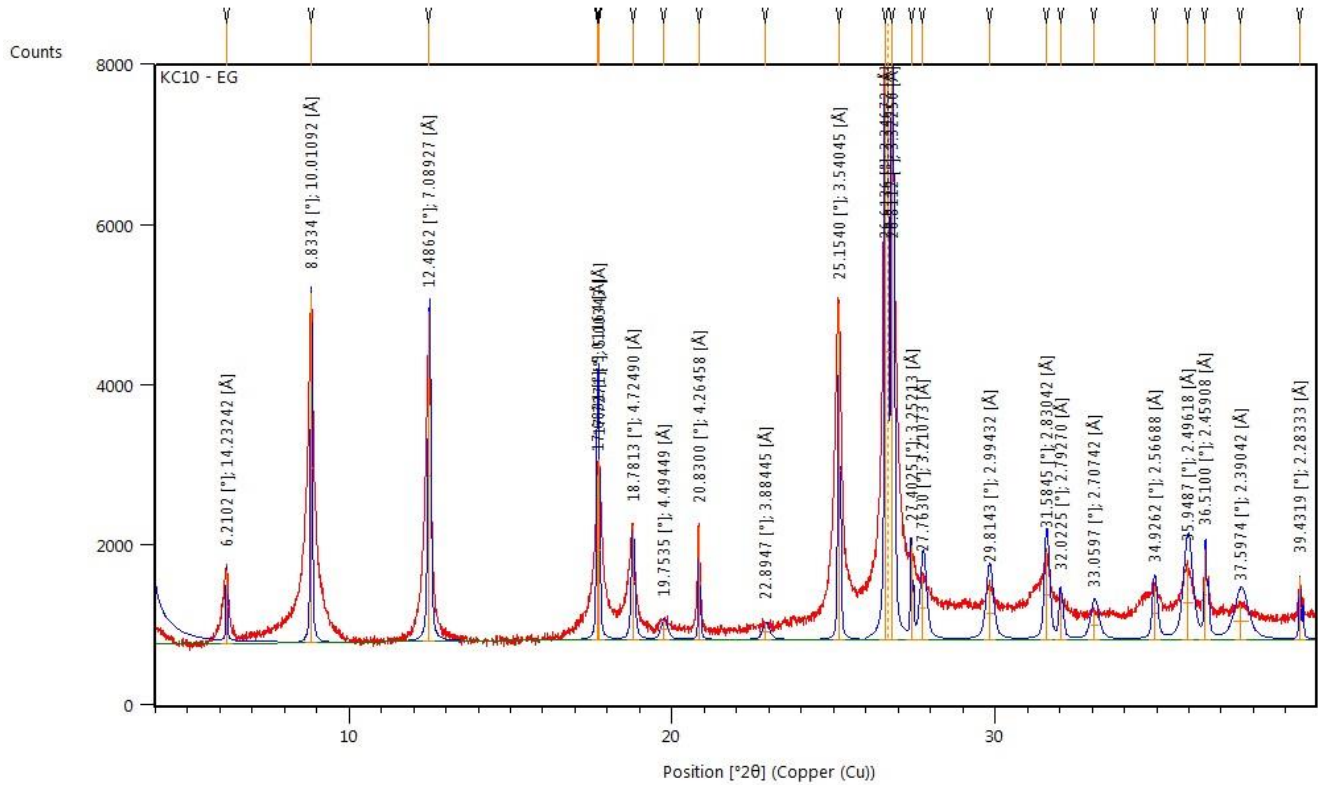


Figure 14. XRD analysis for ethylene-glycolated clay slide KC10.

3.4 – XRF Elemental Analysis

Sample	Wt% of Major Elements										
	Al	Si	P	S	K	Ca	Ti	V	Cr	Mn	Fe
KC06	6.46	20.58	0.03	0.98	3.67	1.67	0.43	0.01	0.01	0.03	3.81
KC08	6.17	16.22	0.03	1.04	4.54	0.84	0.44	0.02	0.01	0.03	3.79
KC10	6.42	16.52	0.03	0.76	4.15	0.98	0.45	0.01	0.01	0.03	4.24
OC02	1.43	20.50	0.06	0.36	0.95	6.82	0.15	0.01	0.01	0.03	0.89
OC03	2.89	31.34	0.04	0.85	1.45	0.34	0.21	0.06	0.01	0.03	1.15
OC04	3.00	19.02	0.02	2.01	1.97	2.42	0.28	0.01	0.01	0.03	2.87
OC05	3.21	24.48	0.04	0.46	2.59	0.23	0.28	0.09	0.01	0.02	1.34
OC06	5.14	15.54	0.03	1.43	3.90	3.66	0.36	0.01	0.01	0.04	3.94
OC07	4.41	20.11	0.02	0.97	3.01	0.39	0.32	0.03	0.01	0.02	3.22
OC08	4.93	17.31	0.02	1.90	3.82	3.31	0.37	0.04	0.01	0.03	2.96
OC09	5.64	17.55	0.02	0.66	3.56	5.01	0.36	0.00	0.01	0.03	3.58
OC20	3.48	31.36	0.05	0.85	1.60	0.44	0.23	0.03	0.02	0.03	1.32
OC25	5.19	22.28	0.12	4.66	2.95	0.22	0.31	0.02	0.01	0.02	6.16
NHH1	5.62	21.42	0.02	0.81	3.92	0.46	0.36	0.01	0.01	0.02	2.74

Table 3. XRF analysis of major elements reported in wt%.

Parts per million (ppm) of Trace Elements															
Sample	Co	Ni	Cu	Zn	Ga	As	Pb	Th	Rb	U	Sr	Y	Zr	Nb	Mo
KC06	28.02	72.09	20.83	49.15	20.03	19.64	17.99	14.47	180.65	12.88	32.12	23.50	171.70	12.07	35.08
KC08	32.71	82.81	30.83	62.18	25.83	42.22	24.55	15.80	192.89	17.33	35.16	17.61	145.90	12.45	56.14
KC10	31.61	74.75	20.83	58.26	22.17	19.32	18.74	15.98	206.41	6.63	71.24	22.29	159.11	11.99	4.41
OC02	5.79	15.57	19.01	16.93	3.22	0.81	7.00	4.44	58.21	-1.20	125.30	50.22	143.79	10.60	11.10
OC03	7.17	176.99	59.13	167.57	6.97	22.99	14.83	7.61	55.50	62.20	81.41	14.48	91.84	12.27	229.29
OC04	21.19	82.99	56.44	108.00	13.93	41.50	20.18	7.96	88.06	17.57	72.24	28.25	128.44	11.36	42.75
OC05	6.45	136.36	57.61	253.56	9.15	8.49	11.10	9.92	98.57	47.81	47.62	27.10	142.15	13.02	170.61
OC06	26.58	86.77	29.04	64.84	19.01	45.35	24.28	13.14	160.08	17.51	44.70	25.57	149.81	10.64	85.19
OC07	18.22	126.45	47.52	158.60	15.18	21.47	17.05	13.08	147.00	33.57	38.22	19.77	120.64	11.96	122.49
OC08	19.35	155.14	78.64	182.91	20.64	50.13	24.12	12.69	123.96	51.70	81.87	16.64	156.94	12.43	113.92
OC09	19.64	53.06	13.82	52.99	15.53	5.34	12.30	14.10	183.04	3.59	42.20	27.38	173.08	10.25	9.27
OC20	9.69	41.30	11.64	33.35	10.62	38.33	20.15	8.37	108.13	8.31	202.62	25.24	95.22	9.43	23.62
OC25	12.85	124.56	52.06	118.17	15.47	10.04	14.13	12.44	150.19	13.17	155.27	24.91	100.31	9.20	25.85
NHH1	13.73	100.33	43.12	120.24	17.84	12.09	15.06	16.16	191.71	30.24	11.30	15.13	150.40	12.98	55.52

Table 4. XRF analysis of trace elements reported in ppm.

Precision of major element analyses on standards using HXRF												
	MgKa1	AlKa1	SiKa1	P Ka1	S Ka1	K Ka1	CaKa1	TiKa1	V Ka1	CrKa1	MnKa1	FeKa1
RTC-W-220	-0.6489	4.0849	24.5693	0.0130	2.3332	2.5851	0.0700	0.2775	0.1024	0.0125	0.0137	2.5471
RTC-W-220	-0.6756	4.1633	24.6712	0.0097	2.3115	2.6003	0.0862	0.2953	0.1081	0.0124	0.0146	2.5236
RTC-W-220	-0.7404	3.9550	23.8266	0.0116	2.2752	2.5563	0.1210	0.2896	0.1086	0.0124	0.0148	2.4884
RTC-W-220	0.7206	4.7211	29.2491	0.0799	2.5022	2.3405	0.1084	0.2588	0.0924	0.0103	0.0235	2.7042
RTC-W-220	0.3069	4.2834	26.8483	0.0614	2.3250	2.2579	0.1079	0.2615	0.0898	0.0110	0.0234	2.7913
RTC-W-220	0.3906	4.3774	27.4861	0.0587	2.3994	2.2935	0.0988	0.2708	0.0908	0.0107	0.0236	2.6562
RTC-W-220	0.5940	4.6472	28.1528	0.0806	2.4390	2.2998	0.2364	0.2555	0.0902	0.0101	0.0239	2.7032
Average	-0.0075	4.3189	26.4005	0.0450	2.3693	2.4190	0.1184	0.2727	0.0975	0.0113	0.0197	2.6306
Standard Deviation	0.6512	0.2845	2.0629	0.0325	0.0805	0.1535	0.0546	0.0155	0.0086	0.0011	0.0049	0.1124
Reported Values	0.6700	4.9600	32.6000	0.0700	3.3400	2.0700	0.1300	0.2300	0.0928	0.0110	0.0150	2.9300
Bruker Duplex 2205	1.8800	1.0775	1.5906	0.1557	1.4820	0.0383	0.5628	0.1441	0.1597	-18.6148	-2.7851	20.2449
Bruker Duplex 2205	3.4148	1.3054	1.7313	0.1310	1.6115	0.1204	0.1979	0.1245	0.1394	-0.2824	13.9393	22.7571
Bruker Duplex 2205	2.9991	1.3363	1.8853	0.1209	1.6078	0.0331	0.1873	0.1286	0.1390	-0.3495	14.2211	22.8379
Bruker Duplex 2205	2.9204	1.2607	1.8739	0.1092	1.5875	0.0563	0.1788	0.1281	0.1339	-0.2268	13.7160	22.6704
Bruker Duplex 2205	3.6905	1.5194	2.1874	0.1213	1.5488	0.1078	0.2523	0.1259	0.1371	-0.2057	13.6288	22.3963
Average	2.9810	1.2999	1.8537	0.1276	1.5675	0.0712	0.2758	0.1303	0.1418	-3.9359	10.5440	22.1813
Standard Deviation	0.6906	0.1585	0.2219	0.0175	0.0539	0.0404	0.1630	0.0079	0.0102	8.2060	7.4547	1.0952

Table 5. Results of XRF standards for major elements including average and standard deviation values.

Precision of trace element analyses on standards using HXRF																
	BaLa1	CoKa1	NiKa1	CuKa1	ZnKa1	GaKa1	AsKa1	PbLa1	ThLa1	RbKa1	U La1	SrKa1	YKa1	ZrKa1	NbKa1	MoKa1
RTC-W-220	0.1745	0.0014	0.0145	0.0126	0.0848	0.0018	0.0021	0.0018	0.0011	0.0134	0.0017	0.0056	0.0032	0.0116	0.0012	0.0073
RTC-W-220	0.2503	0.0016	0.0149	0.0132	0.0870	0.0018	0.0022	0.0018	0.0011	0.0133	0.0023	0.0061	0.0031	0.0115	0.0012	0.0080
RTC-W-220	0.1604	0.0016	0.0144	0.0133	0.0809	0.0018	0.0028	0.0020	0.0012	0.0135	0.0022	0.0063	0.0032	0.0114	0.0013	0.0078
Average	0.1951	0.0015	0.0146	0.0130	0.0843	0.0018	0.0024	0.0018	0.0011	0.0134	0.0021	0.0060	0.0032	0.0115	0.0012	0.0077
Standard Deviation	0.0484	0.0001	0.0002	0.0004	0.0031	0.0000	0.0004	0.0001	0.0000	0.0001	0.0003	0.0004	0.0000	0.0001	0.0001	0.0004
Reported Values	0.2090	N/A	0.0130	0.0083	0.0823	N/A	N/A	N/A	0.0008	0.0122	0.0018	0.0076	0.0035	0.0080	0.0001	0.0079
Bruker Duplex 2205	-0.1867	1.1119	-26.8760	3.6042	0.0037	0.0076	-0.0004	0.0032	0.0002	-0.0026	-0.0191	-0.0575	-0.0007	0.0094	-0.0002	-0.7696
Bruker Duplex 2205	-0.0984	1.0926	-26.3253	3.8435	0.0051	0.0081	-0.0015	0.0030	0.0002	-0.0021	-0.0213	-0.0593	-0.0003	0.0098	0.0001	-0.8835
Bruker Duplex 2205	-0.2670	1.1220	-27.0333	3.8519	0.0058	0.0073	0.0011	0.0037	0.0002	-0.0021	-0.0201	-0.0578	-0.0004	0.0089	0.0001	-0.8005
Bruker Duplex 2205	0.0294	1.1137	-26.8094	3.8043	0.0050	0.0078	-0.0009	0.0030	0.0001	-0.0024	-0.0218	-0.0601	0.0003	0.0100	0.0000	-0.9424
Average	-0.1307	1.1100	-26.7610	3.7760	0.0049	0.0077	-0.0004	0.0032	0.0002	-0.0023	-0.0206	-0.0587	-0.0003	0.0095	0.0000	-0.8490
Standard Deviation	0.1270	0.0124	0.3053	0.1164	0.0009	0.0004	0.0011	0.0003	0.0000	0.0003	0.0012	0.0012	0.0004	0.0005	0.0002	0.0787

Table 6. Results of XRF standards on trace elements including average and standard deviation values.

3.5 – Geochemical, thermal maturity, and crystallinity data

A significant amount of the geochemical data for the samples used in this study, and the locations and sample depth, were previously reported by Lambert (1993). Samples with incomplete geochemical data were sent to StratoChem Services, LLC for analyses. Weaver’s ratio, a measure of degree of illite crystallinity, was determined using XRD data from the glycolated clay slides and was calculated by dividing the diffractogram’s peak height at 10.0Å by the peak height at 10.5Å. K/Rb ratios were calculated using simple division from the XRF elemental data. The data are shown in Table 7. Tmax data for sample NHH1 are not available.

Sample	TOC (wt. %)	Mean Vit. Refl. In Oil (%)	Weaver's Ratio	Tmax (°C)	Depth (ft)	K/Rb
KC06	2.20	0.54*	2.89	440.00	3612.20	203.05
KC08	4.30	0.55*	2.27	441.00	2170.00	235.15
KC10	0.50	0*	3.72	439.00	3353.90	201.05
OC02	1.20	0*	1.30	442.00	4030.50	162.60
OC03	5.30	0.54	1.29	446.00	8619.50	260.42
OC04	7.00	0.55*	1.25	445.00	5627.30	223.80
OC05	6.80	0*	1.32	447.00	8507.50	263.13
OC06	4.40	0.57*	1.55	445.00	6084.50	243.89
OC07	5.20	0.52	1.72	446.00	6199.50	204.67
OC08	4.10	1.50	1.66	486.00	14267.50	308.10
OC09	0.40	0*	1.34	363.00	14332.50	194.72
OC20	0.43*	0.47	1.30	430.00	6150.00	147.83
OC25	7.9*	0.71	1.54	445.00	8407.00	196.41
NHH1	5*	1.27*	1.72	N/A	0.00	204.33

Table 7. Geochemical and calculated data for all 14 samples. * = Denotes data obtained from StratoChem Services. All other TOC, Tmax, and vitrinite reflectance values provided by Lambert (1993).

3.6 – Calculated Mineralogy

To determine which minerals were present in the samples the whole-rock XRD data were used. Spectra from the XRD bulk powder tests were analyzed, and the resulting 2θ and d-spacing of the peaks were measured and used to determine which minerals the peaks represented. With the knowledge of what minerals were present in the samples, the weight percentage of each mineral was calculated with the XRF data, assuming ideal mineral formulas.

The data were first converted from elemental weight percentage to a molar proportion by dividing the elemental weight percentage by the molar mass of the corresponding element. The molar proportions for all of the elements were summed, then the molar proportion of each element was divided by the summed molar proportions to get an elemental proportion. This was necessary because the elemental proportion is needed to calculate a mineral weight percentage based on the whole rock chemistry. The elements V, Cr, and Mn were ignored because they were only present in trace amounts. Mg was not used because of the unreliability of Mg determination by XRF. This produced uncertainties when allocating Mg, as certain minerals that complex with Mg, such as Si and Al, could not be fully accounted for in minerals such as chlorite.

The elemental proportions of each element were assigned to the simplest minerals first, then working toward the more complex minerals, keeping track of the remaining element proportions of each element not used in the previous minerals. Calculations for this study began with the allotment of K to illite, in accordance with an approximate ideal chemical formula for illite ($\text{KAl}_2(\text{Si,Al})_4\text{O}_{10}$). Next, all of S was allotted to pyrite (FeS_2) along with Fe in the amount of 1/2 of the allotted sulfur. Apatite ($\text{Ca}_5(\text{PO}_4)_3(\text{OH,F,Cl})$) was then set equal to 1/3rd of P's elemental proportion. Iron oxides were then accounted for by allotting the entirety of Ti, along with an equal amount of Fe assuming an ideal ilmenite (FeTiO_3). At this point the remaining Fe

and Ca were calculated. The remaining Ca was allotted to dolomite ((Ca,Mg)CO₃), while the remaining Fe was allotted to chlorite ((Mg,Fe)₄Al₄Si₂O₁₀(OH)₈). The remaining Si was calculated by subtracting the starting elemental proportions from the amount of Si allotted to illite and chlorite. The rest of the Si was allotted to quartz (SiO₂). The molar proportions of each mineral was multiplied by that mineral's molar weight, resulting in mineral weights, which were summed together, then each mineral's weight was divided by the summed total to get a mineralogical weight percentage. This process was repeated for all 14 samples to determine mineral weight percentages, as seen in Table 8.

Wt% of Calculated Mineralogy							
Sample	illite	pyrite	FeTi oxides	apatite	chlorite	dolomite	qtz/chert/fossil tests
KC06	45.78	2.30	1.69	0.20	8.24	9.44	32.35
KC08	63.34	2.74	1.97	0.21	8.84	5.30	17.59
KC10	57.78	1.98	1.98	0.26	11.42	6.19	20.40
OC02	11.47	0.82	0.59	0.42	1.28	37.53	47.88
OC03	18.17	2.00	0.83	0.31	0.59	1.91	76.20
OC04	28.58	5.48	1.29	0.16	3.08	15.94	45.47
OC05	36.60	1.22	1.25	0.32	2.31	1.43	56.87
OC06	48.91	3.36	1.44	0.18	7.64	20.79	17.67
OC07	43.98	2.66	1.51	0.17	7.82	2.61	41.26
OC08	48.06	4.51	1.48	0.11	2.95	18.92	23.97
OC09	40.63	1.42	1.31	0.13	7.90	25.97	22.65
OC20	19.67	1.96	0.91	0.35	1.03	2.41	73.67
OC25	37.41	11.11	1.24	0.85	5.91	1.23	42.23
NHH #1	51.98	2.02	1.52	0.15	5.73	2.76	35.84

Table 8. Calculated mineralogy using XRF data reported in wt%.

Chapter 4 - Discussion

4.1 – Sample Problems

There were a number of complications that became evident after all of the data were compiled. Cardott and Lambert (1985) report vitrinite reflectance values in the Woodford range from less than 0.5% to over 5%. As seen in Table 7, vitrinite reflectance values for samples in this study reach a maximum of 1.5%. Hence, the samples used for this study do not include the wide range of thermal maturity reported within the Woodford. It was also a surprise that four of the samples provided by Lambert did not report vitrinite data. These were sent to StratoChem for analyses, but were reported by them as having 0% vitrinite. Meagan Wall of StratoChem services offered her explanation for this: “Generally speaking, Vitrinite Reflectance is not as durable a measurement of maturity as most geochem tomes would lead you to believe. Vitrinite, itself, is firmly associated with Type III kerogen, and is not present before the appearance of woody plants in the Devonian. It is a great deal more likely that the samples simply did not have input of woody material upon deposition.” This results in a major limitation of this study, that the samples do not represent the wide distribution in thermal maturity originally presumed, which limits the range to measure the controls on illitization.

Due to these problems with vitrinite values, Tmax was used as a marker for thermal maturity in this study. Sample OC09, however, appears to have an abnormally low Tmax value, given its great sample depth. Hossam Ali, senior geochemist at StratoChem Services explains “We note that this sample is organically lean (TOC=0.4%) and with very low pyrolysis yield

(HI¹=10 mg HC/g² TOC, S2³= 0.04 mg HC/g Rock). With such low S2 value the S2 peak most probably is flat and therefore the Rock-Eval instrument failed to detect an apex for the S2 peak and reported a false value. With such bad S2 peaks, the Rock-Eval instrument identify the first irregularity part in the S2 peak and reported the Tmax for it. Note that such Tmax values should be ignored and excluded from any interpretation.”

Total Organic Carbon (TOC) values in the Woodford range from 0% up to over 25% (Kirkland et. al., 1992). From Table 7 it can be seen that TOC values in this study range from 0.4%-7.9%, with 11 of the 14 samples having a TOC lower than 5.5%. Similar to the vitrinite reflectance values, the range of TOC values for these samples are not a good representation of the wide range of TOC observed throughout the Woodford.

¹ Hydrogen Index-Measurement of the hydrogen richness of a source rock.

² Milligrams of hydrocarbons per gram of rock.

³ Volume of hydrocarbons formed during the pyrolysis of the sample. Used to estimate the remaining hydrocarbon generating potential of the sample.

4.2 – Illitization

One of the goals of this research was to compare the relationship of vitrinite reflectance to illitization in the Woodford to the relationship reported in Ouachita shales (Guthrie et. al., 1986). This isn't entirely achievable because of insufficient vitrinite reflectance data for all

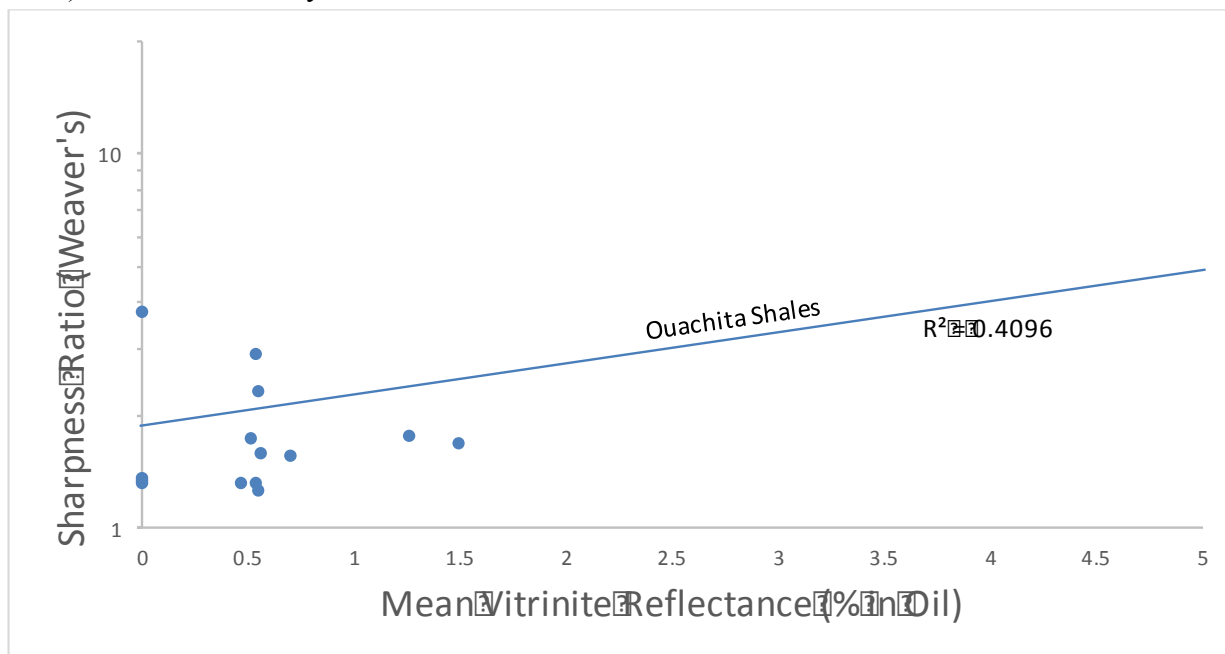


Figure 15. Mean vitrinite reflectance vs Weaver's sharpness ratio. Solid line represents the trendline for the Ouachita shales found in Guthrie et. al. (1986) (Figure 4).

samples, and the limited range of vitrinite reflectance values observed for the samples studied. Figure 15 compares the results of this study to the linear relationship of Guthrie et. al. (1986). No linear correlation exists among the Woodford samples from this study. However, variation around the mean for a given vitrinite value, such as 0.5%, does appear similar to that found by Guthrie et. al. (1986) (Figure 4). It would be informative to include samples with vitrinite reflectance values above 1.5% to determine behavior in this region.

4.3 – Clay Mineralogy

Coincident with the relatively high degree of illite crystallinity, the samples contain very little to no mixed-layer clays, even at low vitrinite reflectance levels. Smectite is easily identified by comparing diffraction patterns of air-dried and ethylene glycol-solvated preparations. The glycolated sample gives a very strong 001 reflection at $5.2^\circ 2\theta$ (16.9\AA) which shifts to $6^\circ 2\theta$ (15\AA) in the air-dried sample (Moore and Reynolds, 1997). Looking at example KC06, no such peaks are observable in either the glycolated or air-dried samples (Figures 16 and 17). Smectite, however, can also exist interlayered with illite as a mixed-layer clay. To determine whether smectite is present as a mixed-layer with illite, several things can be looked for. According to Moore and Reynolds (1997), if diffraction patterns are significantly altered by ethylene glycol solvation, one may expect mixed-layer illite/smectite present. A second indicator is to examine the region between 16 to $17^\circ 2\theta$ in the ethylene glycol solvated diffraction patterns. If a reflection is noted there, then an illite/smectite mixed-layer is likely present. Looking again at sample KC06 in Figures 16 and 17, neither of these criteria are seen, nor are they in any of the other spectra (Appendix A). It can be confirmed that there is very little (if any) smectite present in any of these samples. They would have to have been deposited as

mostly detrital illite, which is unlikely (Whittington, 2009), or any smectite and mixed-layer clays have already been completely converted to illite.

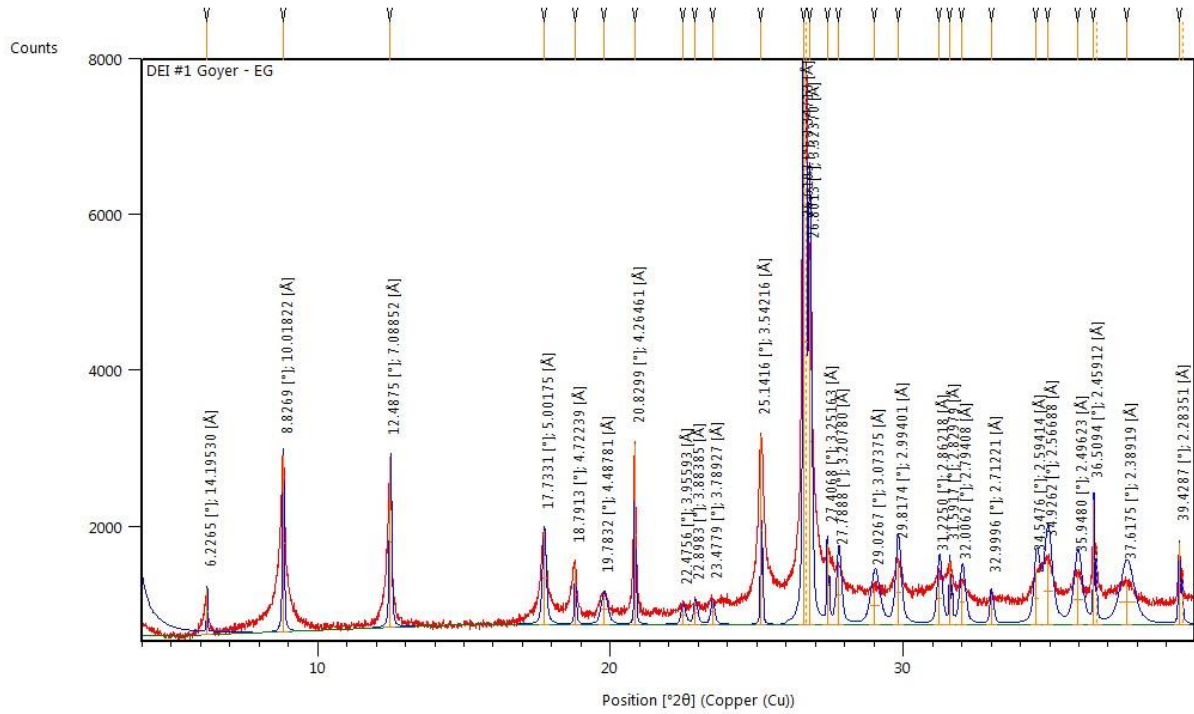


Figure 16. Diffraction pattern for glycolated sample KC06.

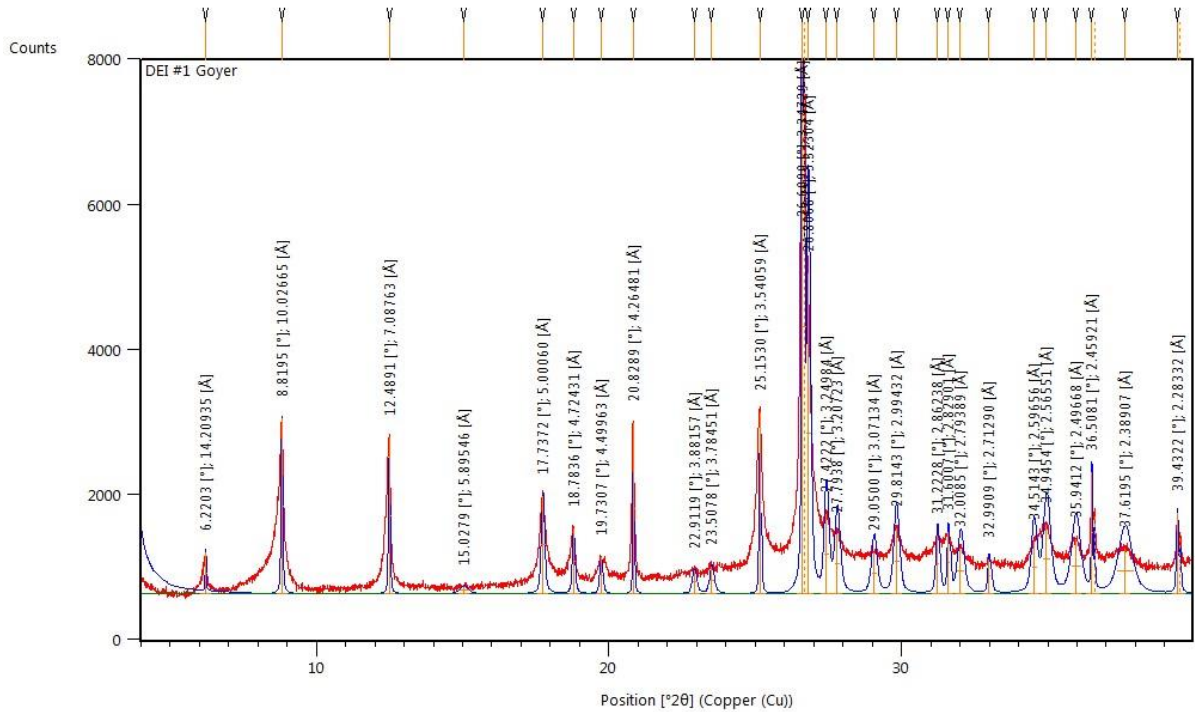


Figure 17. Diffraction pattern for air-dried sample KC06.

For some samples, such as OC02, diffraction peaks for clays appeared suppressed (Figure 18). Initially it was thought this may be due to inadequate sample preparation. For several samples with these suppressed peaks, completely new clay slides were created from the same starting material and analyzed with the XRD. Results for the new slides showed very similar diffraction patterns to the original, with virtually no change from before. After calculations of the mineralogy, it became evident that most of the samples with suppressed clay peaks were in fact low in clay abundance and very high in other minerals such as dolomite or quartz (Table 8). This suggests that these particular samples may, in fact, represent a different rock type than the organic and clay-rich facies targeted as unconventional reservoirs. The quartz-rich samples represent a siltstone facies, and the dolomite-rich samples likely a calcareous (dolomitic) shale, rather than a true Woodford shale. This, unfortunately, limits their usefulness for this study.

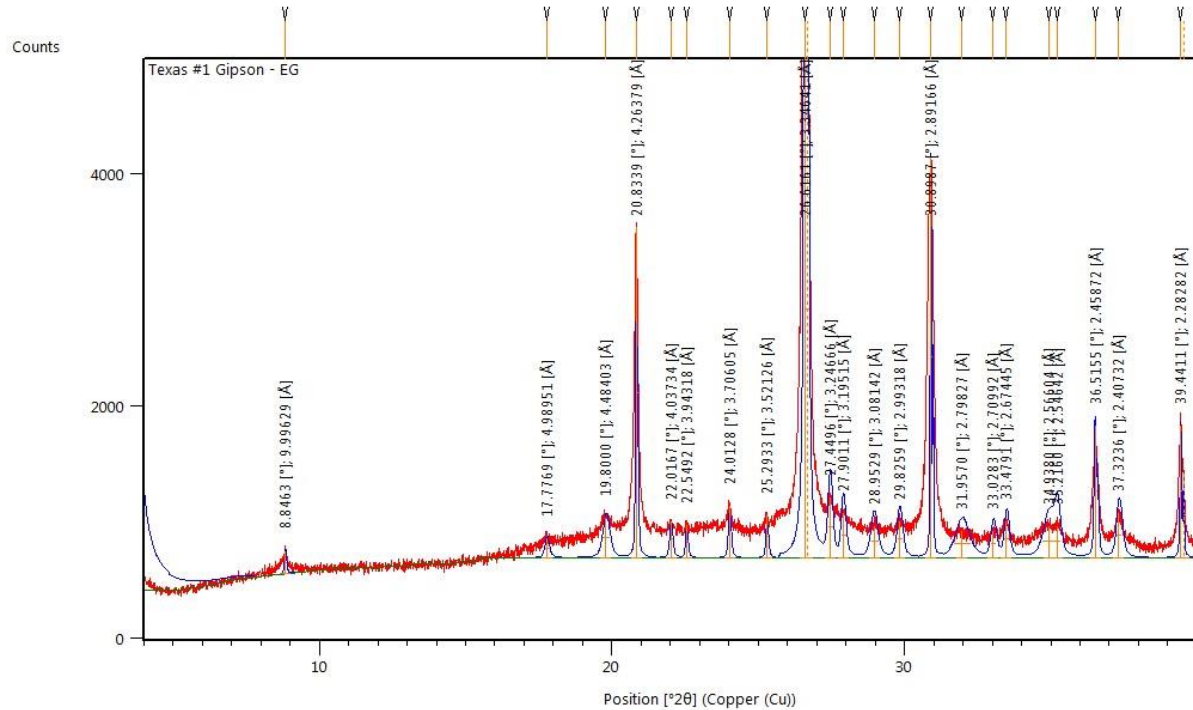


Figure 18. Diffraction pattern for glycolated sample OC02. Note the suppressed clay peaks and high dolomite and quartz peaks.

4.4 – Thermal Maturity

As previously stated, Tmax was used as an indicator of thermal maturity in this study, with the exception of samples OC09 and NHH1, which were excluded as previously discussed. Figure 19 displays the relationship between Tmax and depth. The figure shows a trend line indicating thermal maturity increasing with depth. If we compare this to the values shown in Table 9, it is seen that most of the samples lie in the oil hydrocarbon generation zone from type II kerogen (435-455°C). This relationship attests to the control of burial depth on thermal maturity, which was expected. Figure 19 also illustrates the lack of samples at higher thermal maturity among the sample suite for this study.

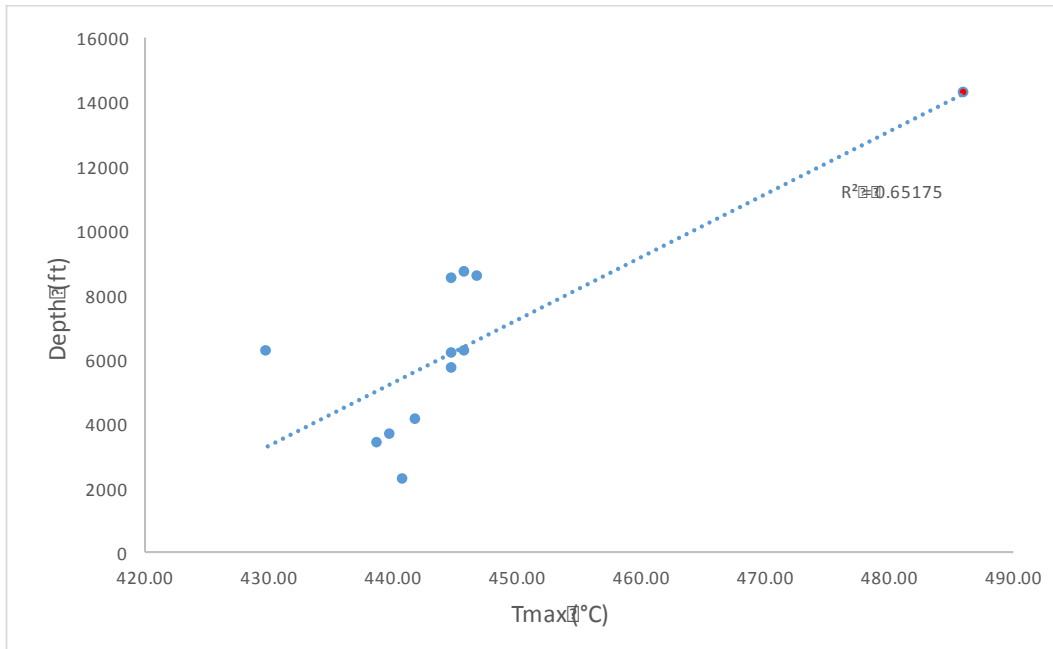


Figure 19. Tmax vs depth.

Hydrocarbon Generation Zone	Rock-Eval Pyrolysis T _{max} , °C
Immature	< 435
Oil (from type II kerogen)	435–455
Oil (from type III kerogen)	435–465
Gas (from type II kerogen)	> 455
Gas (from type III kerogen)	> 465

Table 9. Hydrocarbon generation zones for Tmax values (Beaumont and Foster, 2000).

4.5 – K/Rb Ratio

Chaudhuri et al. (2007) found the K/Rb ratio can be a strong geochemical tracer for the source of potassium in a system. They concluded that K/Rb ratios are much higher in organic matter than in common potassium-bearing silicate minerals, such as feldspar and mica. With this information, Totten et al. (2013) investigated the transformation of smectite to illite in the Woodford shale, with the focus of determining the source of potassium and other minerals

needed to drive this process. The study found abnormally low K/Rb ratios in the organic fraction of the samples, and very high K/Rb ratios in the clays. They concluded that K was selectively removed from organic matter during the burial diagenetic transformation. Moreover, they proposed that clay mineral diagenesis is actually driven by organic matter transformations, as organic maturation releases the essential components needed for the process. In addition, Larriestra et. al. (2015) examined the K/Rb ratio related to paleoenvironmental conditions and its consequence for the identification of source rock intervals and reservoir quality evaluation. In their study, it was reported that K/Rb ratios were significantly higher in oil-bearing sandstones than clean sandstones.

Based upon these previous studies, K/Rb ratios were investigated in relation to thermal maturity for this study. A relationship between K/Rb and T_{max} can be seen in Figure 20, with increasing K/Rb ratio with increasing T_{max} . This correlation suggests that maturation of source rocks progresses with increased organic influence. When removing samples believed to be poor representations (suppressed clay XRD peaks, dolomite-rich) of actual Woodford shale (OC02, OC03, OC04, OC05), an even stronger correlation is observed (Figure 21). Caution should be used, however, as the regression is strongly influenced by only one value with high T_{max} .

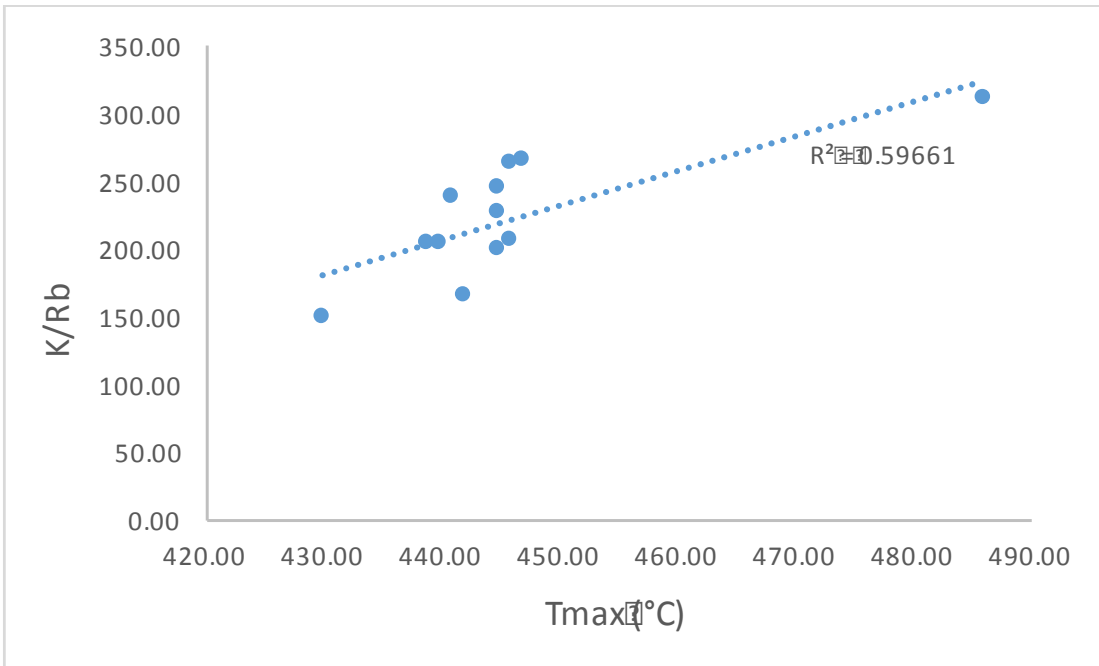


Figure 20. Tmax vs K/Rb ratios.

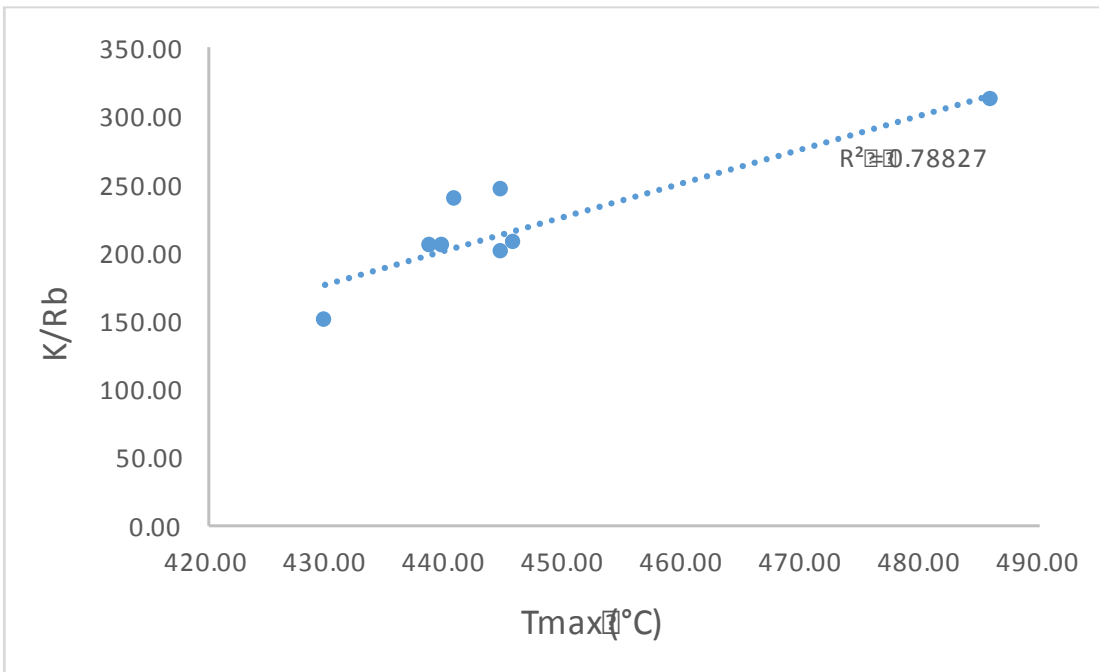


Figure 21. Tmax vs K/Rb without samples OC02, OC03, OC04, OC05.

4.6 – Mineralogical Variation with Tmax

A correlation coefficient measures the degree to which two variables move in relation to each other. The coefficient ranges from -1 to +1, where a high positive correlation means the two variables tend to increase together while a high negative correlation shows they move apart at the same time. If the coefficient is close to zero, the correlation is a random, weak, nonlinear correlation. A correlation coefficient between calculated mineral % and Tmax can be seen in Table 10. As observed, coefficients range from -0.3 to +0.25. This demonstrates a weak correlation coefficient, and it can be said there is not any statistical correlation between any of the mineral percentages and Tmax. Furthermore, Figure 22 displays calculated illite percent versus Tmax. Very little correlation exists, as confirmed by its 0.20 correlation coefficient (Table 10). This reinforces the conclusion that all of the samples in this study are already illite, with little to no smectite present.

Correlation Coefficients (Mineral % vs Tmax)	
Pyrite	0.21
Apatite	-0.26
Chlorite	-0.17
Illite	0.20
FeTi Oxides	0.09
Dolomite	0.25
Qtz/Chert/Fossil Tests	-0.30

Table 10. Correlation coefficients of calculated mineral percentages vs Tmax.

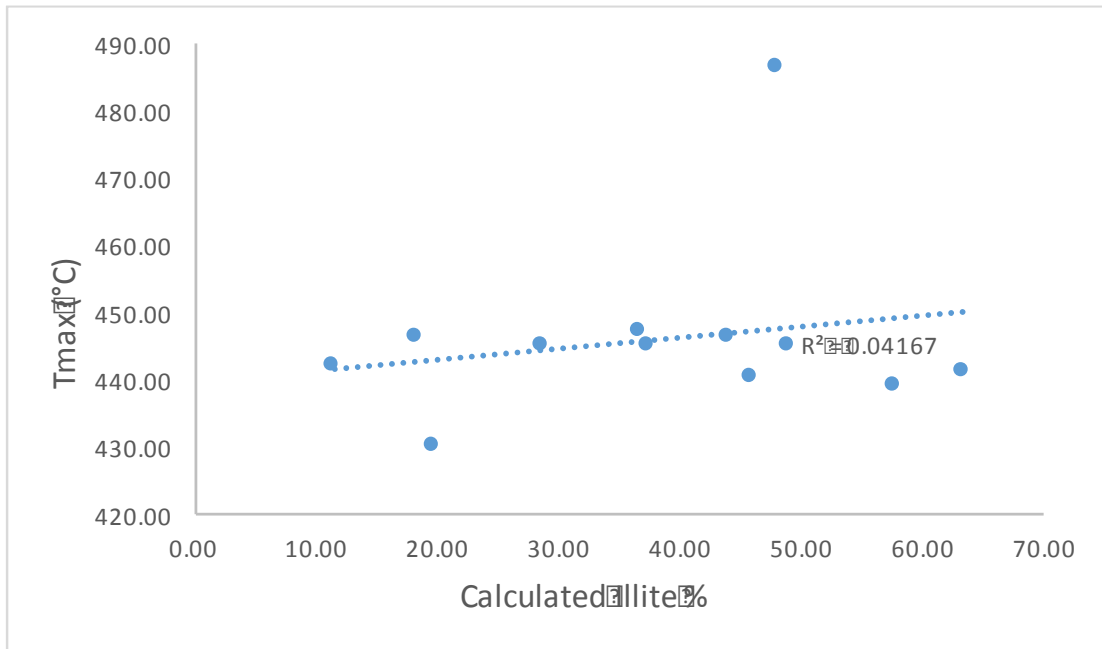


Figure 22. Calculated illite percentages vs Tmax.

4.7 – Total Organic Carbon (TOC)

To go along with data discussed above, a correlation between TOC and K/Rb ratios can be observed. Looking at Figure 23, generally speaking, a higher amount of TOC correlates with

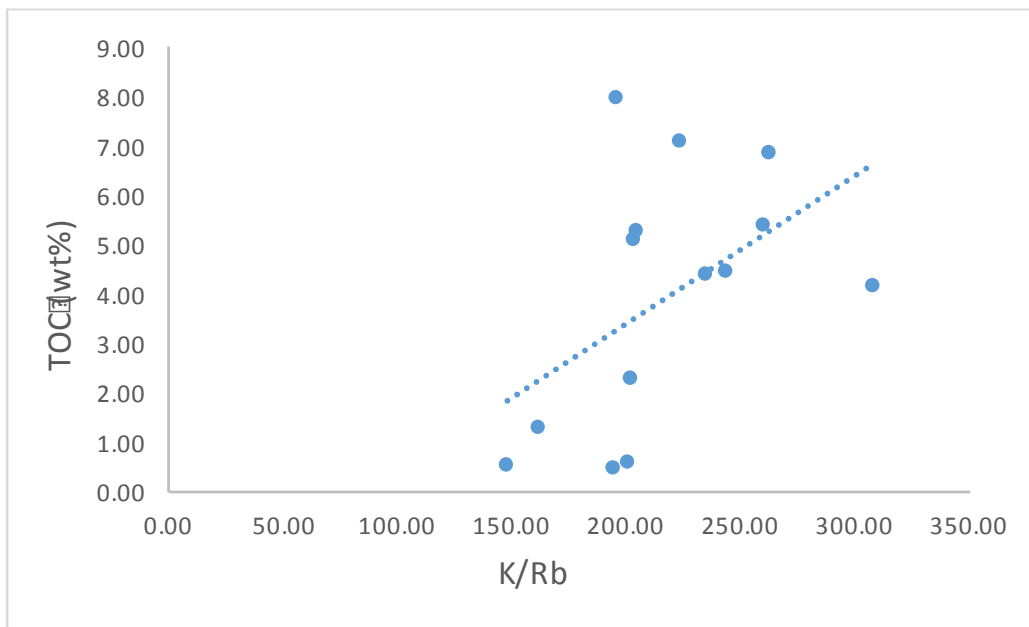


Figure 23. K/Rb vs. TOC (wt%).

a higher K/Rb ratio. This is consistent with the conclusion made by Chaudhuri et al. (2007) that K/Rb ratios are much higher in organic matter than common potassium-bearing silicate minerals.

A correlation between TOC and Tmax also exists. Figure 24 displays a trend of increasing Tmax with increasing TOC, with the exception of one outlier (OC08). Sample OC08 was at a depth of 14,267.5 feet, much deeper than any of the other samples except OC09, which was previously excluded due to a Tmax value that appears to be too low. Due to this extreme depth relative to the other samples, it is expected to be overmature and out of the hydrocarbon generation window, which is validated by its high Tmax value. According to Pang et al. (2016), TOC values significantly decrease with the mass hydrocarbon expulsion once a source rock enters the overmature stage. Sample OC08 is consistent with this claim, and is excluded from this comparison. All of the other samples in Figure 24 lie within the immature to early mature thermal maturation stage (Table 9), and indicate increasing thermal maturation with increasing TOC values.

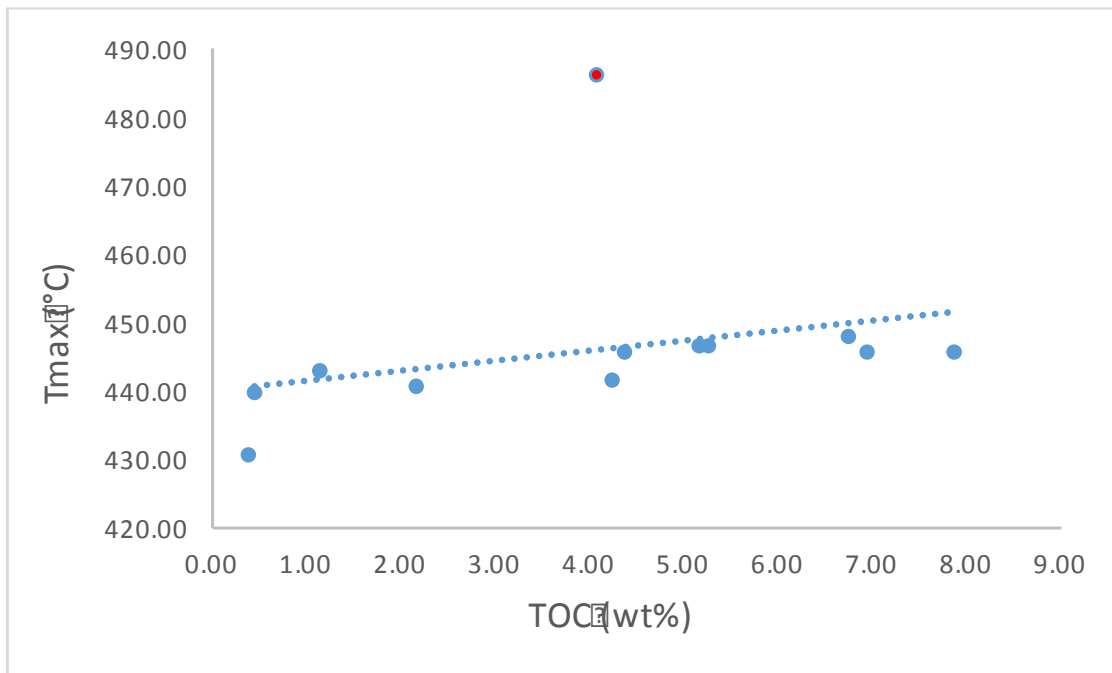


Figure 24. TOC vs Tmax.

A study conducted by Zhang et al. (2017) utilized a handheld XRF for examination of drill cuttings in horizontal wells in the Woodford shale. Upon analyses, an abnormally high Mo zone was identified, which was interpreted as evidence for a euxinic condition on deposition that aided the preservation of organic matter. Further analyses found that the same zone contained high TOC values, up to 10.9%. They concluded that high Mo concentrations in cuttings or core samples from vertical wells could be used as a proxy for high TOC, which is useful locating target zones for a horizontal well. Figure 25 displays the relationship between Mo and TOC for the samples in this study. The figure shows a general trend of increasing Mo with increasing TOC, further validating the conclusions by Zhang et al. (2017).

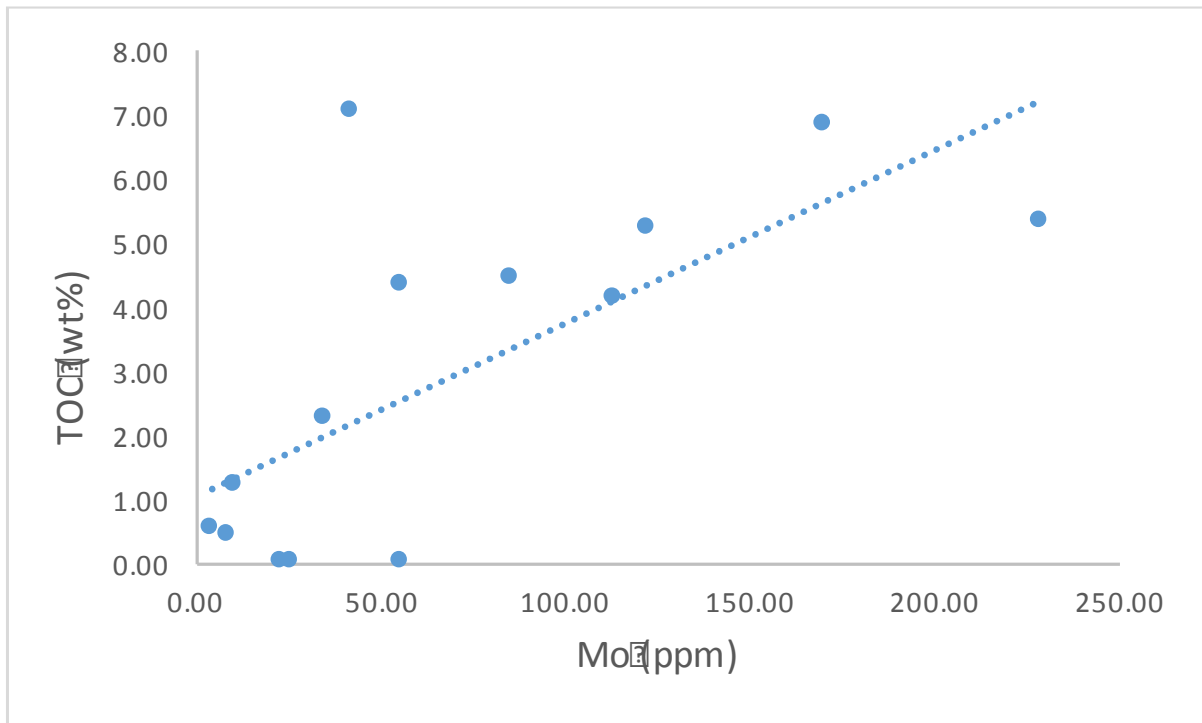


Figure 25. Mo (ppm) vs TOC (wt%).

Chapter 5 - Conclusion

This study provides insights into the investigation of the influence of organic matter on illitization in the Woodford shale. It was found from XRD analysis that the predominate clay mineral in all samples is illite, with no recognizable mixed-layer smectite present, even at low thermal maturities. This was supported by the high percentages of illite found in the calculated mineralogy from XRF data. This suggests illitization is occurring very early in the diagenetic process. Chaudhuri et al. (2007) and Totten et al. (2013) suggested that high amounts of K and other elements found within organic matter could be causing this accelerated illitization. This hypothesis is supported in this study by examining K/Rb ratios, where higher K/Rb ratios in the clays show a direct correlation with increased thermal maturity. The correlation between K/Rb and TOC further supports the control of organic matter on potassium in shales.

It was found that the mineralogical compositions of samples in this study were not affected by increasing thermal maturity, as very weak correlation between the two variables existed. Of particular interest was that illite was not controlled by Tmax, which provides more evidence for the theory that high amounts of organics are driving illitization rather than thermal maturity.

A correlation between Mo and TOC was also found in the samples in this study. Samples with higher TOC tended to have higher Mo contents, agreeing with similar results found by Zhang et al. (2017). This relationship could potentially be useful in quickly identifying organic-rich zones with the use of an XRF on drill cuttings and cores on-site.

A major limitation of this study arose from the choice of samples to include in the study. Future investigations should include very immature shales with smectite remaining, as well as

samples representing a wider range of TOC, ideally up to 25%. Ideally samples should encompass a wider range of Woodford shale compositions, rather than those with lower clay contents, as observed in several of the samples in this study.

References

- Amsden, T. W., (1975). Hunton Group (Late Ordovician, Silurian, and Early Devonian) in the Anadarko basin of Oklahoma: Oklahoma Geological Survey Bulletin 121, 214 p.
- Beaumont, Edward A., and Norman H. Foster. (2000). *AAPG Treatise of Petroleum Geology: Exploring for Oil and Gas Traps*. 1st ed. AAPG.
- Boles, J.R., and Franks, S.G., (1979). Clay diagenesis in Wilcox sandstones of southwest Texas: implications of smectite diagenesis on sandstone cementation: *Journal of Sedimentary Petrology*, v. 49, p. 55-70.
- Bradley, W.F. (1945). Molecular association between montmorillonite and some polyfunctional organic liquids. *Journal of the American Chemical Society*, 67, 975-981.
- Caldwell, Craig D. (2011). "Lithostratigraphy of the Woodford Shale, Anadarko Basin, West-Central Oklahoma." AAPG Search and Discovery Article #50518: p. 1-25.
- Cardott, B. J. and M. W. Lambert. (1985). Thermal maturation by vitrinite reflectance of Woodford Shale, Anadarko basin, Oklahoma, AAPG Bulletin, vol. 69, no. 11, p. 1982-1998.
- Chaudhuri, S., N. Clauer, and K. Semhi, (2007). Plant decay as a major control of river dissolved potassium: a first estimate, *Chemical Geology*, vol. 243, no. 1, p. 178-190.
- Eberl, D. D.; Velde, B. (1989). "Beyond the Kübler index" *Clay Minerals* 24 (4): 571–577.
- Faure, Gunter (1998). *Principles and applications of geochemistry : a comprehensive textbook for geology students* (2nd ed.). Upper Saddle River, N.J.: Prentice Hall.
- Feinstein, S., (1981). Subsidence and thermal history of Southern Oklahoma aulacogen Implications for petroleum exploration: *American Association of Petroleum Geologists Bulletin*, v. 65, p. 2531-2533.
- Garner, D.L., Turcotte, D.L., (1984). The thermal and mechanical evolution of the Anadarko basin: *Tectonophysics*, v. 107, p. 1–24.
- Guthrie, J. M., D. W. Houseknecht, and W. D. Johns. (1986). Relationships among vitrinite reflectance, illite crystallinity, and organic geochemistry in Carboniferous strata, Ouachita Mountains, Oklahoma and Arkansas, AAPG Bulletin, vol. 70, no. 1, p. 26-33.
- Harris, Dustin, (2017). A laboratory investigation into rock physics and fracture potential of the Woodford shale, Anadarko Basin, Oklahoma. Thesis. Kansas State University Graduate School. Manhattan. Kansas State University.

Higley, D.K., (2014). Thermal Maturation of Petroleum Source Rocks in the Anadarko Basin Province, Colorado, Kansas, Oklahoma, and Texas, chap. 3, *in* Higley, D.K., compiler, Petroleum systems and assessment of undiscovered oil and gas in the Anadarko Basin Province, Colorado, Kansas, Oklahoma, and Texas ---USGS Province 58: U.S. Geological Survey Digital Data Series DDS-69-EE, 53 p.

Polastro, R. M., (1985). Mineralogical and morphological evidence for the formation of illite at the expense of illite/smectite: *Clays and Clay Minerals*, v. 33, p. 265-275.

Hoffman, P., J. F. Dewey, and K. Burke., (1974). Aulacogens and their genetic relation to geosynclines, with a Proterozoic example from Great Slave lake, Canada, *in* Modern and ancient geosynclinal sedimentation: SEPM Special Publication 19, p. 38-55.

Hower, J., Eslinger, E.V., Hower, M.E., and Perry, E.A. (1976). Mechanism of burial metamorphism of argillaceous sediment: 1. Mineralogical and chemical evidence. *Geological Society of America Bulletin*, 87, 725–737.

Jiang, Shu. (2012). Clay Minerals from the Perspective of Oil and Gas Exploration, Clay Minerals in Nature - Their Characterization, Modification and Application, Dr. Marta Valaskova

Johnson, K. S., and Cardott, B.J., (1992). Geologic Framework and Hydrocarbon Source Rocks of Oklahoma. *Oklahoma Geological Survey Circular* ,93 (21), 37.

Kirkland, D.W., Denison, R.E., Summers, D.M., and Gormly, J.R., (1992). Geology and Organic Geochemistry of the Woodford Shale in the Criner Hills and Western Arbuckle Mountains, Oklahoma. *Oklahoma Geological Survey Circular v. 93*, 38-69.

Kowal, David Anazario. (2016). Comparison of Thermal Maturation Indicators Within Hydrocarbon Bearing Sedimentary Rock. Thesis. Kansas State University.

Lambert, M.W. (1993). Internal Stratigraphy and Organic Facies of the Devonian-Mississippian Chattanooga (Woodford) Shale in Oklahoma and Kansas, *in* B.J. Katz and L.M. Pratt, eds., Source rocks in a sequence stratigraphic framework: AAPG Studies in Geology 37, p. 163-176.

Larriestra, F., Covo, M. E., Cunio, R., Benso, A., Corbellieri, A., & Larriestra, C. N. (2015). The K/Rb Ratio and Its Geological and Petrophysical Implications: A Test Case of the San Jorge Gulf Basin, Argentina. *Search and Discovery Article #41644*, 1-14.

Moore, D. M. and R. C. Reynolds. (1989). X-ray Diffraction and the Identification and Analysis of Clay Minerals, Oxford university press Oxford. 332 pp.

Northcutt, R.A., and Campbell, J.A. (1995). Abstract: Geologic Provinces of Oklahoma, by R. A. Northcutt and J. A. Campbell; #90957. AAPG.

Pang, Xiongqi, Qianwen Li, Sumei Li, and Maowen Li. (2016). The recovery of TOC and its application in source rocks at high mature – over mature stage in deep petroliferous basin. International Conference and Exhibition, Barcelona, Spain, 3-6 April 2016: pp. 217-217.

Rowe, H., Hughes, N., and Robinson, K. (2012). The quantification and application of handheld energy-dispersive x-ray fluorescence (ED-XRF) in mudrock chemostratigraphy and geochemistry: *Chemical Geology*, v. 324-325, p. 122–131.

Semhi, K., (2013). Source of Potassium for the Illitization Process in Buried Argillaceous Rocks: A Case for Evidence from the Woodford Shale, North-Central Oklahoma. *GCAGS Transactions*, 2013, p 449-454.

Totten, M. W., M. A. Hanan, D. Mack, and J. Borges. (2002). Characteristics of mixed-layer smectite/illite density separation rates during burial diagenesis: *American Mineralogist*, v. 87, p. 1571-1579.

Totten, M. W., and H. Blatt. (1993). Alteration in the non-clay-mineral fraction of pelitic rocks across the diagenetic to low-grade metamorphic transition, Ouachita Mountains, Oklahoma and Arkansas: *Journal of Sedimentary Petrology*, v. 63, p. 899-908.

Totten, M.W., Ramirez-Caro, D., Chaudhuri, S., Clauer, N., Boutin, R., Riepl, G., Miesse, J. and

Totten, M. W., Sr., J. Borges, and I. M. Totten. (2007). The effect of provenance on clay mineral diagenesis in Gulf of Mexico shales: *Gulf Coast Association of Geological Societies Transactions*, v. 57, p. 699-716.

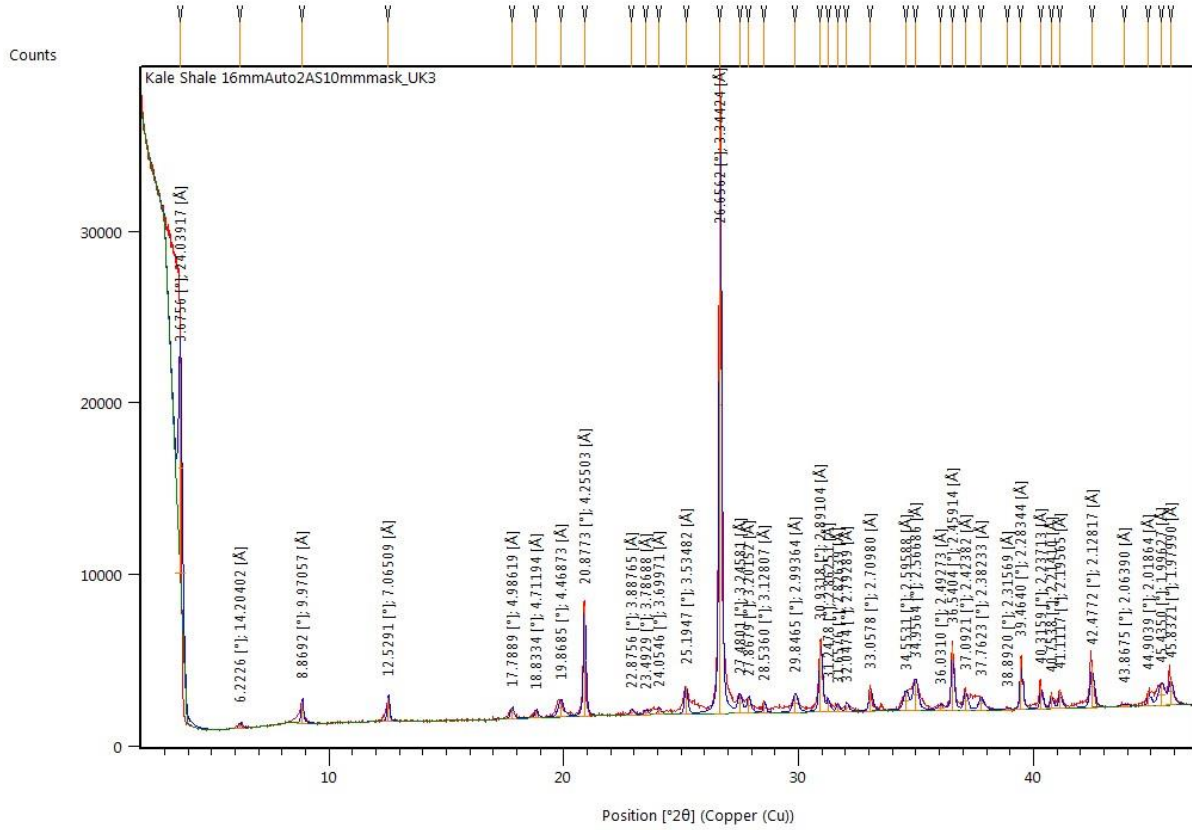
Weaver, C. E., (1960). Possible uses of clay minerals in search for oil, *AAPG Bulletin*, vol. 44, no. 9, p. 1505-1518.

Webster, R.E., (1980). Evolution of S. Oklahoma aulacogen: *Oil and Gas Journal*, v. 78, no. 7, p. 150-172.

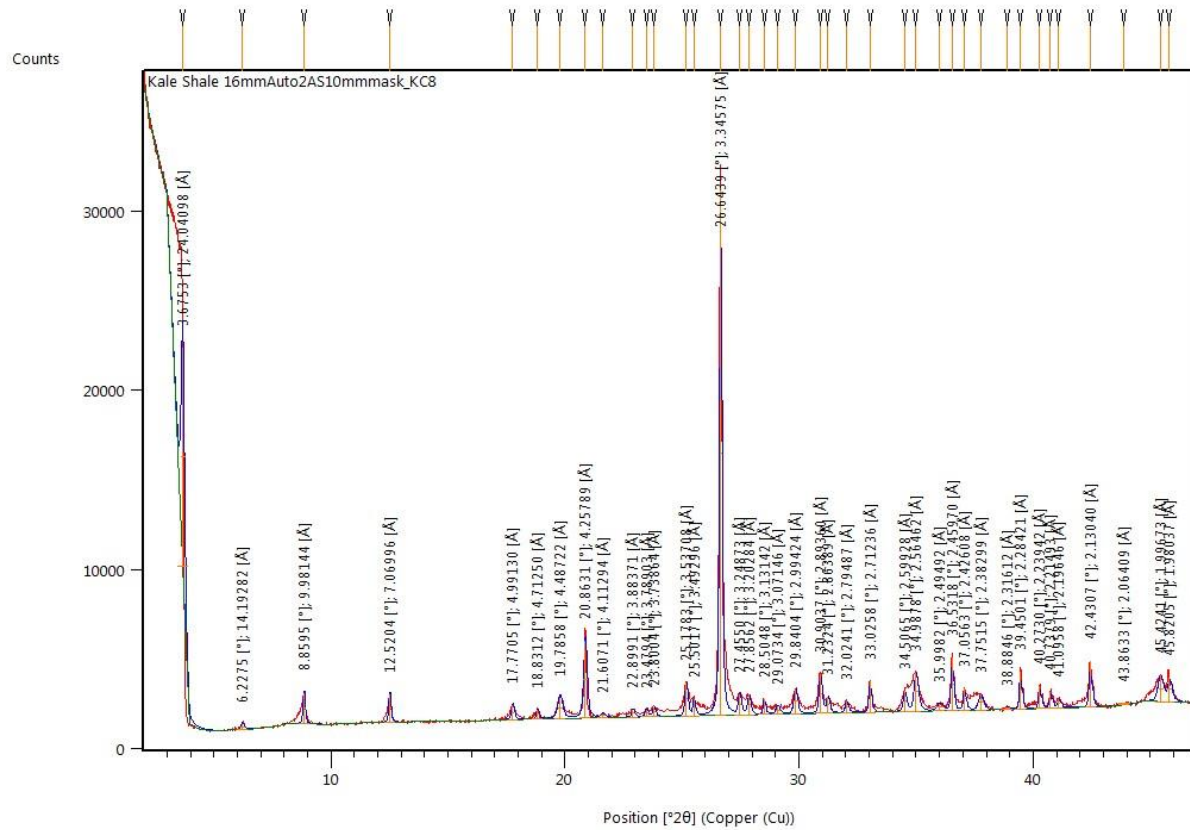
Whittington II, Richard Allen, (2009). "Clay Mineralogy and Illite Crystallinity in the Late Devonian to Early Mississippian Woodford Shale in the Arbuckle Mountains, Oklahoma, USA." Thesis, Georgia State University.

Zhang, Jing, Bryan Turner, and Roger Slatt. (2017). "XRF Chemostratigraphy for Characterizing Shale Reservoir along a Horizontal Well Track." *AAPG Search and Discovery Article #41993*

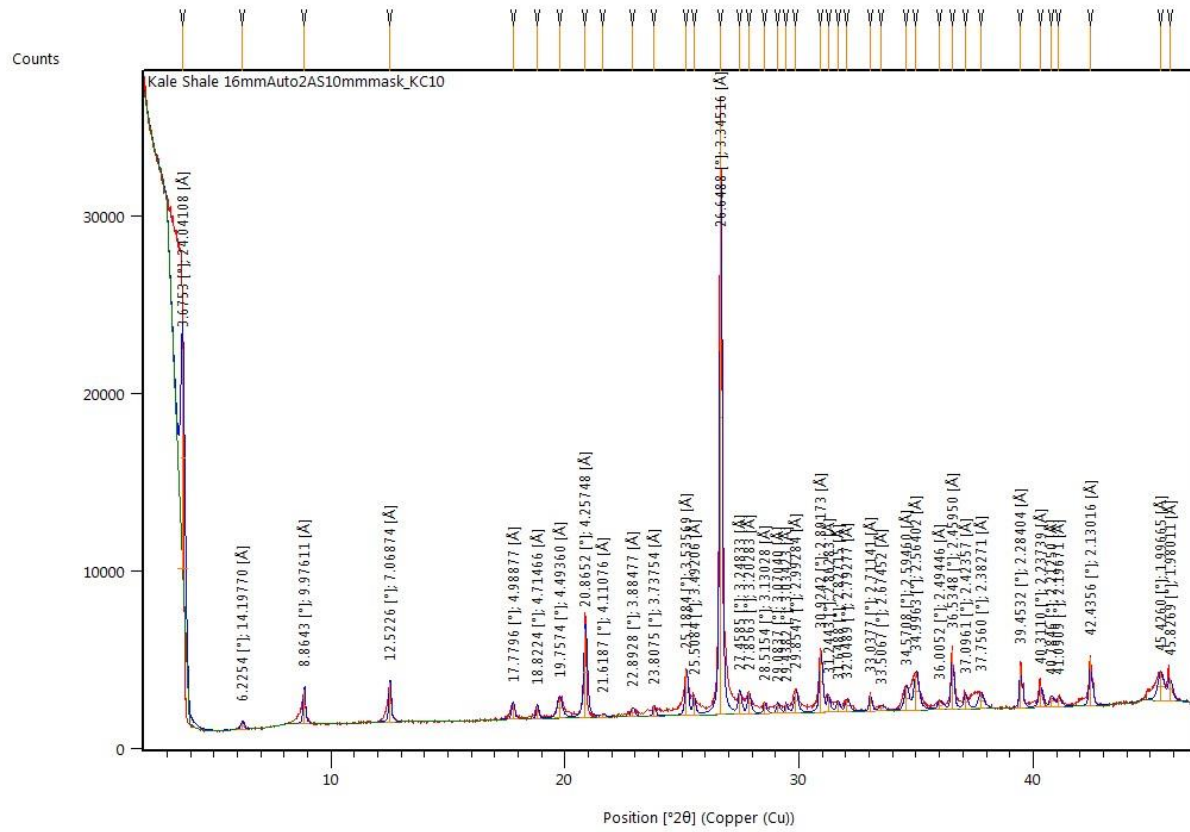
Appendix A -



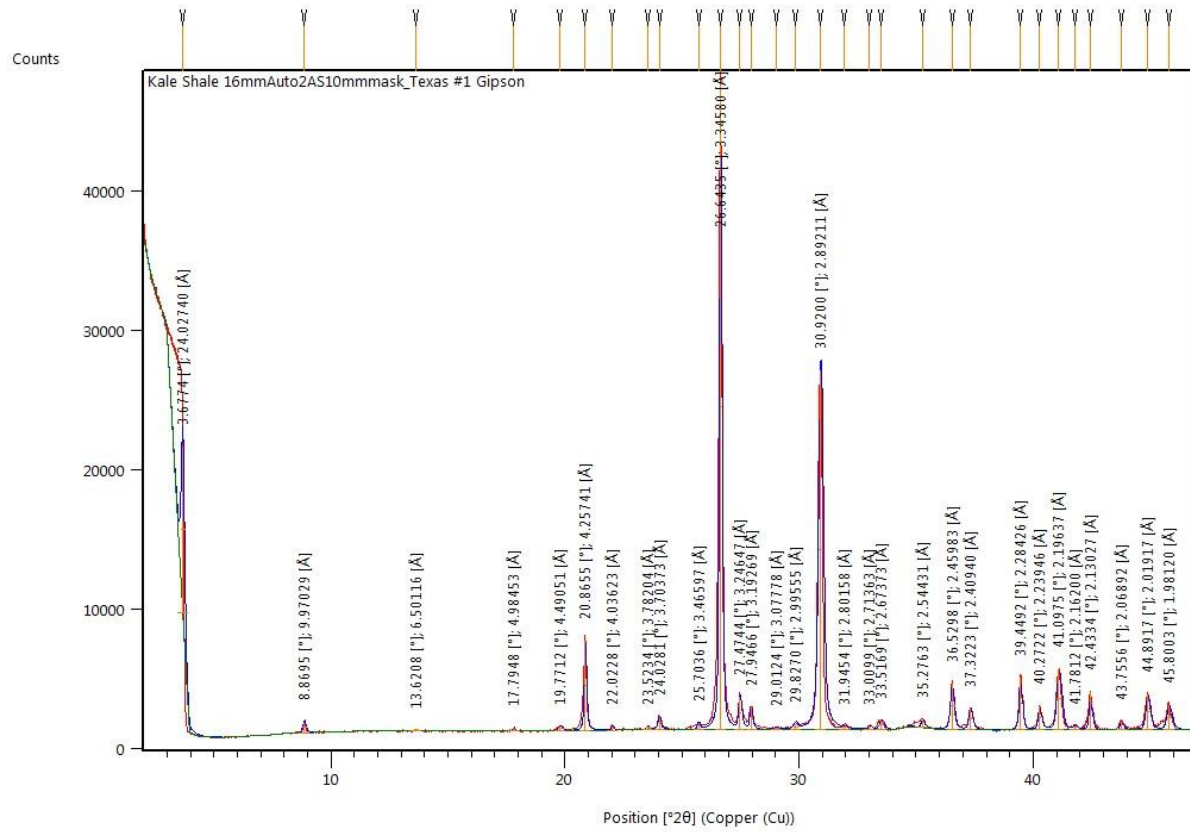
Appendix A.1 - 1 KC06 bulk powder XRD analysis.



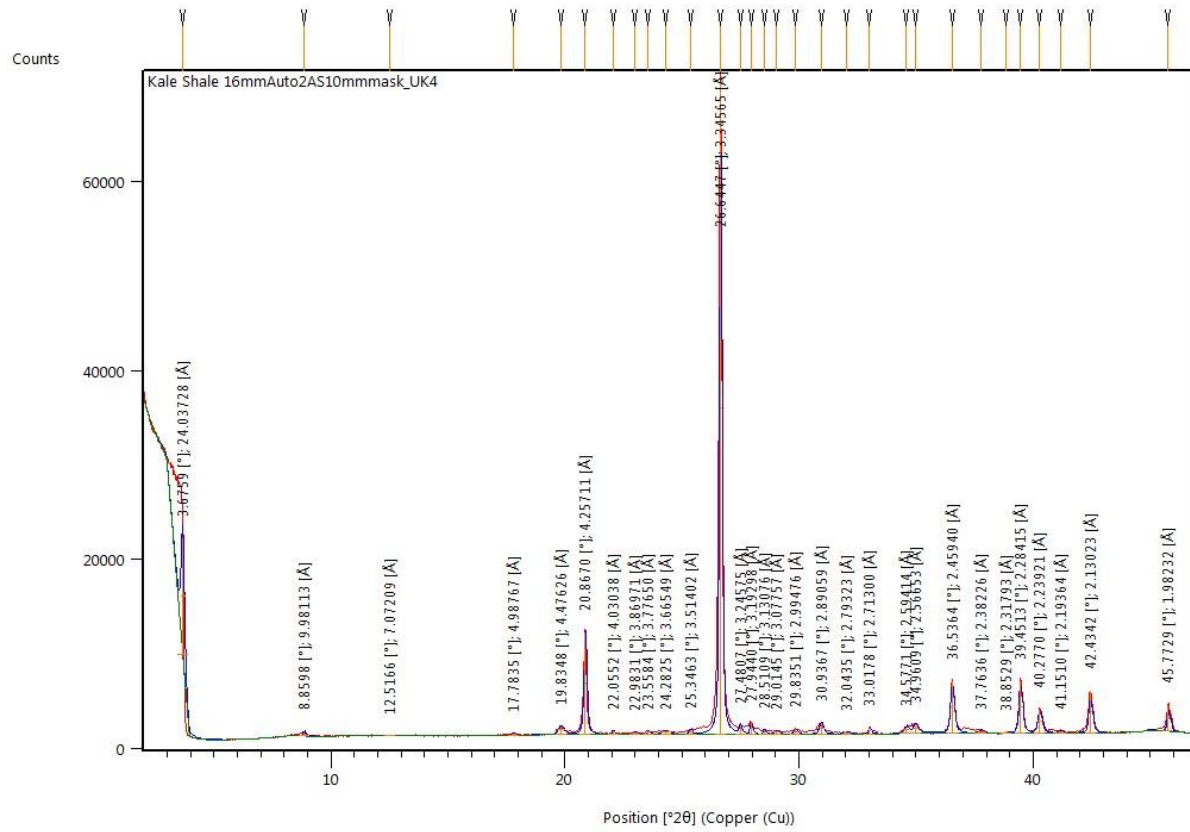
Appendix A.1 - 2 KC08 bulk powder XRD analysis.



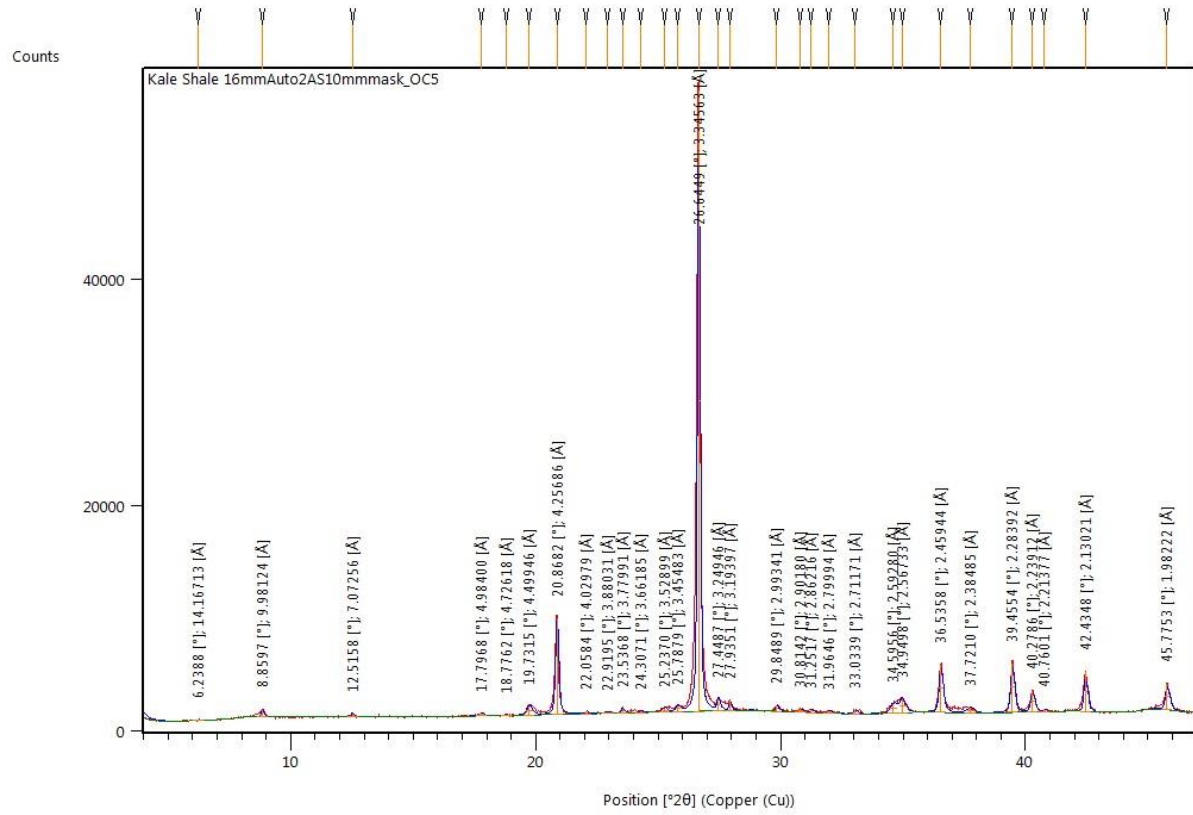
Appendix A.1 - 3 KC10 bulk powder XRD analysis.



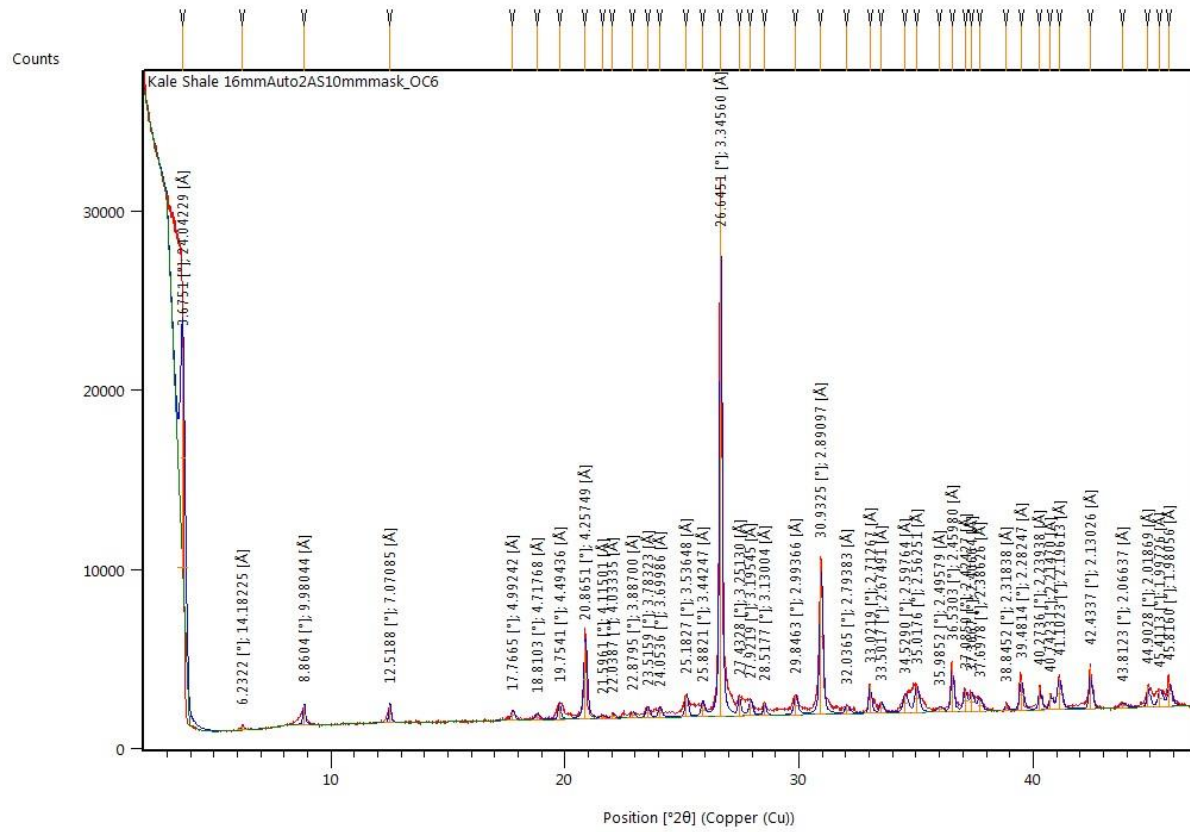
Appendix A.1 - 4 OC02 bulk powder XRD analysis.



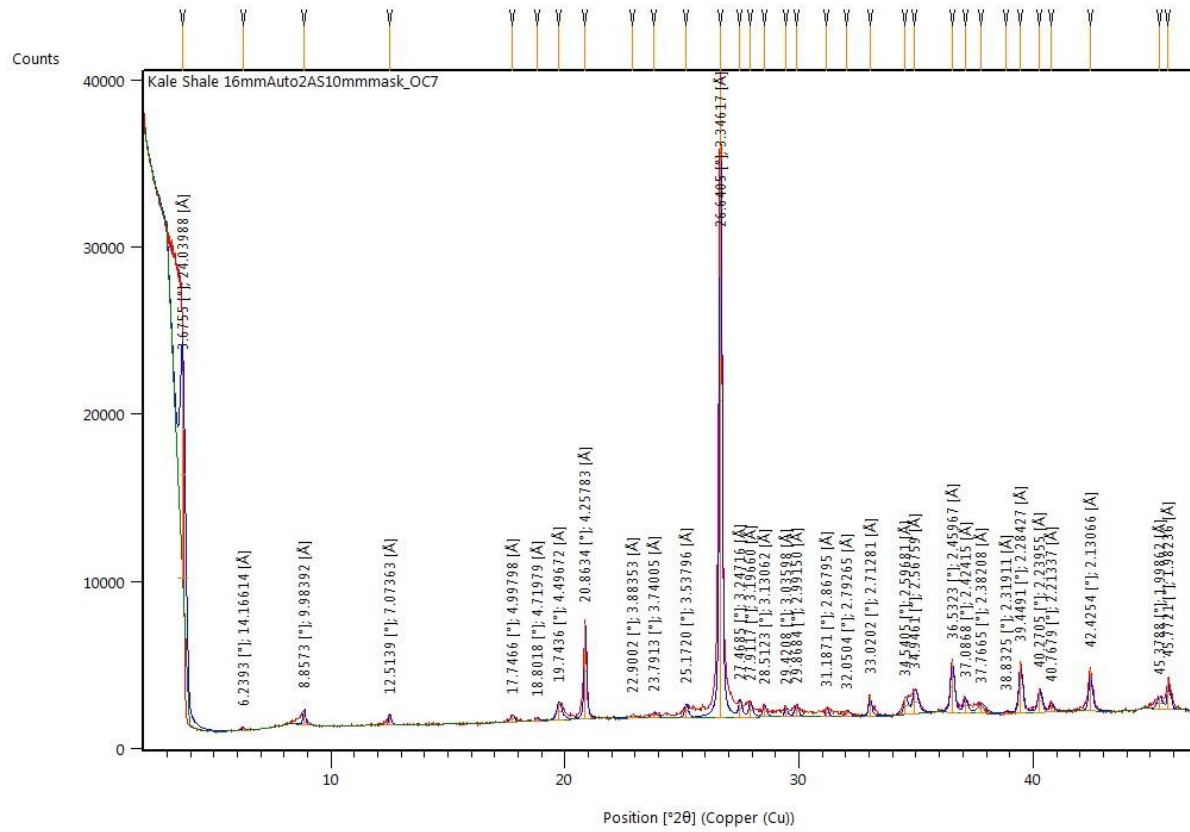
Appendix A.1 - 5 OC03 bulk powder XRD analysis.



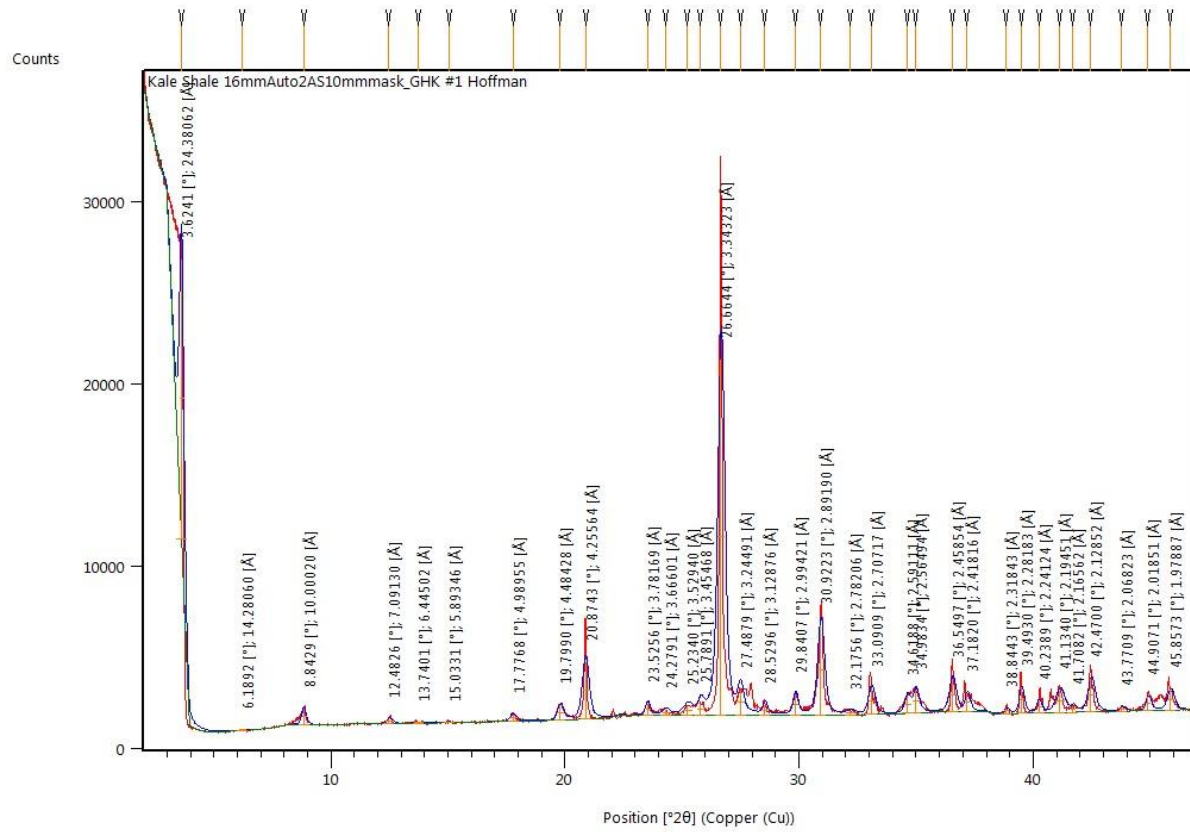
Appendix A.1 - 7 OC05 bulk powder XRD analysis.



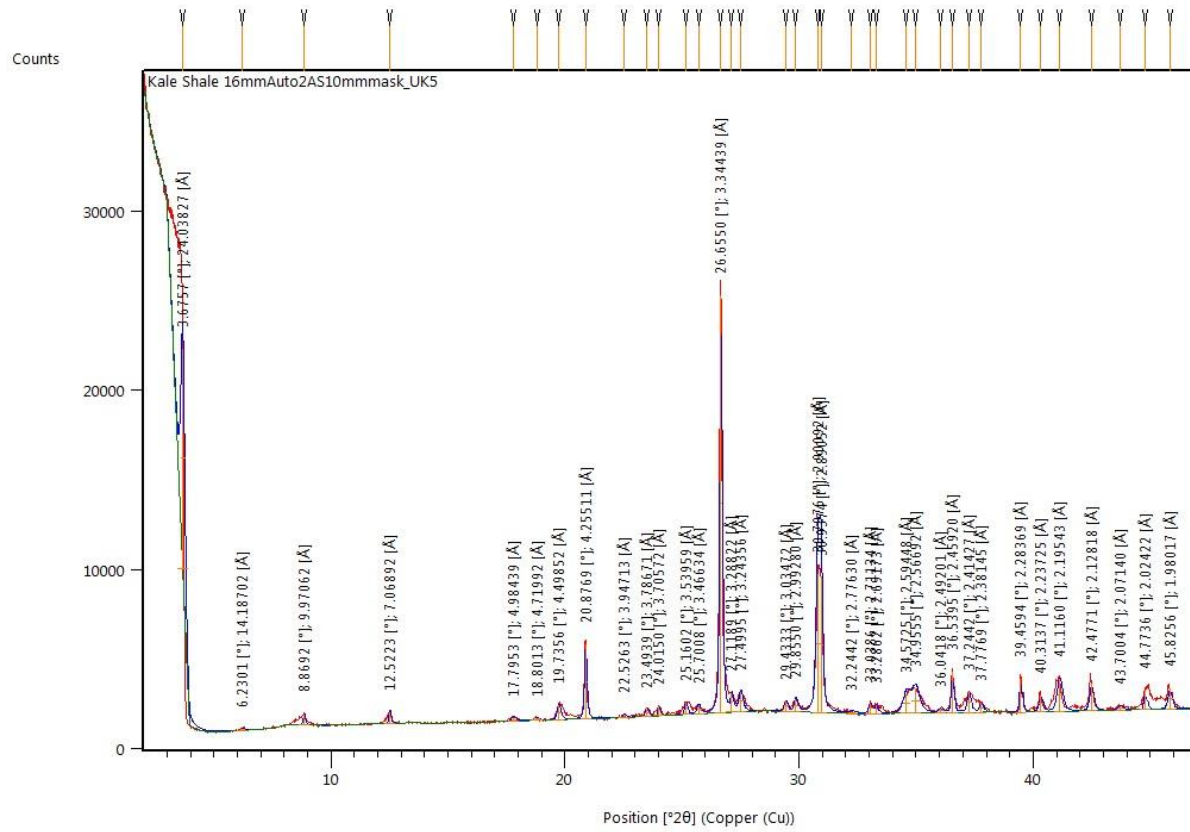
Appendix A.1 - 8 OC06 bulk powder XRD analysis.



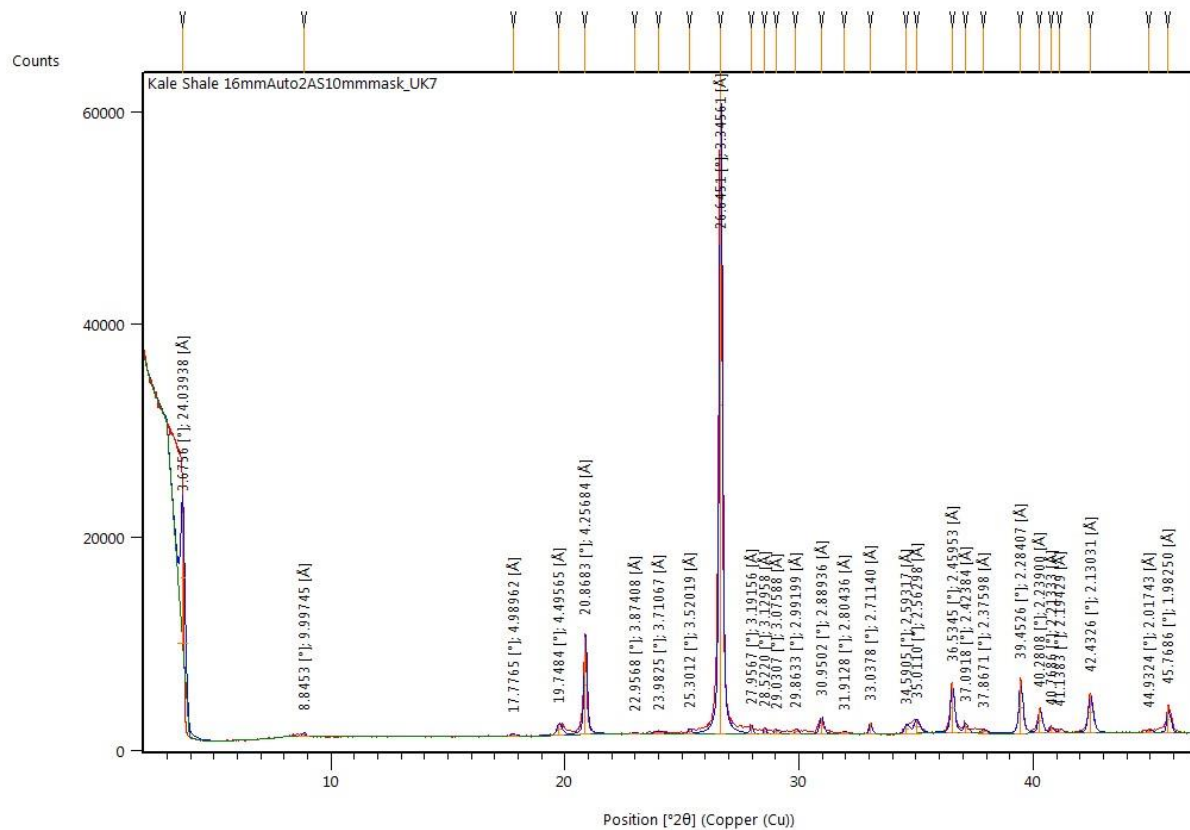
Appendix A.1 - 9 OC07 bulk powder XRD analysis.



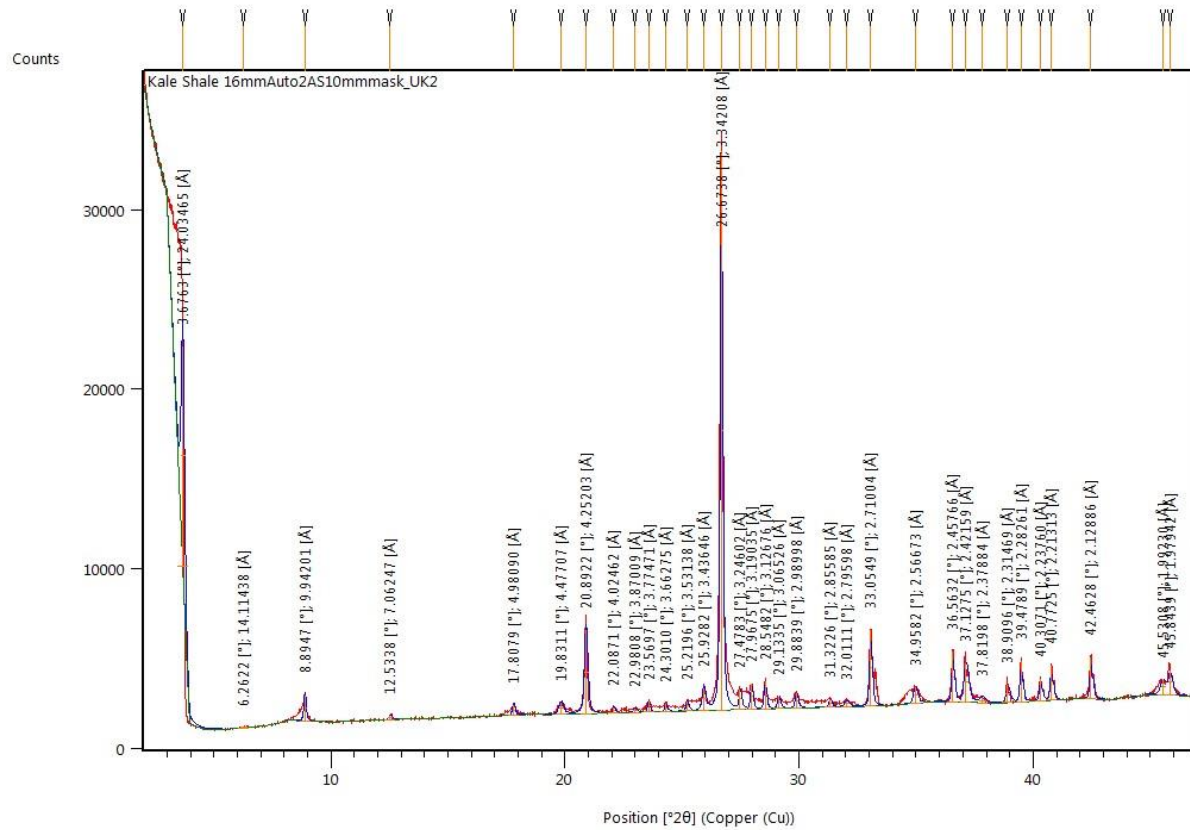
Appendix A.1 - 10 OC08 bulk powder XRD analysis.



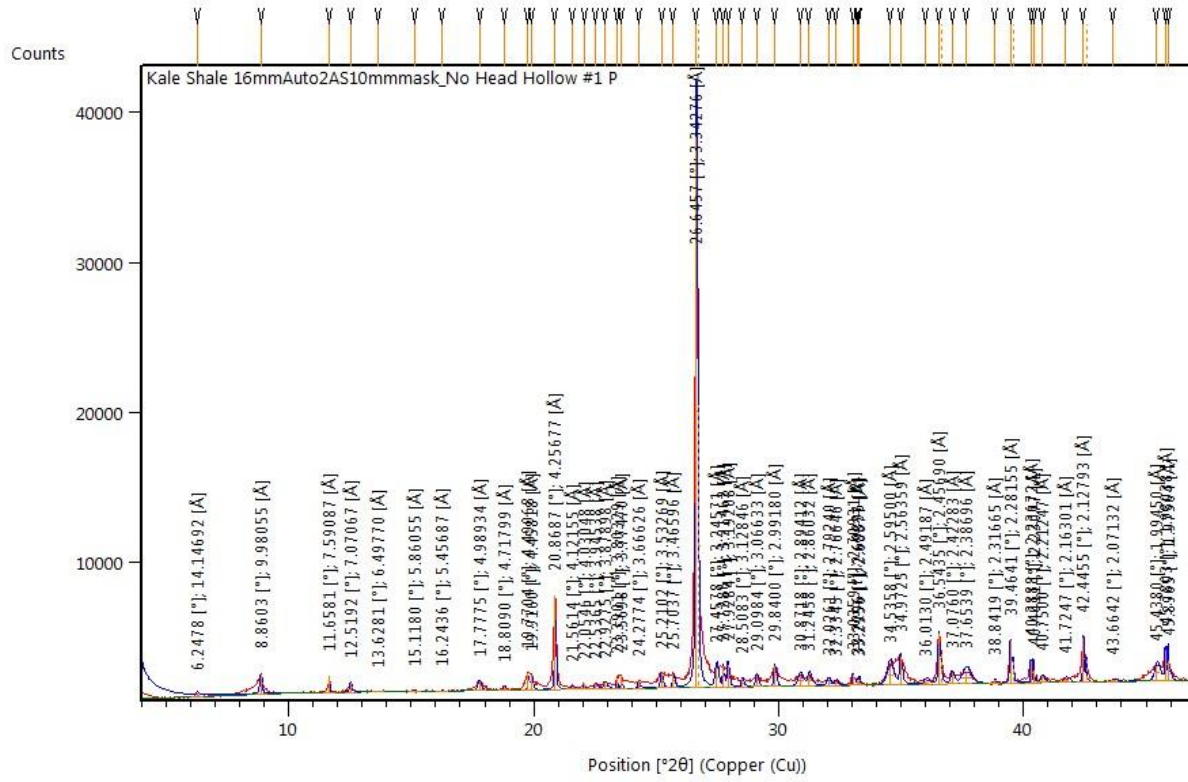
Appendix A.1 - 11 OC09 bulk powder XRD analysis.



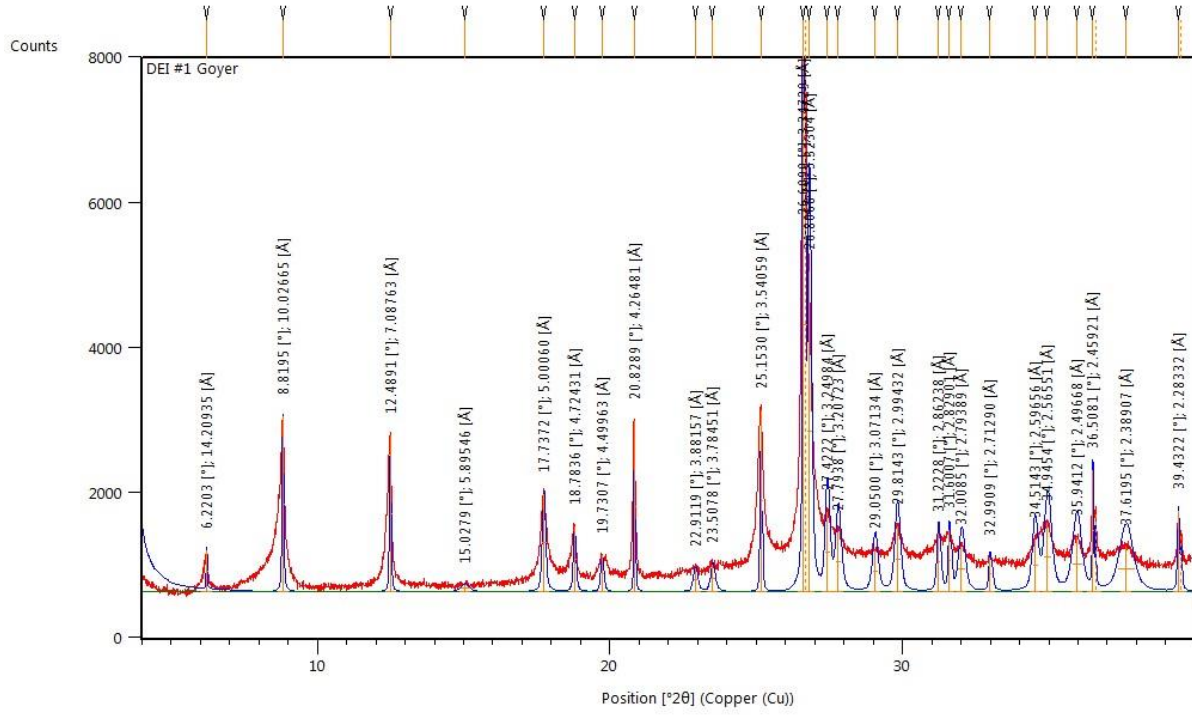
Appendix A.1 - 12 OC20 bulk powder XRD analysis.



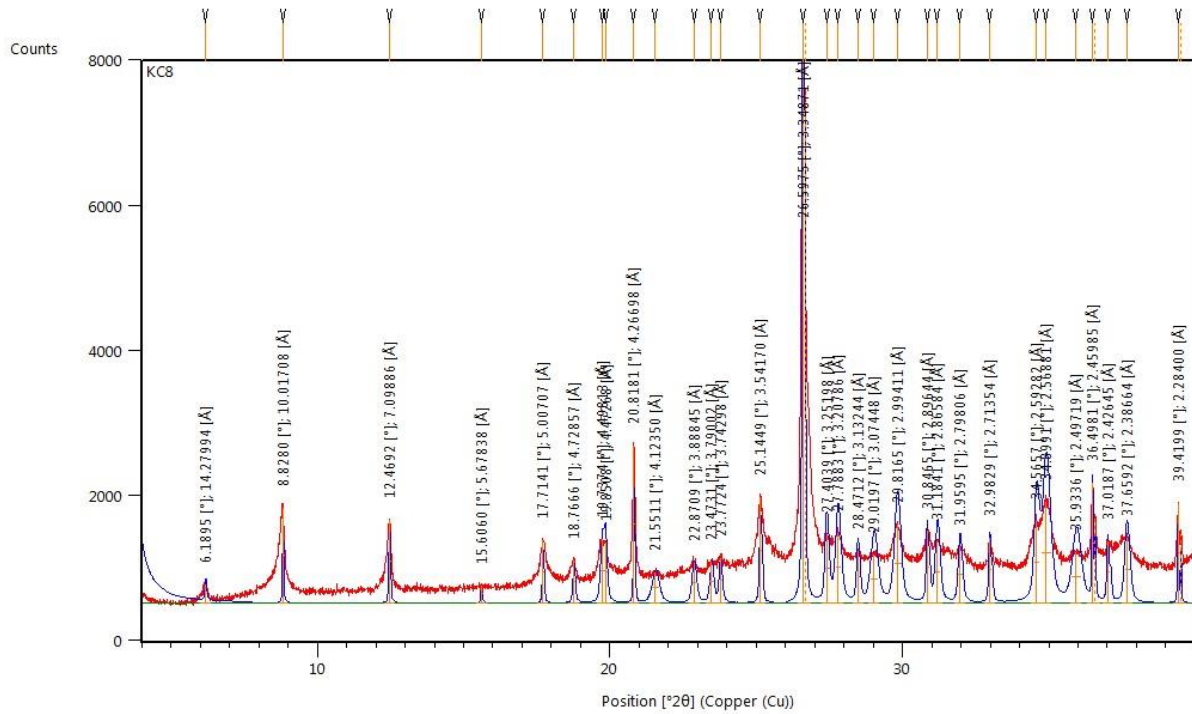
Appendix A.1 - 13 OC25 bulk powder XRD analysis.



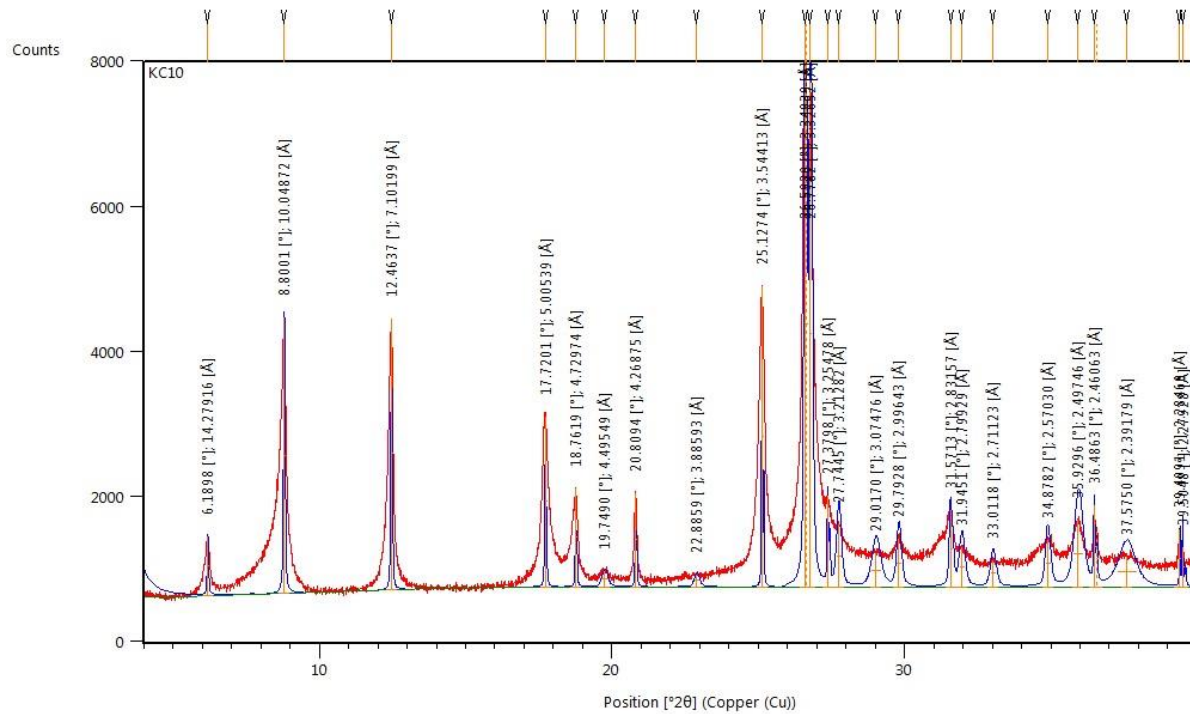
Appendix A.1 - 14 NHH1 bulk powder XRD analysis.



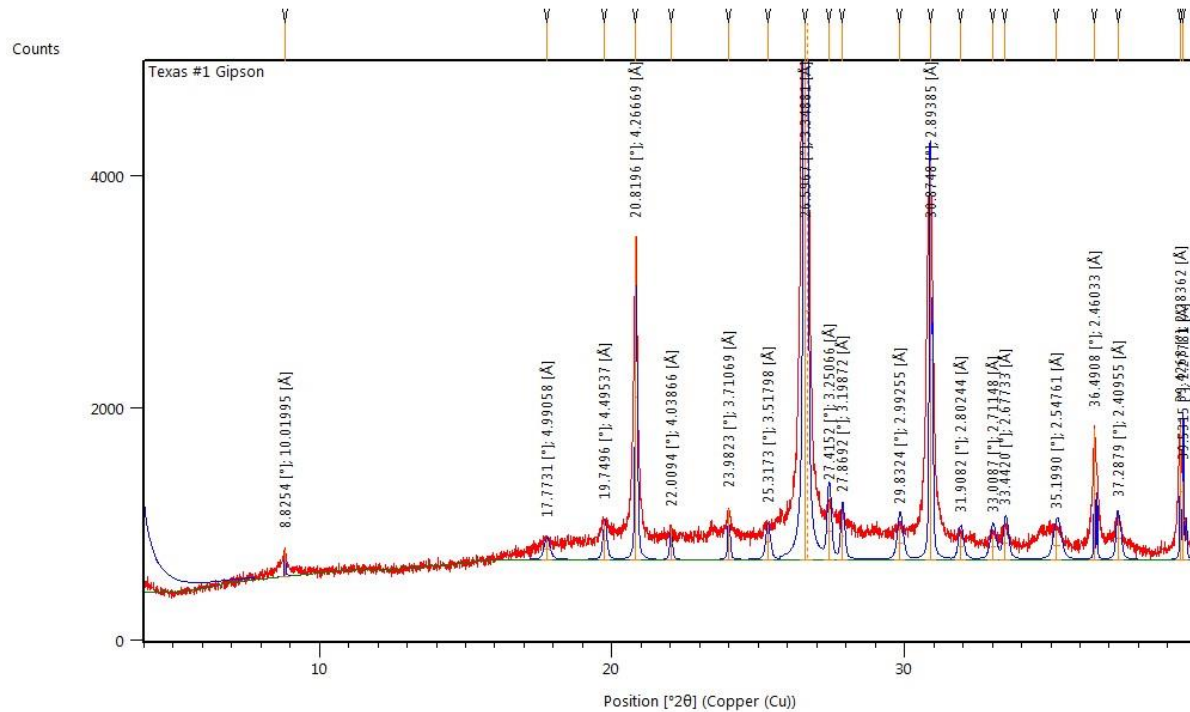
Appendix A.2 - 1 KC06 untreated clay slide XRD analysis.



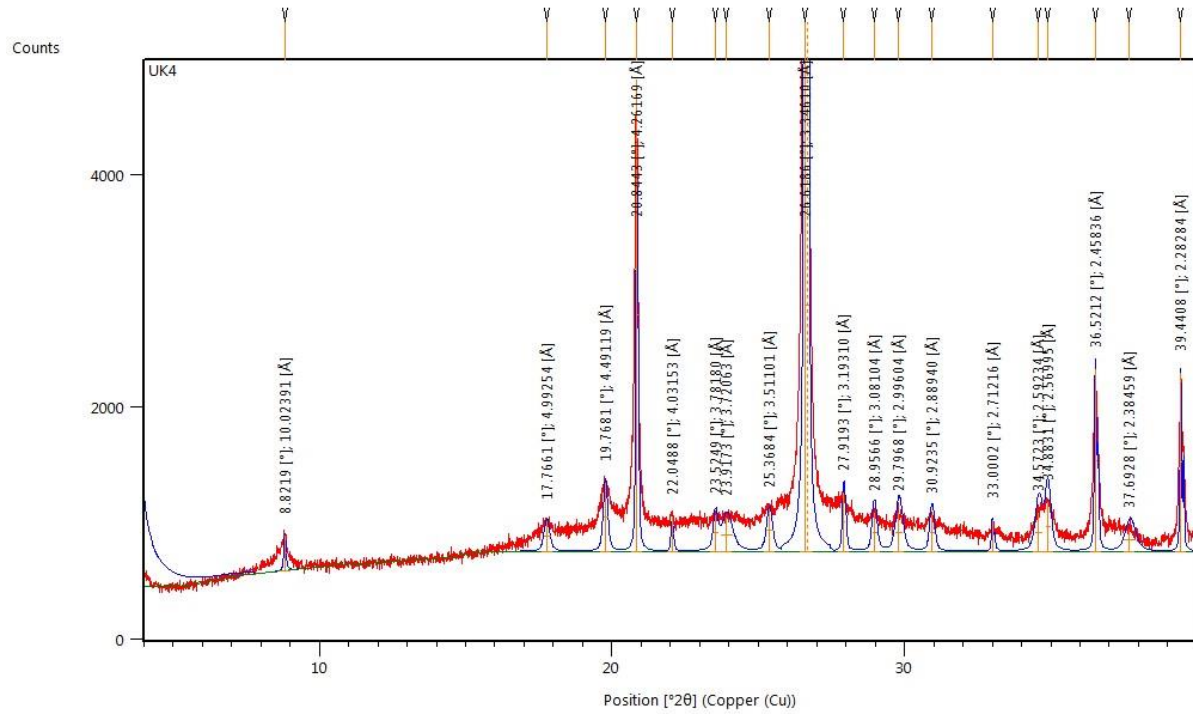
Appendix A.2 - 2 KC08 untreated clay slide XRD analysis.



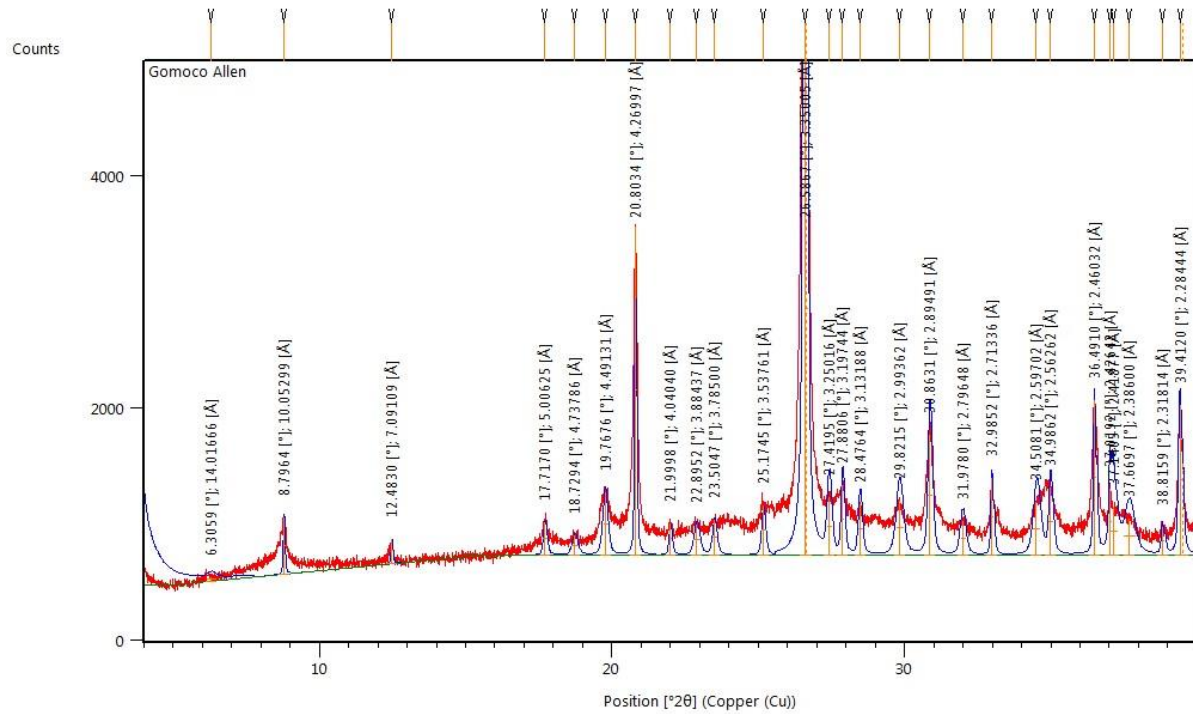
Appendix A.2 - 3 KC10 untreated clay slide XRD analysis.



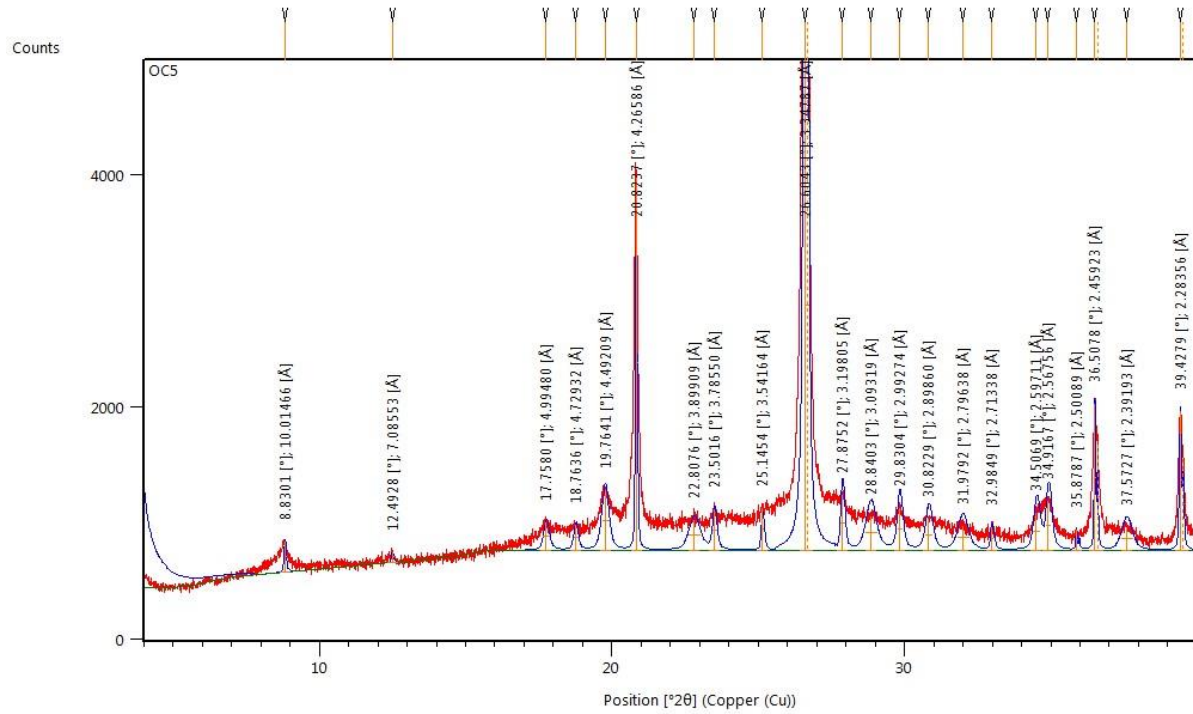
Appendix A.2 - 4 OC02 untreated clay slide XRD analysis.



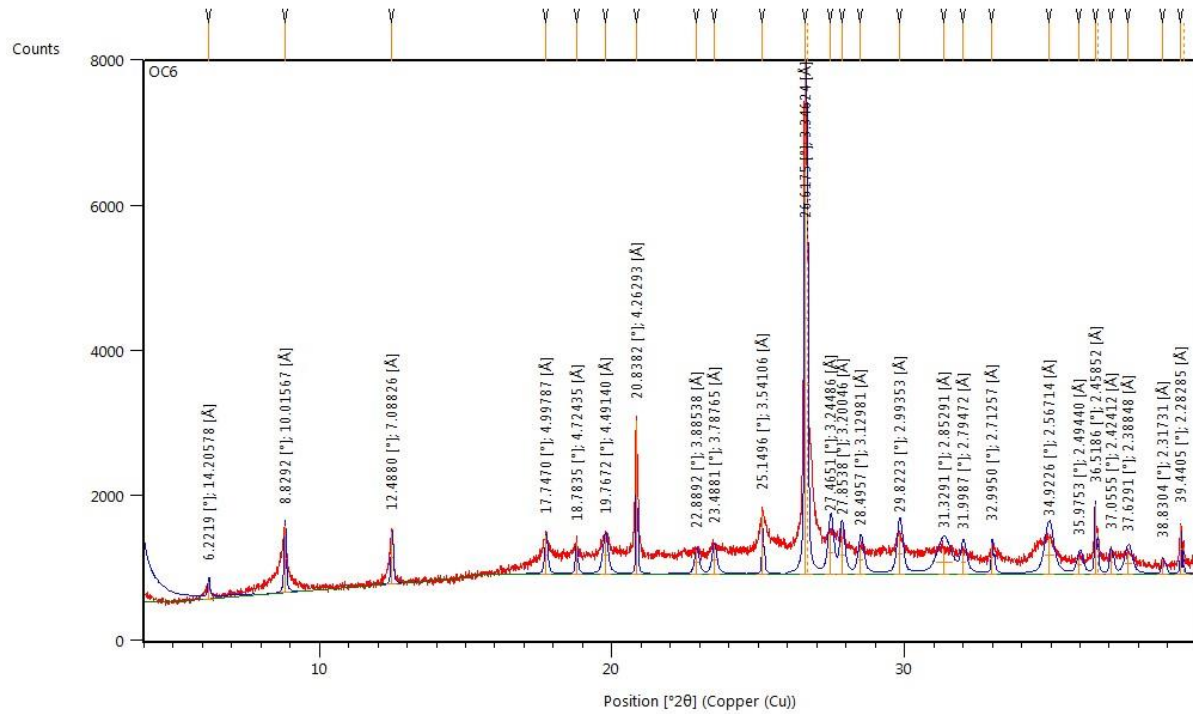
Appendix A.2 - 5 OC03 untreated clay slide XRD analysis.



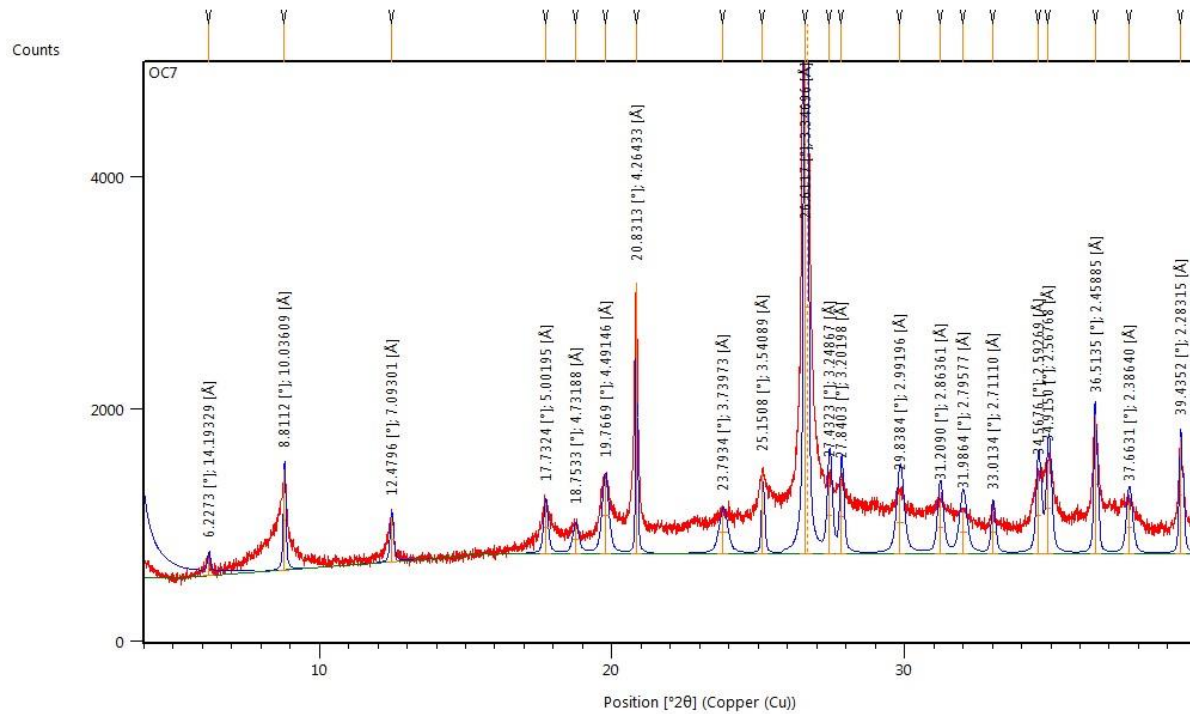
Appendix A.2 - 6 OC04 untreated clay slide XRD analysis.



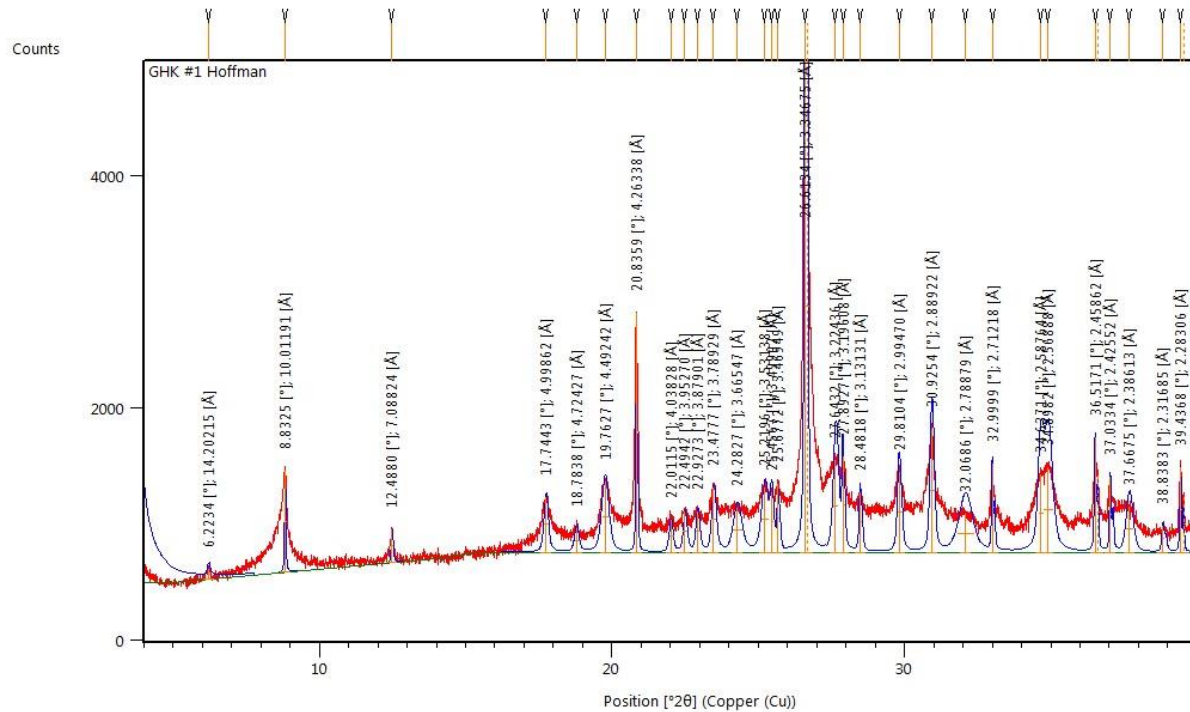
Appendix A.2 - 7 OC05 untreated clay slide XRD analysis.



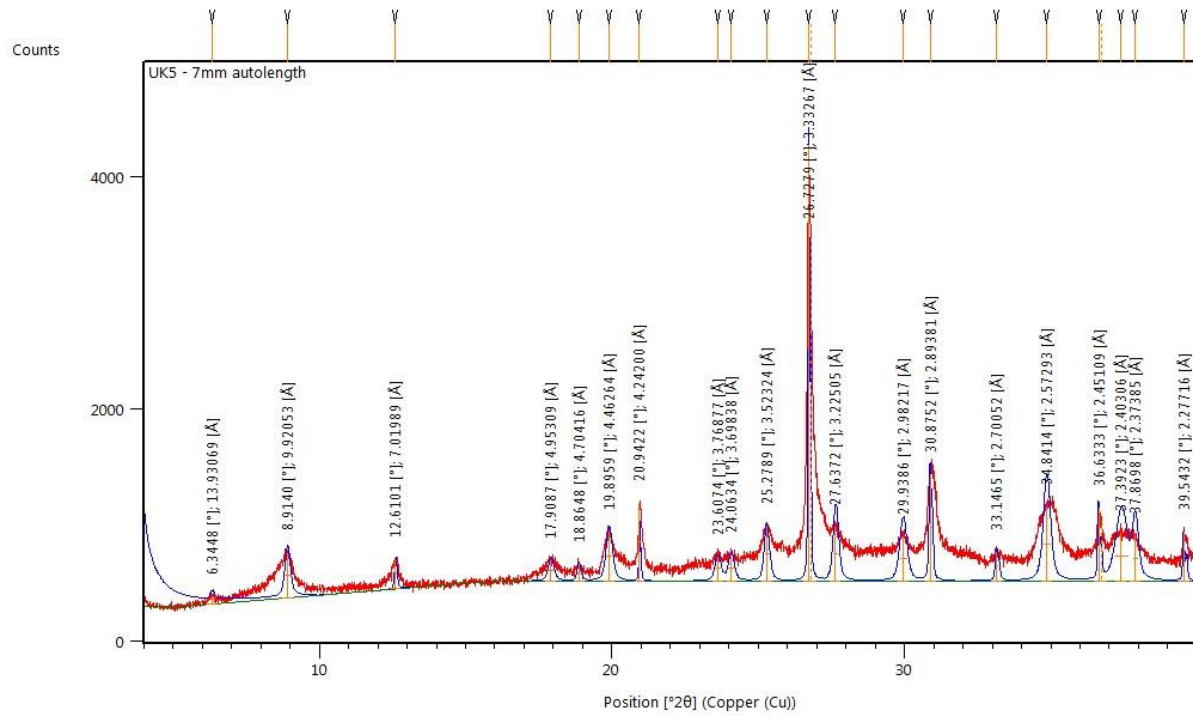
Appendix A.2 - 8 OC06 untreated clay slide XRD analysis.



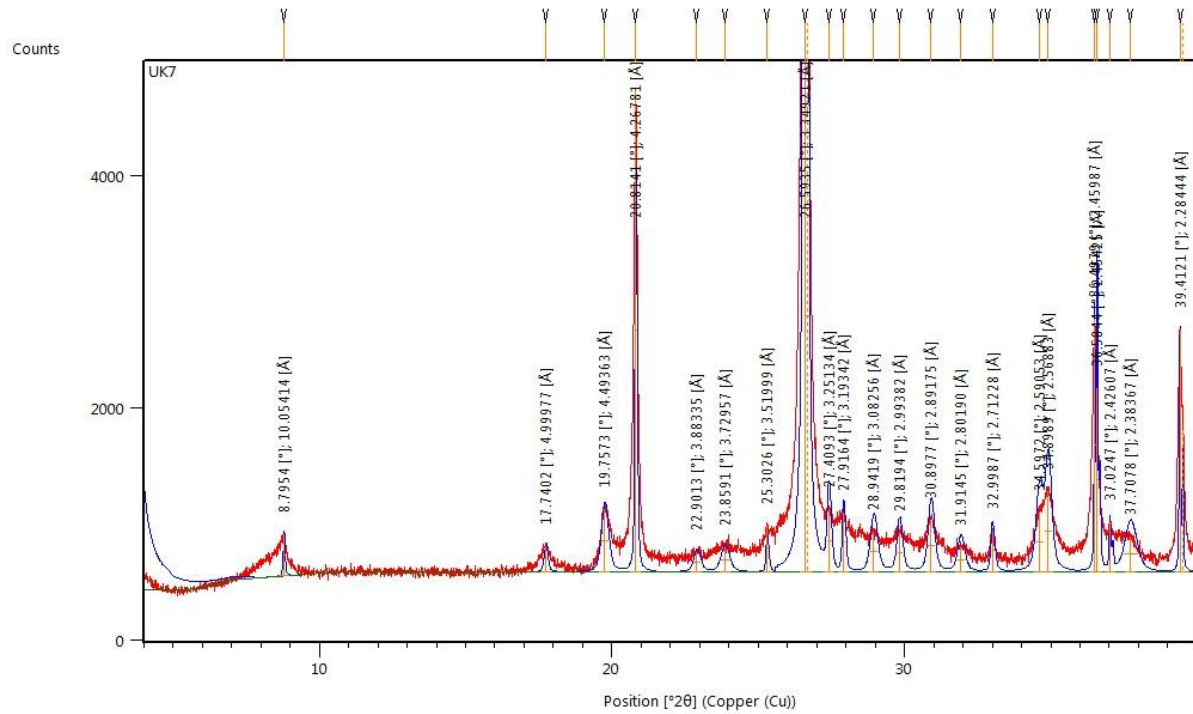
Appendix A.2 - 9 OC07 untreated clay slide XRD analysis.



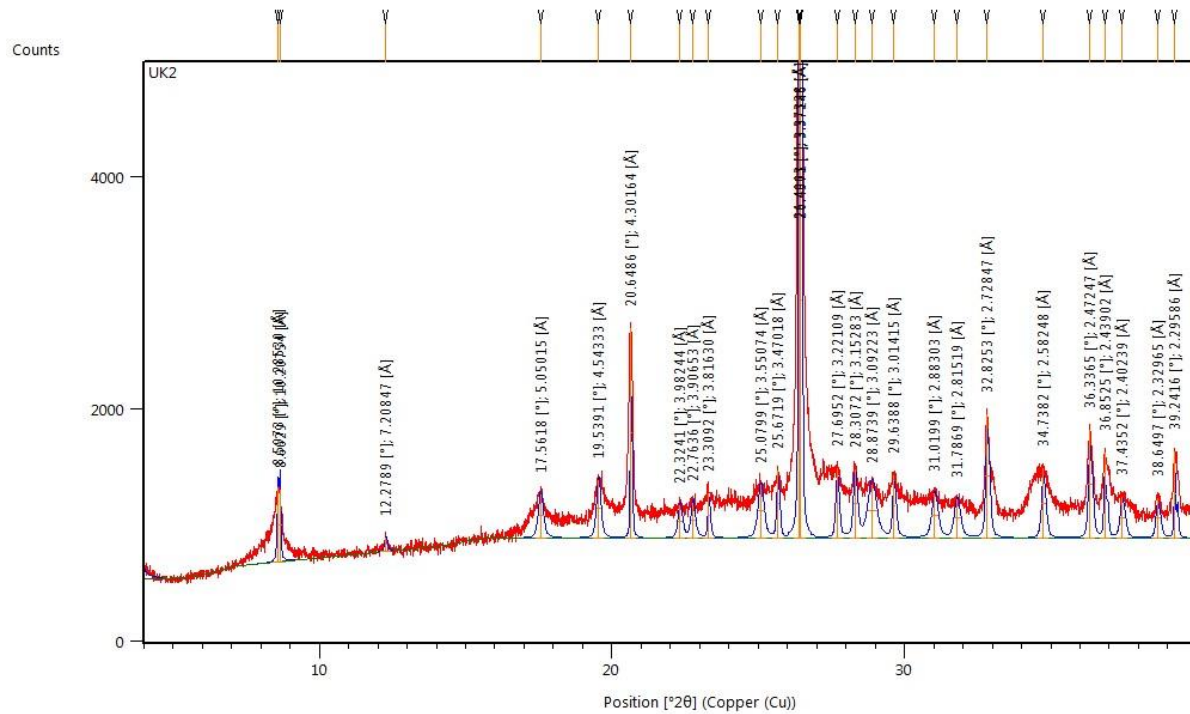
Appendix A.2 - 10 OC08 untreated clay slide XRD analysis.



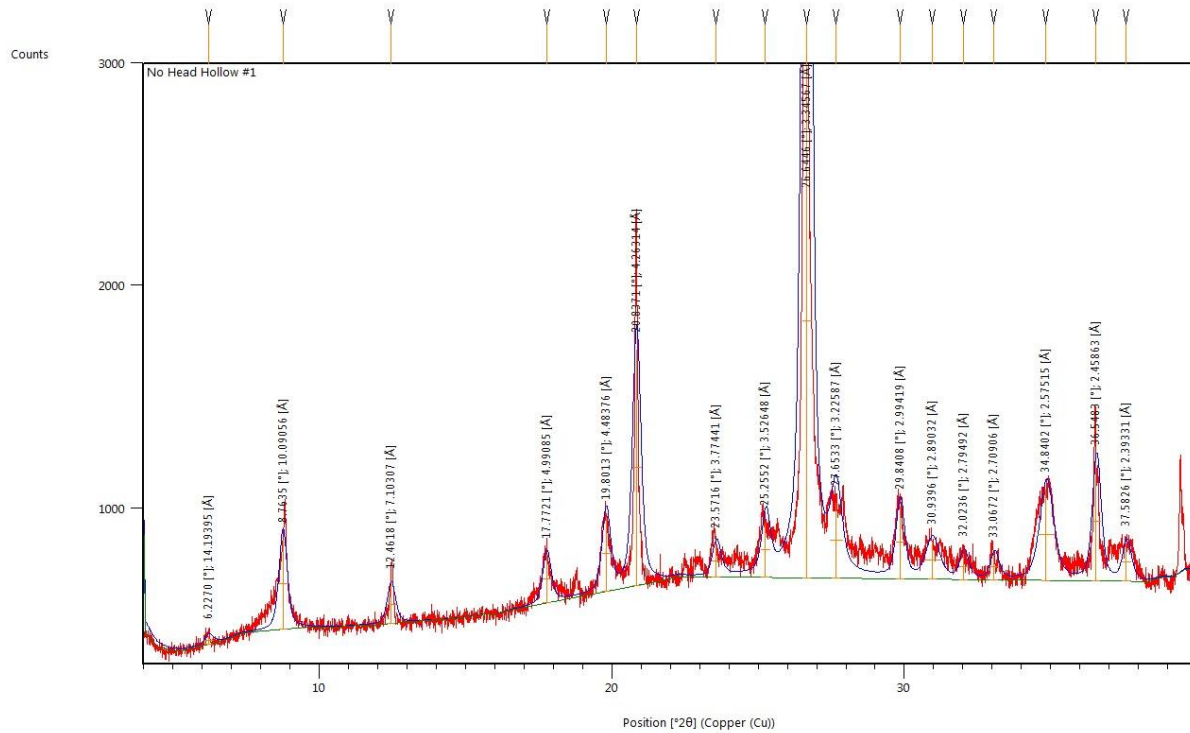
Appendix A.2 - 11 OC09 untreated clay slide XRD analysis.



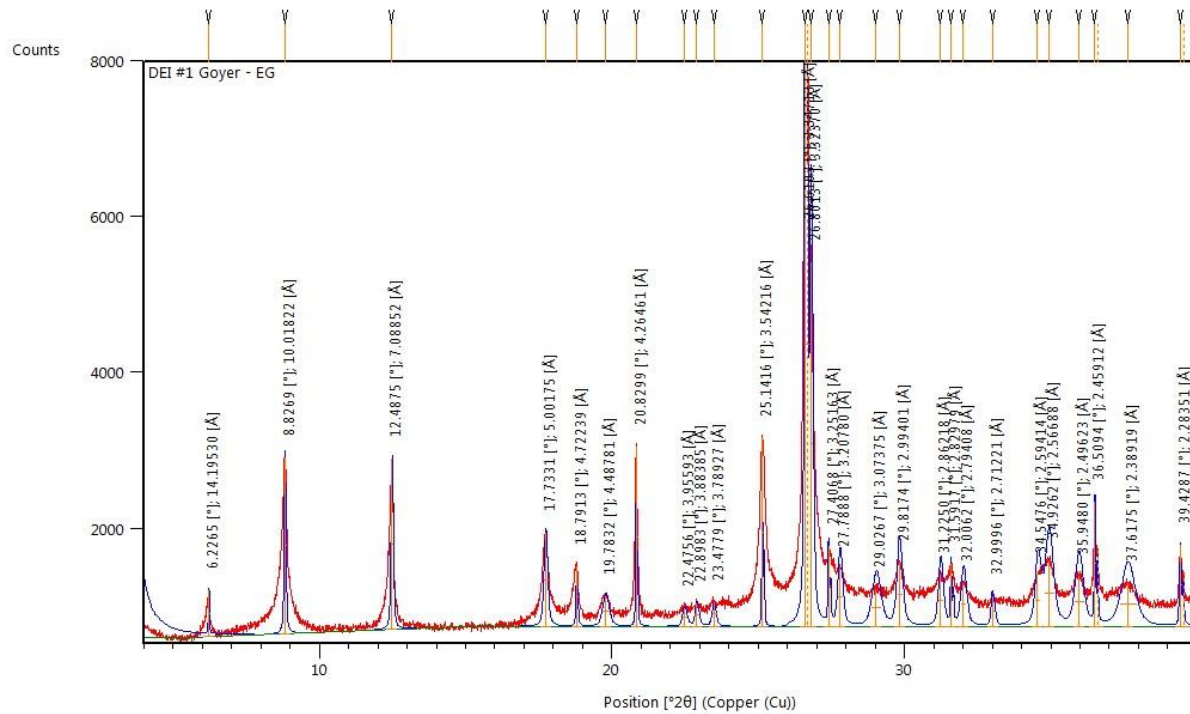
Appendix A.2 - 12 OC20 untreated clay slide XRD analysis.



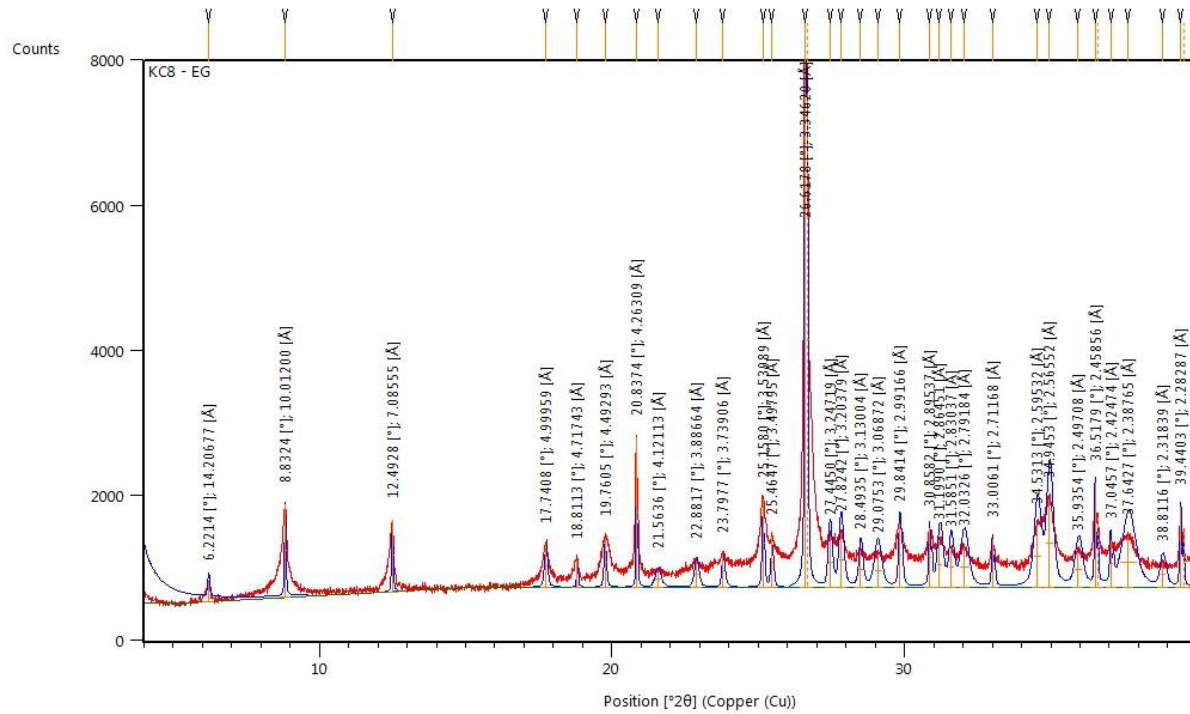
Appendix A.2 - 13 OC25 untreated clay slide XRD analysis.



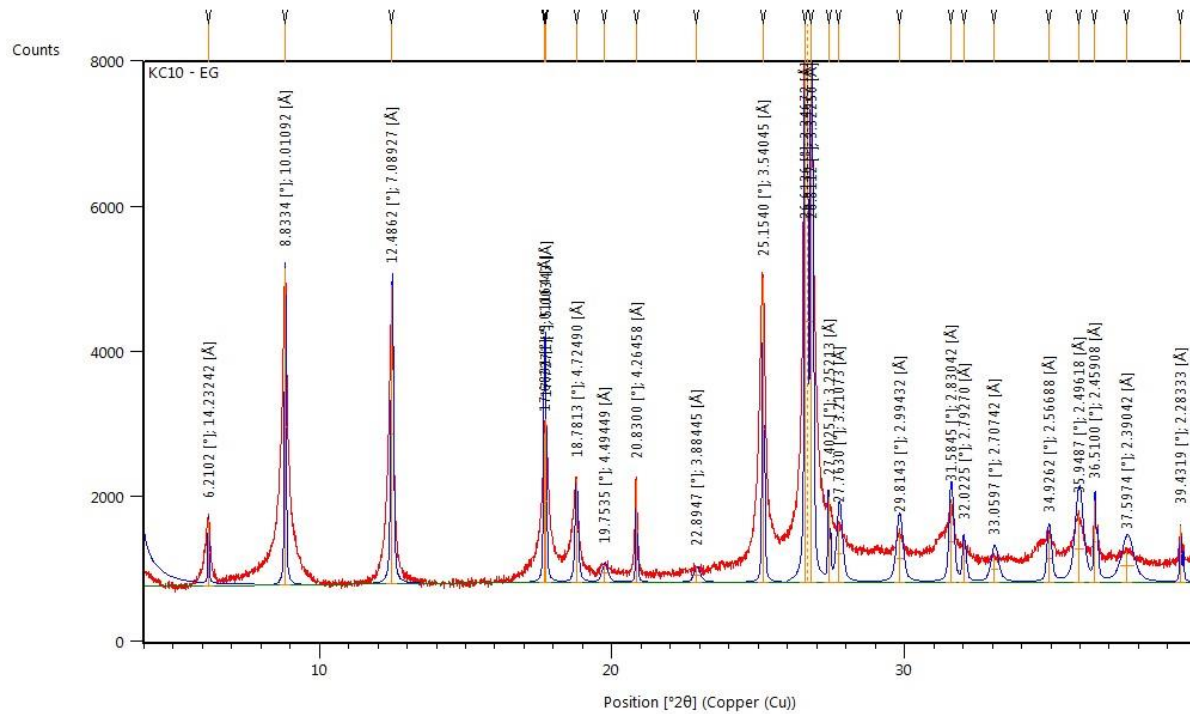
Appendix A.2 - 14 NHH1 untreated clay slide XRD analysis.



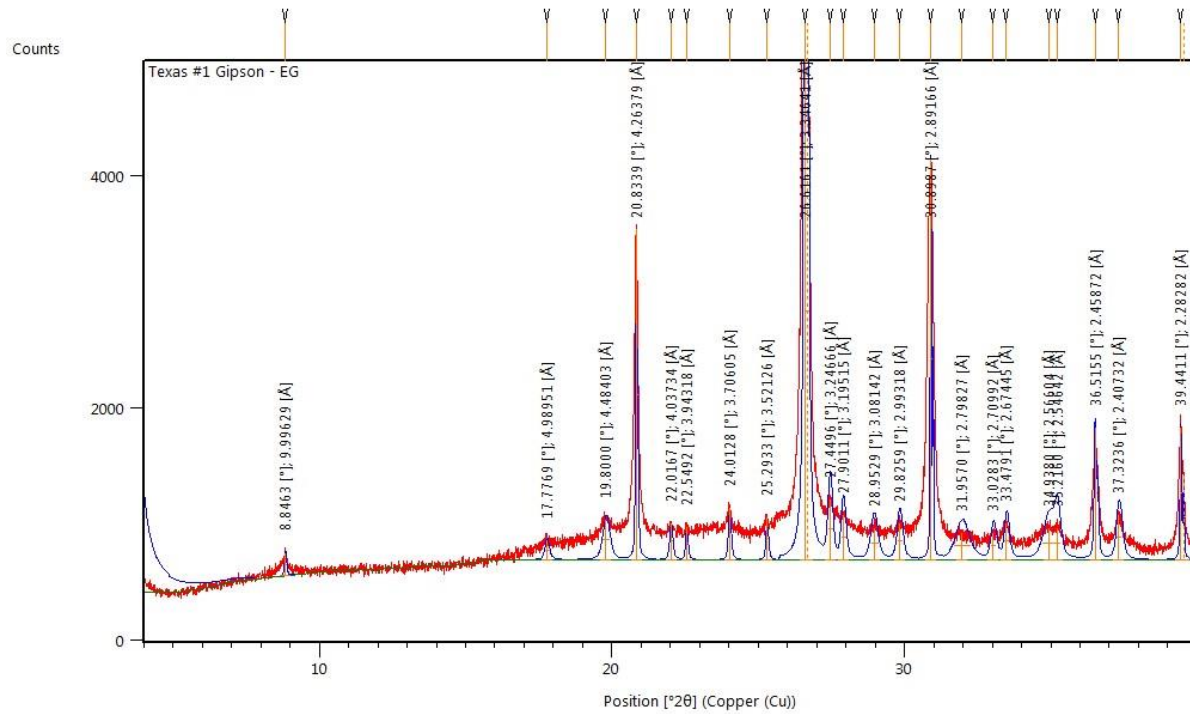
Appendix A.3 - 1 KC06 glycolated clay slide XRD analysis.



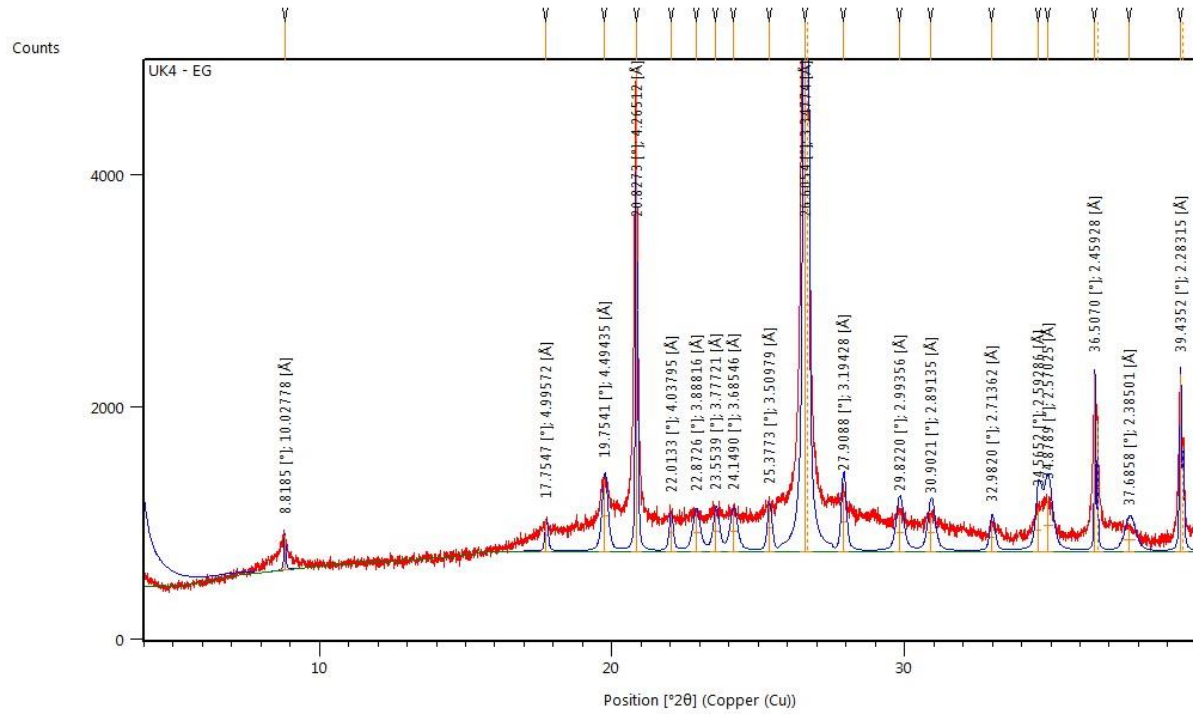
Appendix A.3 - 2 KC08 glycolated clay slide XRD analysis.



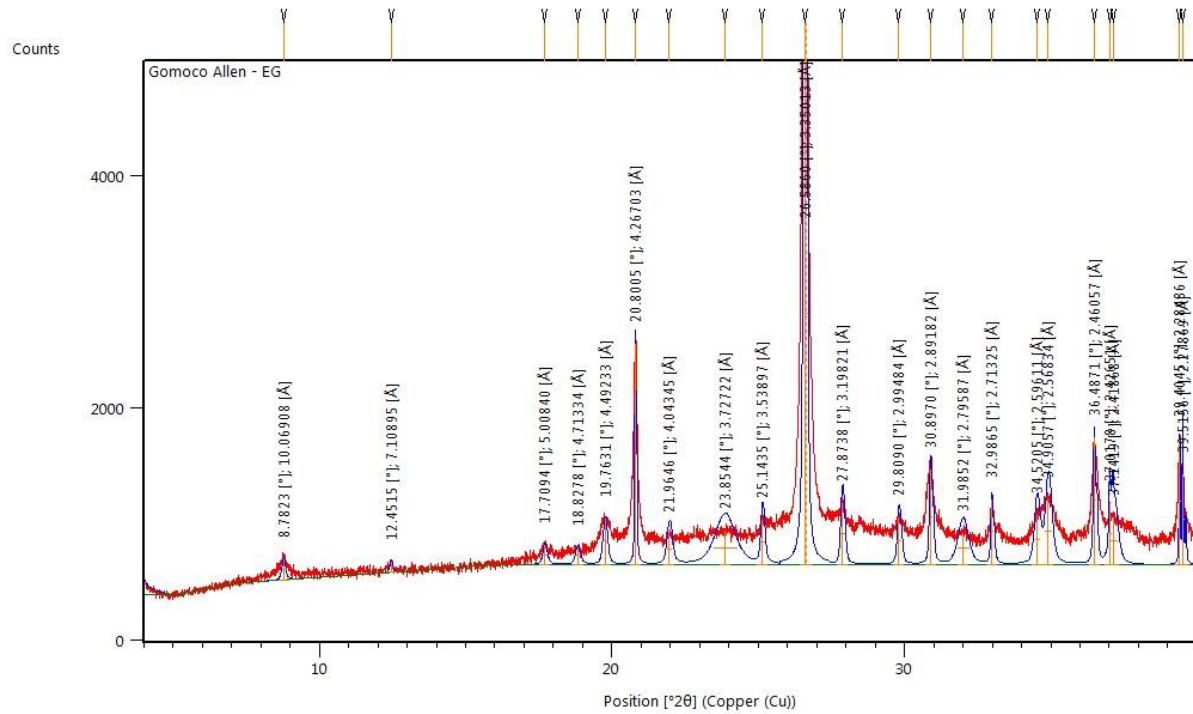
Appendix A.3 - 3 KC10 glycolated clay slide XRD analysis.



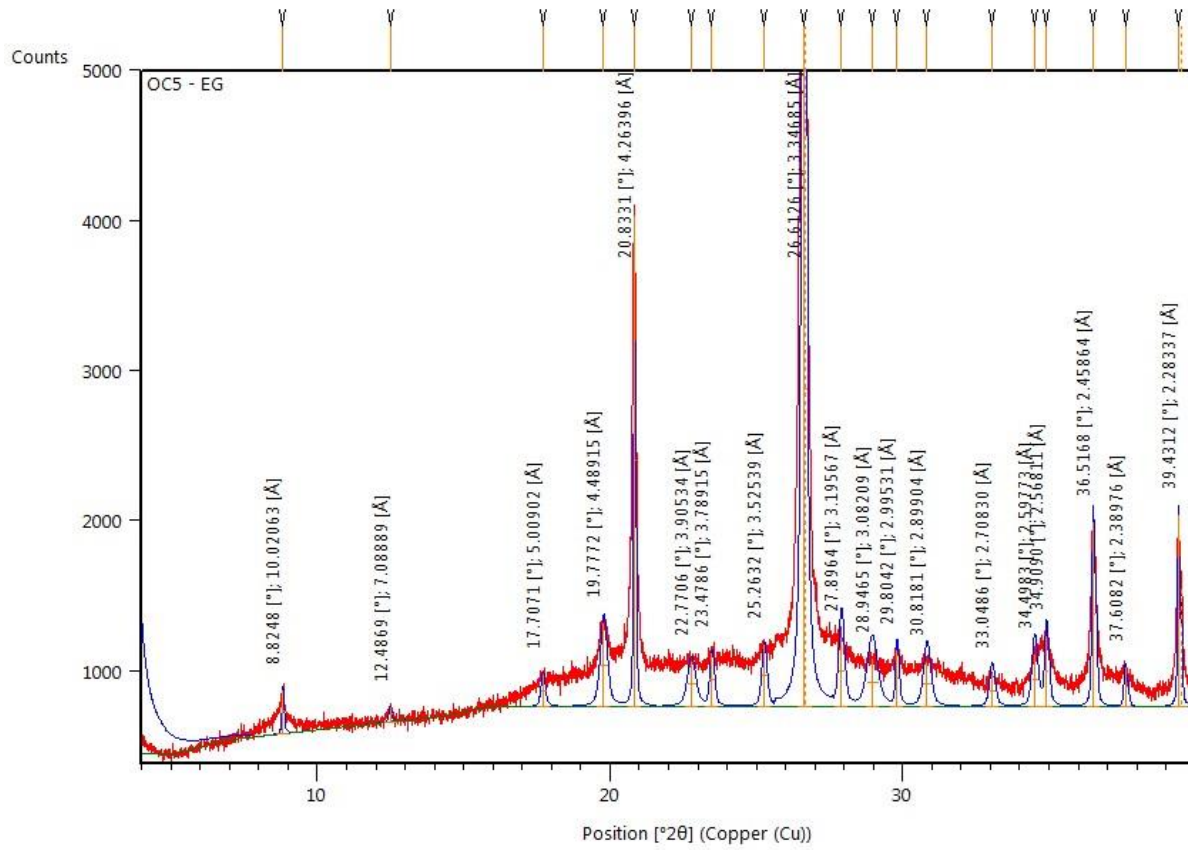
Appendix A.3 - 4 OC02 glycolated clay slide XRD analysis.



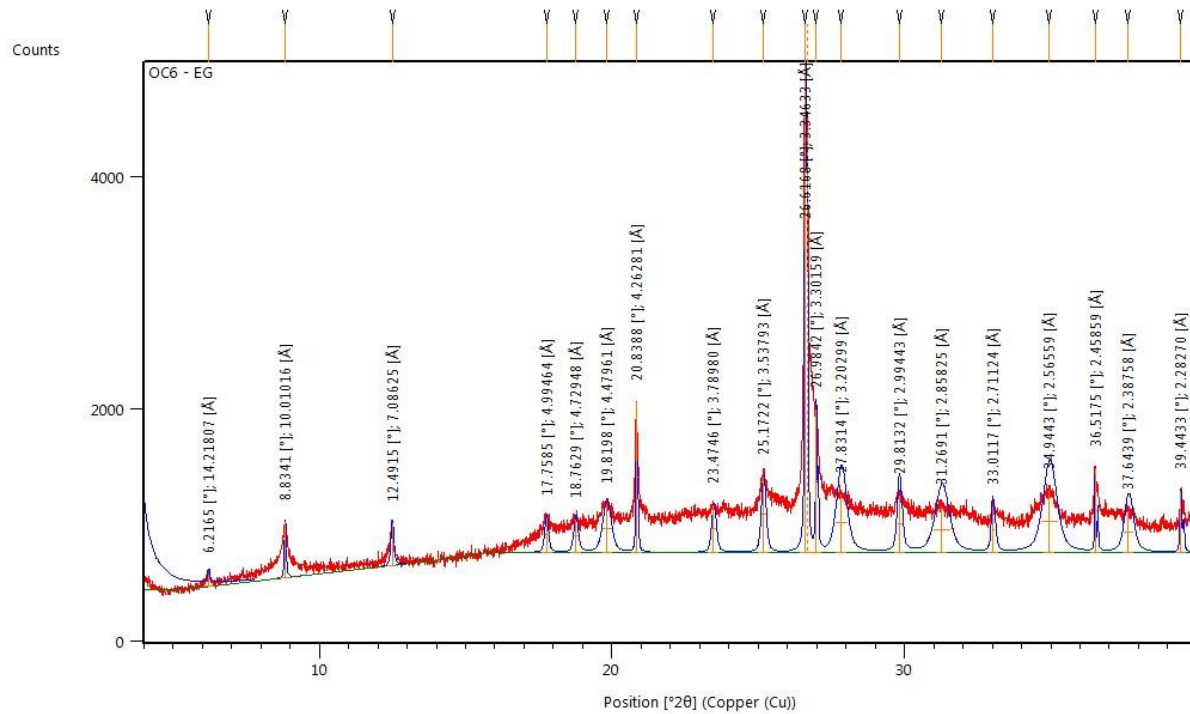
Appendix A.3 - 5 OC03 glycolated clay slide XRD analysis.



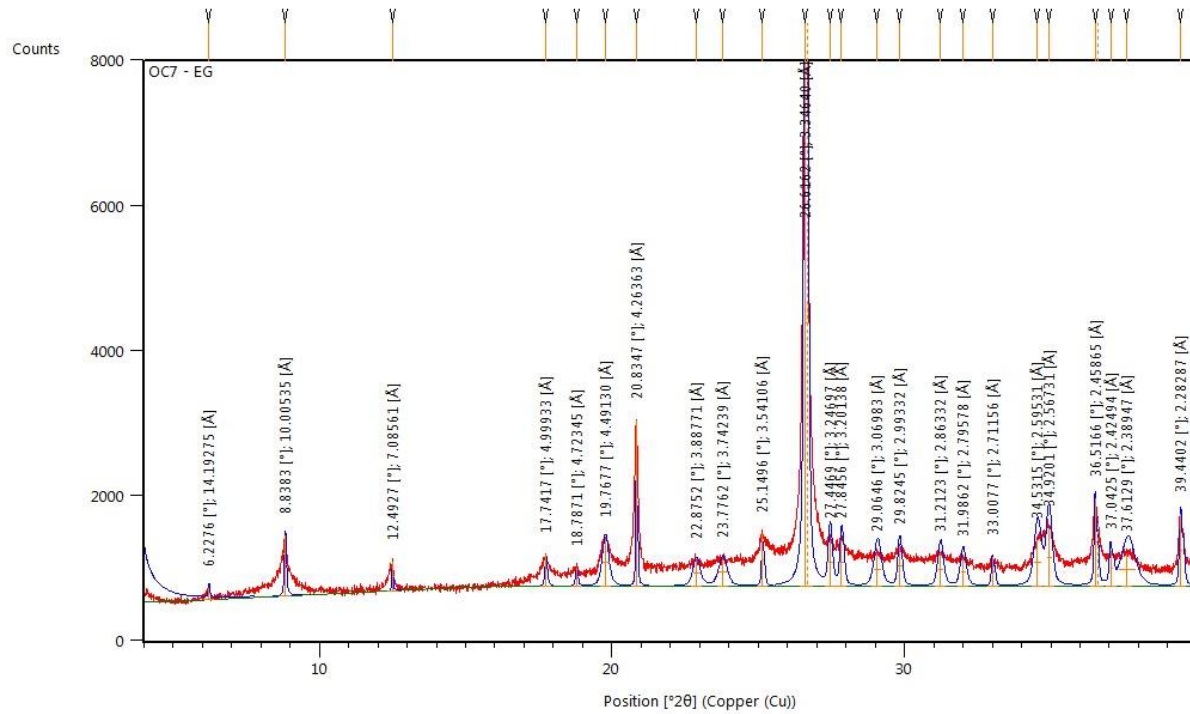
Appendix A.3 - 6 OC04 glycolated clay slide XRD analysis.



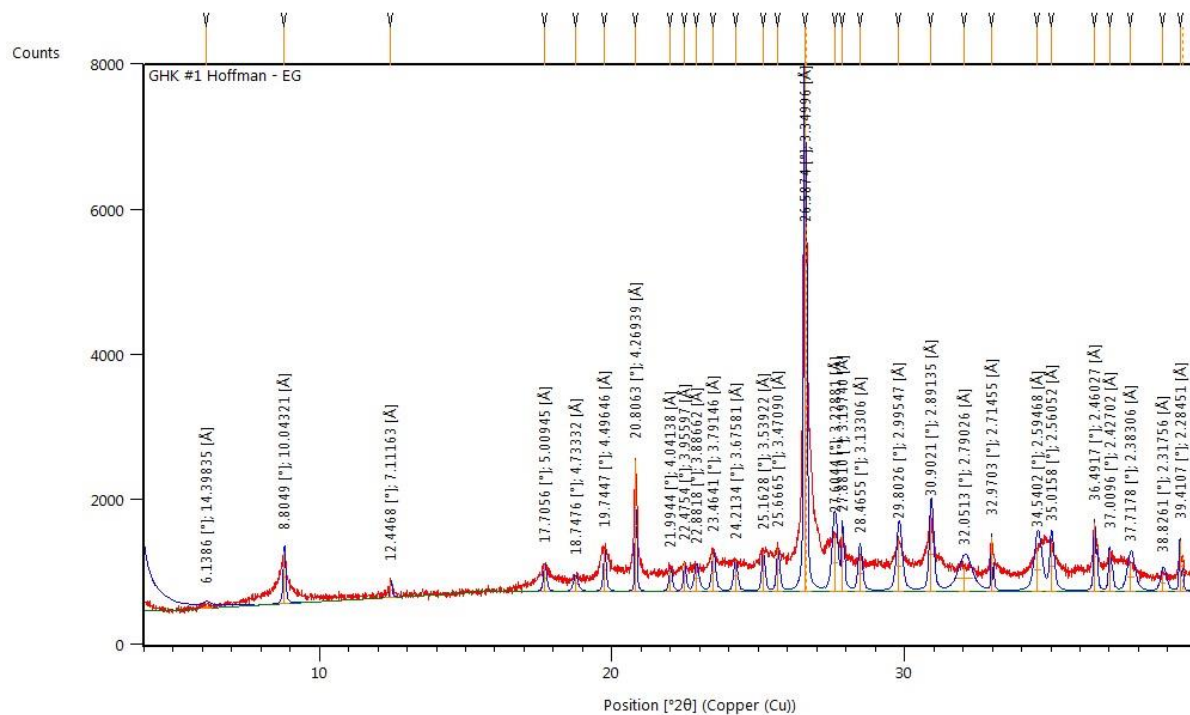
Appendix A.3 - 7 OC05 glycolated clay slide XRD analysis.



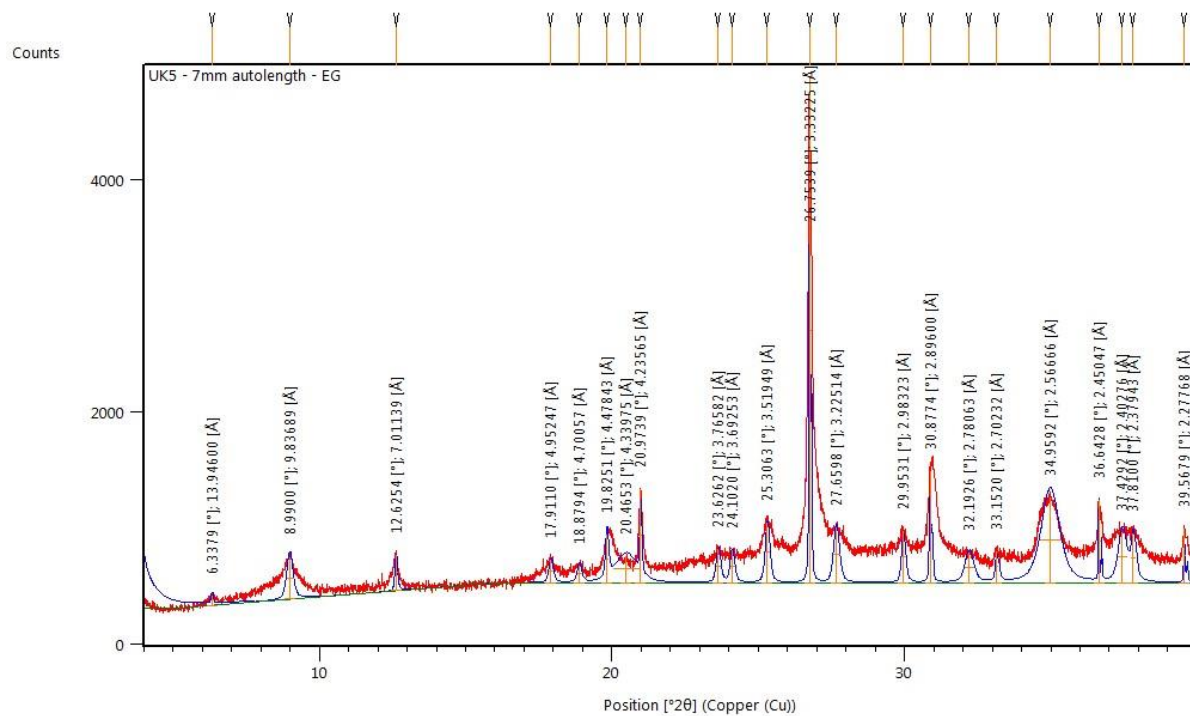
Appendix A.3 - 8 OC06 glycolated clay slide XRD analysis.



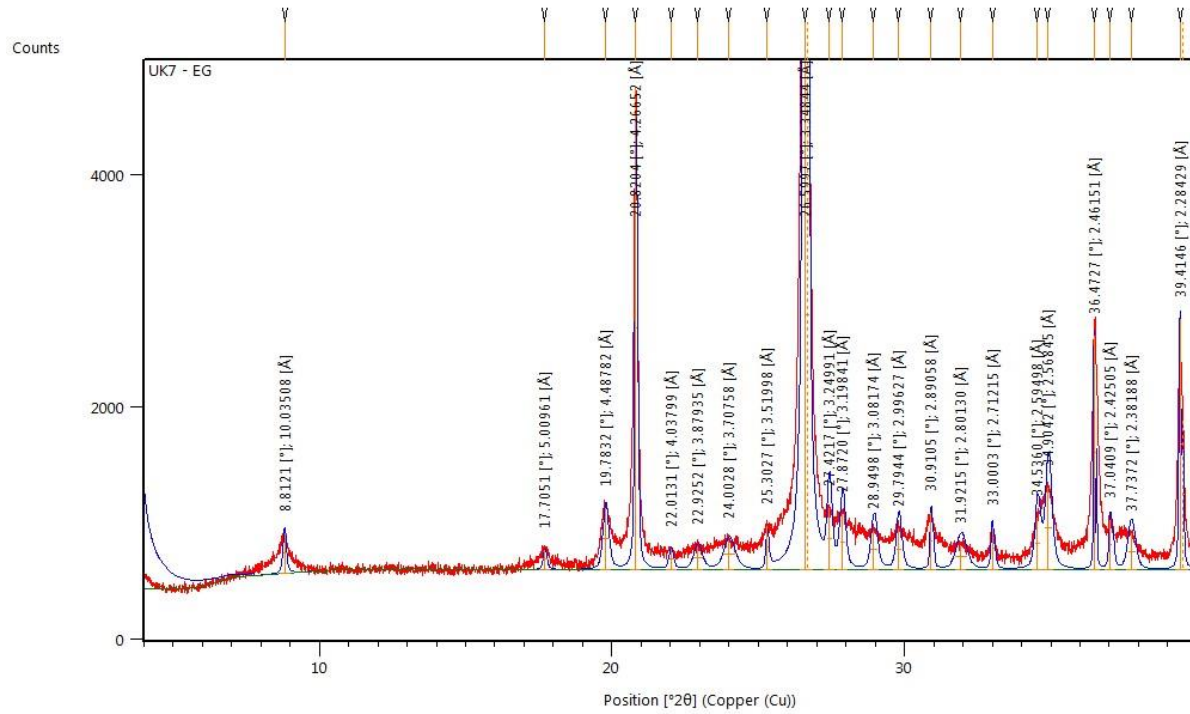
Appendix A.3 - 9 OC07 glycolated clay slide XRD analysis.



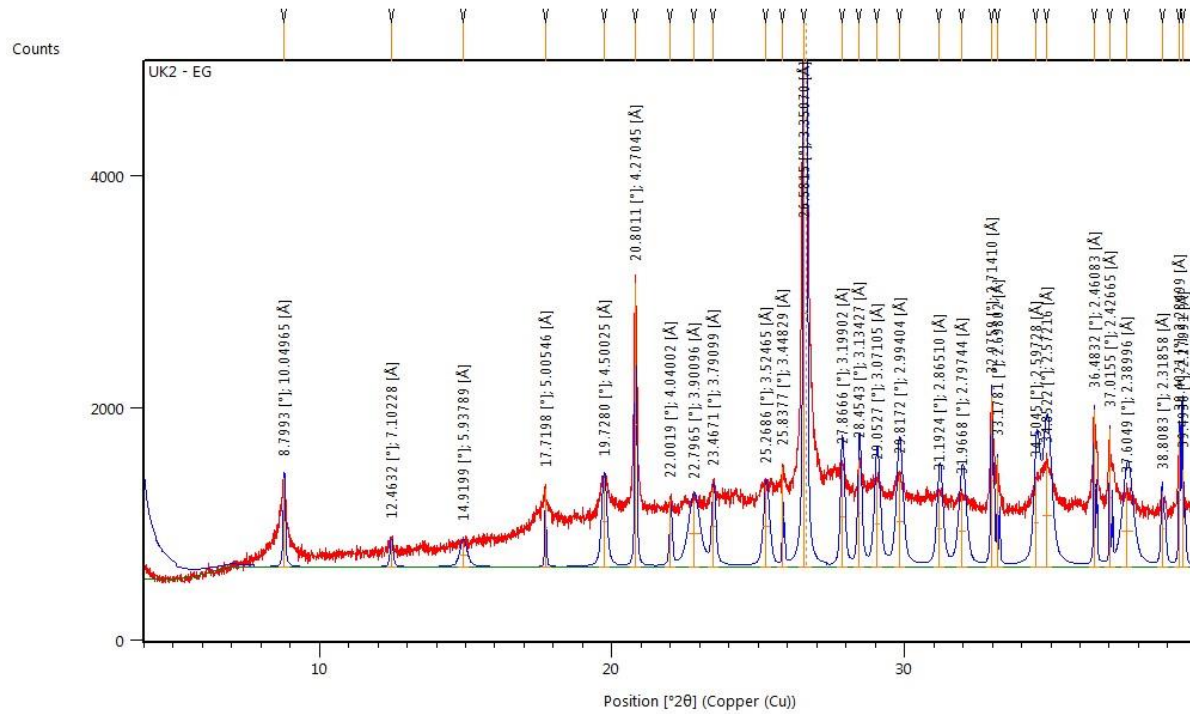
Appendix A.3 - 10 OC08 glycolated clay slide XRD analysis.



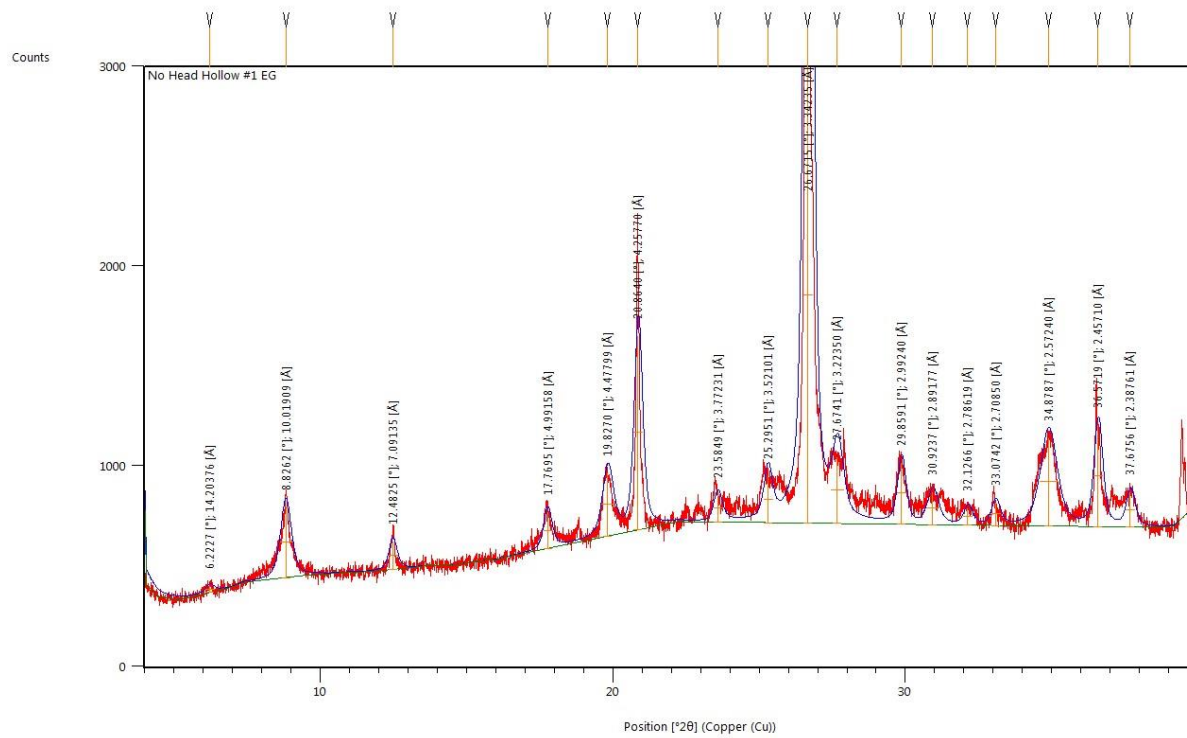
Appendix A.3 - 11 OC09 glycolated clay slide XRD analysis.



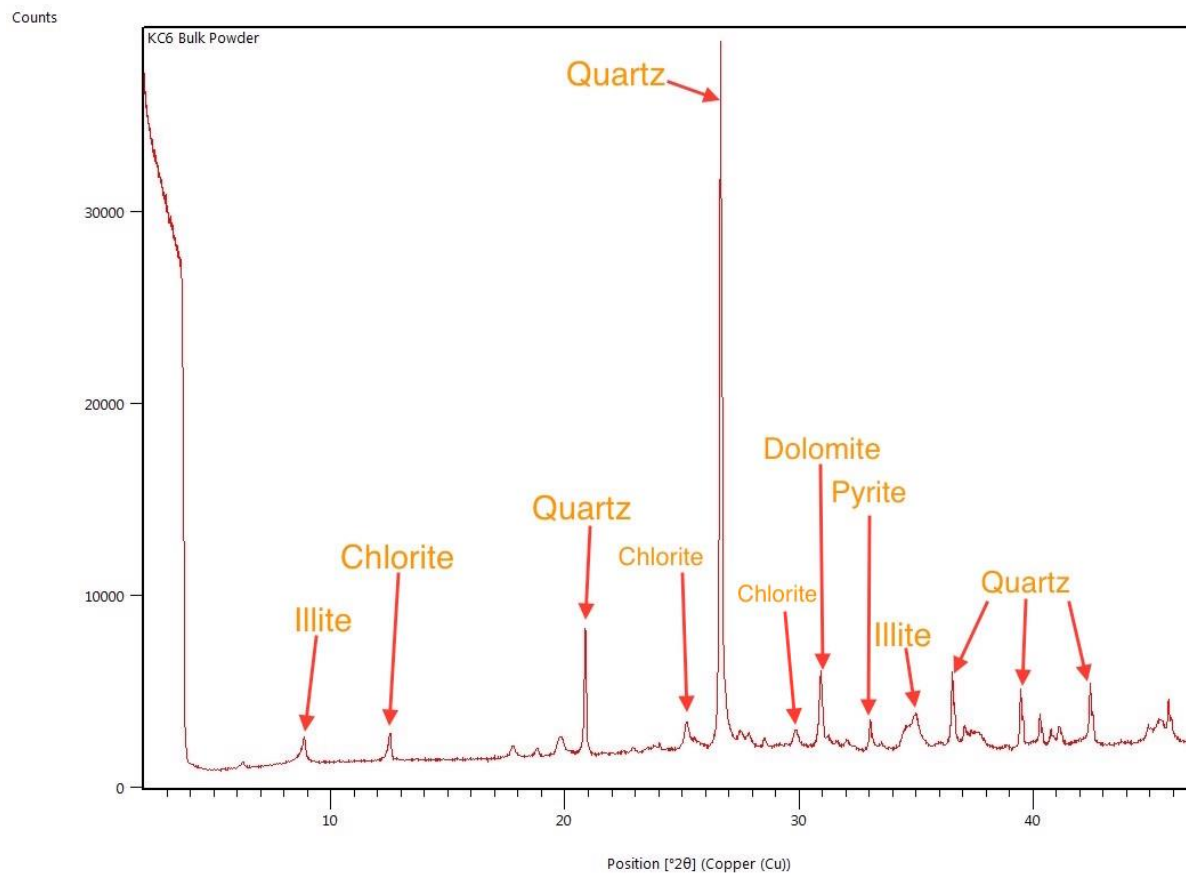
Appendix A.3 - 12 OC20 glycolated clay slide XRD analysis.



Appendix A.3 - 13 OC25 glycolated clay slide XRD analysis.



Appendix A.3 - 14 NHH1 glycolated clay slide XRD analysis.



Appendix A.4 - 1. Interpreted peaks for sample KC06 XRD bulk powder analysis.

Major	<u>Accepted values</u>	<u>Rowe et al (2012) measured values</u>	<u>Measured values this study (averaged)</u>
Mg (wt%)	0.67	0.8	-0.0075
Al	4.96	5.39	4.32
Si	32.6	33.7	26.4
P	0.07	0.05	0.045
S	3.34	2.18	2.37
K	2.07	2.31	2.42
Ca	0.13	0.23	0.118
Ti	0.23	0.27	0.27
Mn	0.015	0.012	0.02
Fe	2.93	2.53	2.63
<u>Trace</u>			
Ba (ppm)	2090	1884	1951
V	928	1114	975
Cr	110	98	113
Ni	130	153	146
Cu	83	147	130
Zn	823	844	842
Th	8.4	9	11
Rb	122	123	134
U	18.1	17	21
Sr	75.5	87	60
Y	35.4	34	32
Zr	80.3	95	115
Nb	9	9	12
Mo	79	83	77

Appendix A.5 - 1. Accepted and measured values for XRF clay standard RTC-W-220.